Acoustic Noise in Vector Controlled Induction Motor Drives

David Martínez Muñoz

LUND UNIVERSITY

Licentiate Thesis
Department of Industrial Electrical Engineering
and Automation

Department of
Industrial Electrical Engineering and Automation
Lund Institute of Technology
Lund University
P.O. Box 118
SE-221 00 LUND
SWEDEN

http://www.iea.lth.se

ISBN 91-88934-21-7
CODEN:LUTEDX/(TEIE-1028)/1-170/(2001)

Printed in Sweden by Media-Tryck
Lund University
Lund 2001

Abstract

This thesis deals with the analysis and prediction of the acoustic noise emitted from vector controlled induction motor drives. The effect of some structural changes in the stator, introduced with the aim of reducing the noise emissions, is also discussed.

Noise pollution in the environment and in the workplace can cause discomfort, a change in performance and even physical damage. Electric machines, and more in particular induction motors, are finding application in new environments where lower noise levels are demanded. It is, therefore, imperative that the designs should satisfy certain criteria in terms of noise generation and transmission. Vector control is one of the most commonly implemented strategies in variable speed drives, and hence the importance of understanding the characteristics of the noise generation when this technique is used.

A digital drive system has been developed for a 2.2 kW induction motor, and its dynamic capabilities demonstrated for a wide range of the frequency spectrum. This tool has been used for the experimental evaluation of the noise emissions when the flux and/or the torque are modulated with high frequency noise signals. The results showed that the noise emissions were higher when the flux was modulated compared to the torque, although the differences were considerably reduced when the machine was loaded. It was also observed that the noise emissions were decreased importantly at load. Sound pressure and sound intensity measurements have been conducted with the rotor stationary and rotating at low speed, showing that the most proper way to quantify the noise emissions from electric machinery is to measure the sound power through sound intensity measurements.

A method for the prediction of the noise emissions has been proposed, based in the interactive use of mechanical and electromagnetic finite element analyses, together with an acoustic boundary element method. The results show that

the accuracy of the noise prediction depends on the proper calculation of the modes of vibration in the structural analysis, as well as a suitable selection of the material damping. The effect of skewing also needs to be modelled in order to account for high order rotor harmonics. The influence of a 10% increase in the saturated part of the iron BH curve is translated into an increase of 3 dB or less in the sound power level, depending on the frequency.

The effect of the introduction of air gap layers around the outer part of the stator core in order to interfere with the natural transmission path for the vibrations has also been analyzed. When the gaps are filled with air the acoustic behaviour is not improved since the reduction of the stiffness in the outer core actually increased its sensitivity to the vibrations.

Acknowledgements

This work has been carried out at the Dept of Industrial Electrical Engineering and Automation (IEA), Lund Institute of Technology, in Lund, Sweden, and at the Acoustics and Vibration Unit (AVU), University College, The University of New South Wales, at the Australian Defence Force Academy (ADFA), in Canberra, Australia.

I would like to express my most sincere gratitude to Associate Professor Joseph C. S. Lai, who has contributed to my work providing guidance and support with the acoustic experiments and simulations, as well as very interesting discussions. I am thankful to my supervisor, prof. dr. ir. Duco W. J. Pulle, for his advise in control of electrical drives and in electric machines, as well as for proofreading the draft of this thesis.

I wish to thank all my colleagues and the staff at IEA and at the School of Aerospace and Mechanical Engineering, where the AVU was located, for being friendly, helpful, and providing a fantastic atmosphere. Many thanks go to Svante Andersson at IEA, for many enjoyable discussions, regardless of the topic. I am also grateful to Antti Papinniemi at the AVU, who was my laboratory companion for the experiments presented in Appendices A and B and, together with Dr Rei Yu, gave me advise with various issues related to the structural FEM package used. I wish to thank my room mate at IEA, Avo Reinap, for introducing me to the two dimensional electromagnetic software, and for being a very nice company.

I also wish to express my gratitude to Dr Alex Michaelides at the Vector-Fields support in Oxford for many discussions about the electromagnetic finite element modelling and software related issues. His efforts to solve several problems found with the software during the course of this project are well acknowledged.

The structural models of the test motor included in Chapter 4 were created

by Dr Chong Wang during his PhD studies at the AVU, and their availability is acknowledged. I am also grateful to Dr Robert Bjärnemo at the Dept of Machine Design, LTH, for giving me access to the structural software at the departmental computing facilities.

A number of people earn my gratitude for their support during the experimental work. Getachew Darge at IEA has been very helpful, specially repairing the DSP cards used in the experiments. At the AVU, I am grateful to Andrew Roberts and Glen Torr at the electronic workshop, who helped with the purchase and building of new equipment, as well as to fulfill the strict safety requirements in the laboratory before the experiments could be started. Dr Andrew Dombeck and the staff at the mechanical workshop also helped with practical issues. I wish to thank the Dept of Electrical Engineering at ADFA for sharing a lot of equipment that was needed for the experiments. The converter used to control the load motor was provided by Zener Electric Australia.

I am very thankful to Professor Lars Gertmar, who made a very detailed review of the draft of the thesis, Professor Mats Alaküla and Dr Kelvin Maliti, for proofreading the thesis and suggesting modifications and comments which have certainly contributed to the improvement of its quality.

Professor Gustaf Olsson is always a source of encouragement and support. This work has been partially financed by NUTEK, within the Acoustic Noise research program, and also with internal funds at IEA, including my year in Australia. This support is gratefully acknowledged. The AVU contributed financially not only sharing its personnel, facilities and advanced acoustic equipment but also purchasing laboratory and computing material, which is very much acknowledged.

Last, but certainly not least, I would like to thank my parents Manuel and Josefa, and my two brothers Manuel and José Andrés for all their love, trust and support over the years.

Lund, November 18, 2001,

David Martínez Muñoz

Contents

Chapter 1

Introduction

1.1 Background

Major contributions on acoustic noise in adjustable-speed a.c. electric motor drives have been done during the last 15 years in connection with the advent of more and more cost effective and powerful frequency converters. The new installations of adjustable-speed drives in industry and commercial buildings are today to a majority embodied as a.c. induction motor drives, i.e. as low-maintenance, brush-less drives, pushing traditional d.c. brush-commutator motor drives aside. The level of motor noise radiated increased considerably, as a consequence, due to the current harmonics introduced by the switching technology in the converter. This thesis focuses on the embodiment of the frequency converter what regards modern voltage and airgap flux modulation techniques. The literature referenced here is therefore limited to recent publications on adjustable-speed a.c. electric motor drives although the author is well aware that contributions on constant-speed a.c. electric motor drives were made as early as during the First World War and, with the spreading of digital computers, up to the 1970's.

Noise sources

In general, three different sources of noise can be distinguished in electric machines: mechanical, aerodynamic and electromagnetic. The mechanical component is mainly influenced by the way the stator sheets are mounted into the core of the motor, the coupling to the load, rotor unbalance, as well as the vibration of the bearings and the amount of damping material present in the structure.

The aerodynamic component is only dependent on the fan used in air cooled machines. The electromagnetic component is due to the action of magnetic forces in the airgap. These forces are influenced by the harmonics present in the voltage feeding the machine, slot combinations, saturation, magnetostriction and eccentricity among others.

After all, noise is produced due to the mechanical vibrations that take place in the machine. Hence, it is important to evaluate how the different components of the structure influence the noise emissions. One factor to take into consideration is that the machine usually presents some changes compared to the original design, due to the tolerances introduced during the manufacturing process, which become more important in mass production. Starting from the same prototype design, it is not unusual to find machines with a rather different acoustical behaviour, as analyzed in Zhu et al. (1997). The main variations are found in the eccentricity of the rotor relative to the stator, which is one important source of noise. An acoustical simulation method is presented in Ramesohl et al. (1999), where the effects of a great deal of different manufacturing tolerances are studied in mass produced electric machines. A combination of electromagnetic and mechanical FEM is used to calculate the force densities which are applied to an acoustic boundary element model (BEM).

Eccentricity is one important factor that has to be taken into consideration when studying the acoustic response of an electric machine. There are namely two types of eccentricity: static eccentricity, or incorrect positioning of the rotor with respect to the stator bore, and dynamic eccentricity, when the machine has a bent shaft due to mechanical unbalance. In other words, in the case of static eccentricity the closest part between the rotor and the stator remains unchanged along the shaft and is fixed always to the same stator point, independently of the rotation of the rotor. In the case of dynamic eccentricity, this closest part varies along the shaft for a given rotor position, and rotates with the rotor all around the inner stator surface. Dynamic eccentricity is usually checked in the manufacturing stage and compensated by means of dynamic balancing. However, static eccentricity is hardly checked during the production process and its contribution to the generation of audible noise is studied in Delaere et al. (1998).

One of the optimization parameters in electric machine design is the size of the motor, and thus the amount of iron needed to achieve a certain performance. Reducing the size of the core decreases the stiffness of the stator structure, which in turn becomes more sensitive to forces acting on it. Therefore,

there is a compromise between cost and noise. An optimization process was developed by Hadj Amor et al. (1995) where, for randomly selected dimensions of the structure, the noise is estimated and in this way the dimensions of the motor producing the least noise can be found. The results obtained suggested the existence of only one minimum, which not surprisingly corresponded to a very heavy and expensive motor.

The stiffness of the stator is also directly influenced by the amount of damping material present on it, as explained in Verma and Balan (1998). Damping materials in the stator are the windings, laminations and insulation. Experiments carried out with a stator shell, both with no laminations and a laminated stator, confirmed that the noise level was around 20 dB lower in the case of the laminated stator, due to its higher amount of damping. Besides, the peaks along the frequency scale in the noise spectrum were more flattened. However, the stiffness of the laminated stator is lower than the stator shell with no laminations, which means that there will be several more resonances falling in the audible frequency range. This behaviour is further affected by the fact that the damping at these frequencies is reduced, as it is proportional to the resonant frequency and the damping ratio, i.e. the benefits of damping are less accentuated at lower frequencies, but still the overall acoustic emissions are lower when damping is present.

The stiffness of the machine is also increased when coupling the motor to the ground (foot mounting) and the load (shaft mounting). The effect on the acoustical emissions of this coupling was analyzed in Zhu et al. (1999) and showed that, although additional natural frequencies are added to the system, the coupling restricts the stator vibration, as its stiffness is increased. The result is that the acoustic noise produced by the machine is reduced. Further, it was shown that even if two similar motors present quite a different acoustic behaviour at no load, when loaded not only the acoustic noise is reduced, but also the acoustic behaviour of both machines becomes much more similar.

In fact, the noise produced by one induction machine can change considerably depending on the ratio between the stator and rotor slots. In general, odd rotor slot numbers should be avoided. A more complete study was presented in Kobayashi et al. (1997), where transient magnetic field FEM and harmonic analyses using Fourier series expansion are used together to compute the forces for a given number of stator and rotor slots. It was found that the level of acoustic noise is dependent on the first space harmonic order, which was not always predicted by analytical calculations based on the slot ratio of the machine.

While the sources responsible for the acoustic noise in electric machines are widely accepted, there is a lack of consensus about the physical mechanisms of noise production in the machine. The most accepted theory is that the stator vibrations are produced by the radial components of the electromagnetic airgap forces, whereas tangential forces are usually neglected. However, tangential forces can play an important role in large machines, as discussed in Garvey and Le Flem (1999). The influence of magnetostriction is not yet clear. It is a phenomena that consists on the change in the dimensions of the iron when a magnetic flux passes through it. The iron tends to contract along the direction of the flux and tends to expand in the other two directions, and this process increases the level of vibration in the machine. In Belmans and Hameyer (1998), it is considered that although the effect of magnetostriction in theory can contribute to the audible noise, in practice its contribution is negligible. However, a method was presented by Garvey and Glew (1999) where the effects of magnetostriction in the stator core can be computed and its importance is showed. In Låftman (1997), after a series of experiments, it is stated that the magnetostrictive forces are about the same magnitude as the Maxwell forces in medium sized induction machines, in the range of a few tens of kilowatts, and therefore they would have a major importance in the production of noise in electrical machines.

Finally, the effect of the geometrical and constructional irregularities were presented in Chang and Yacamini (1996). It was found that these irregularities introduce asymmetrical behaviour, which results in an enriched frequency response spectrum. The asymmetry frequencies are caused mainly by the stator winding and frame irregularities which means that the design details of the winding and the frame will play a very important role in the mechanical behaviour of electrical machines and should not be treated simply as an additional mass. Hence, motors should be designed and constructed as symmetrical as possible, in particular the winding overhang.

Electromagnetic force computation

In order to predict the noise behaviour of the machine, it is important to evaluate the airgap flux distribution, which is directly linked to the harmonic pattern of the electromagnetic forces acting on the stator. Many theories have been developed for their analytical computation and approximations need to be introduced in order to model the numerous details in the machine affecting the

airgap forces such as saturation, slot shape, etc. Some of the theories proposed provide a quick and relatively accurate prediction of the expected airgap force frequencies and repetencies, although they are still imprecise in the calculation of their magnitudes. A modified one-dimension theory is used by Gerling (1994) taking into account the changes in the reluctance along the airgap due to the stator slots, while no rotor slots are considered. The main idea is to use the geometrical airgap in the region of a stator tooth, and enlarge it only in the region along a slot opening by a factor regarding the average length of the field lines penetrating through the slot. This procedure shows more accurate results than considering a general enlargement of the geometrical airgap through the whole surface to account for the effects of the stator slot openings. A new correction factor associated with the depth of the slot openings improved considerably the accuracy when predicting the amplitudes of the harmonics.

Another approach accounting for the effects of stator and rotor slotting, eccentricity, iron saturation and the interactions between the various stator and rotor current components was presented by Vandevelde and Melkebeek (1994), using the rotating field theory and the permeance wave technique. The airgap flux density components are then obtained by multiplying the permeance waves, in which the effects of slotting, eccentricity and saturation are modelled, by the magnetomotive force. A more accurate model based on a magnetic equivalent circuit method (MEC) was also elaborated for the calculation of the flux components and the resulting radial magnetic forces (Vandevelde and Melkebeek, 1997).

The effects of both stator and rotor slot openings under load and no load conditions were studied analytically by Cho and Kim (1998), taking into consideration the effects of skewing and the rotation of the rotor, as well as eccentricity. At no load the model was accurate in predicting the frequencies of the harmonics but not the amplitudes. Besides, under load conditions there were slight discrepancies in the magnitude of the main flux.

Although the analytical approaches present certain limitations, their short computation time proves to be helpful for a quick sketch of the force spectrum in the machine. However, for more accurate calculations, the use of finite element methods (FEM) is more appropriate, although the computation time is considerably increased. The developments in computing technology through the years has contributed to spread the use of FEM packages for electromagnetic an mechanical analyses, among others. Since the noise problem in electrical machines is a consequence of the interaction between electromagnetic and me-

chanical forces, both packages need to be used together. In this way, Ishibashi et al. (1998) presented an algorithm to predict the shape of the vibration modes of the motor at no load, combining electromagnetic and mechanical FEM analyses. It was found that the vibration response of one mode depends on the mode of the nearby natural frequency, and not on the mode of the electromagnetic force wave.

The use of FEM is mainly limited to low frequencies and repetencies, since the number of elements increases in a quadratic way. For higher values, a new method suitable for calculations of noise and vibration in electrical machines was developed by Wang et al. (2000). The method was called statistical energy analysis (SEA), commonly used for ship and aircraft structures but not earlier applied to electrical machines. The main idea is to divide the whole structure into groups of components presenting similar modal energy storage and then estimate the vibration energy of each subsystem by solving the energy balance equations which relate the power flow from one subsystem to another. In the case of induction machines these structures correspond to those ones presenting similar modes of vibration.

Influence of the modulation strategies

The electromagnetic noise component acquired a great importance with the arrival of converters. Many research efforts were directed towards the manipulation of the switching pattern so as to mismatch the new harmonics introduced in the currents from the natural resonant frequencies of the machine structure, which proved to be the cause of increasing noise in the new drives (Belmans et al., 1991). One of the most wide spread modulation techniques is *pulse width modulation* (PWM), where the states of the switches are selected by comparing the actual value of the command signal, which is output from a regulator, with a constant frequency carrier wave. Increasing the switching frequency above the audible spectrum range (20 Hz - 20 kHz) would indeed reduce the noise perceived from the motor, but drawbacks appear in the converter instead. Switching faster involves an increase of the power lost in the switches as well as the amount of electromagnetic noise produced by the converter. In order to avoid these side effects the switching frequency should be maintained between the range from 3 kHz up to 12 kHz, where the human ear is still quite sensitive. Increasing the switching frequency may also contribute to the appearance of strong subharmonics, causing more single tones, which are perceived as highly

disturbing by the human ear (Belmans and Hameyer, 1998). An alternative to PWM is *pulse frequency modulation* (PFM), where the frequency of the carrier wave is changed continuously in order to spread the harmonic components over the whole spectrum. The results obtained using this technique showed a better acoustical response compared to PWM, as described in Stemmler and Eilinger (1994). The frequency can be changed in a random fashion (*random modulation*) or among some predetermined values, selected in a way that they do not interact with any of the natural resonant frequencies of the motor, and this idea was successfully tested by Bologniani et al. (1999).

In the last decade new control strategies have been developed in order to achieve better performance in the drives. As a consequence, the switching pattern in the converter is modified, which in turn results in a different acoustical response. The noise emissions from a direct torque controlled (DTC) drive are analyzed in Xu et al. (2000). It was shown that DTC controlled drives have similar spread spectrum features as in the case of random PWM modulation, which is generally regarded as less irritating. However, the wideband of their harmonic spectra is more likely to induce mechanical resonances, which sometimes may lead to higher noise emissions. The noise level was now increased with the load, although an optimal flux level providing minimal noise was found. A comparison between the noise behaviour when the flux and the torque are modulated in vector controlled induction motor drives was presented by Martínez Muñoz et al. (1999), showing that the drive is more sensitive to flux modulation. However, further studies were needed to determine how the force pattern in the airgap was influenced by flux and torque modulation.

Noise reduction techniques

A means to reduce the noise by arranging the winding in the machine was presented in Hupe and Kennel (1989). Two inverters were used to drive a large induction machine equipped with two separate windings. The noise and the current ripple were reduced by triggering two PWM inverters with inverse pulses so that the switching frequency harmonic voltages are in antiphase. This method is only practical for very high power rating induction machine drives. For smaller motors a similar configuration was described in Chau et al. (2000) where an increase in the power and a reduction of the noise was achieved by purposely selecting the phase of the two carriers of the dual inverters, depending on the number of poles used at different machine operations.

The advantages of using magnetic bearings over conventional ones in order to reduce the noise emissions has been reported in Maliti (2000). Active noise control can also be applied for noise reduction in electrical machines (Belkhayat et al., 1997). In order to suppress some magnetic noise components, it is possible to inject into the stator a number of current harmonics, which magnitudes and phases can be controlled, and their frequencies are linked to the rotation speed. If one of the force waves has the same magnitude, frequency and mode number than a natural one but is in opposite phase, thus the two force waves will nullify and the corresponding magnetic noise will disappear. However, the process of active noise reduction is considerably expensive since it requires a microphone, sensors and advanced control tools for real time processing.

1.2 Objectives and contributions of the thesis

Although the acoustic influence of different modulation strategies such as DTC, PWM and PFM is available in the literature, there is a lack of studies treating the acoustic problem in vector controlled drives. Since the use of this control strategy is widely spread in electrical drives, therefore the importance of examining its noise emissions. Hence, the major objective of the thesis is to provide an understanding of the mechanisms responsible for the noise emissions when the vector control strategy is used in induction motor drives. With this purpose, a digital drive system has been developed for a 2.2 kW induction motor, and this tool has been used for the experimental evaluation of the noise emissions when the flux and/or the torque are modulated with high frequency noise signals.

Another objective of this work is to develop a method for the prediction of the noise emissions of electromagnetic origin, combining different simulation packages. In this way, the acoustic behaviour of a machine design using a certain control strategy could be studied and optimized without the need of building a prototype. The different stages of the process, from the controller to the motor, have been implemented in SIMULINK, where the line currents feeding the machine are obtained. These currents are introduced into an electromagnetic FEM package, where the test motor is modelled and the airgap forces are calculated. In order to obtain the spectrum of the forces around the motor, a high number of simulations have to be performed, at different points in time, using a transient solver. The modal behaviour of the machine is calculated through a structural analysis using another FEM software, and this structural work was performed by Wang (1998). A brief discussion of his work is included in this

thesis, since it constitutes an important step in the noise prediction process. Finally, the electromagnetic and modal information is introduced in a BEM package, where the noise radiation is computed.

The nature of vector control links the modulation of the currents to a characteristic force distribution in the machine, where the influence of radial and tangential forces may be weighted in order to develop suitable structural changes so as to reduce the noise emissions. A study of some structural changes in the conventional stator of an electrical machine has been conducted with this objective. In particular, the effect of introducing air gap layers around the outer part of the stator core in order to interfere with the natural transmission path of the vibrations has been analyzed.

1.3 Outline of the thesis

The material of this thesis is divided into seven chapters. In this first Chapter, a general literature review dealing with aspects of noise generation in electrical machines has been presented. An overview of the major contributions studying the influence of the different parts of the machine structure in the noise emissions was presented first, followed by the most relevant studies concerning the analytical and FEM electromagnetic force computation presented in recent years. The influence of different modulation strategies in the overall emissions was also treated as well as the methods proposed for the noise reduction in electrical machines.

In Chapter 2, the theory behind vector control is introduced. The practical implementation of this theory in a digital control system is explained, and its dynamic capabilities are demonstrated in a musical application. This system is used for the experiments presented in Chapter 5.

In Chapter 3, an analytical computation of the radial airgap forces in the test motor is discussed. The method assumes ideal iron, and the slotting effects are also modelled. The method is validated with the results obtained from FEM simulations when linear materials are used, and the corresponding non linear results are also included.

In Chapter 4, a noise prediction using finite and boundary element modelling is proposed. This chapter consists of three parts. In the first one, a previous study of the structural behaviour of the test motor is discussed. The structural models as well as the conclusions from this previous study constitute the basis from where the electromagnetic and acoustic calculations are devel-

oped in the other two parts. The electromagnetic force for a given current modulation is computed in the second part, and these forces are used to excite the acoustic model and obtain the noise emissions, which are included in the third part.

In Chapter 5, the results from the measurements are presented. Sound pressure measurements were conducted inside an anechoic chamber with the machine at stand still, in four different positions, as well as at a low rotational speed under no load and load conditions. Sound power measurements were conducted using the sound intensity technique, with the machine rotating in order to average the results, also under no load and load conditions.

In Chapter 6, a study of several structural changes in the stator core of an electrical machine, with the aim of reducing the noise emissions, is discussed. The study was performed using finite and boundary element methods and it serves as a complement to previous experimental works developed using a similar concept.

In Chapter 7, a summary of the most important results and conclusions of the thesis is presented. It also contains some suggestions for possible future work in this area.

Four appendices are included at the end of the thesis. Appendix A presents the experimental calculation of the modal parameters of a one axis symmetric plate, which serves for the learning and understanding of the methods presented in the first part of Chapter 4. Appendix B deals with a noise prediction conducted with the same plate, and it is useful as an introduction to the second and third parts in Chapter 4. The results from the sound intensity measurements at no load and load are included in Appendices C and D, and they support the validity of the sound power results presented in Chapter 5.

Chapter 2

Control

2.1 Introduction to Vector Control

Electrically driven industrial and household applications most often require the flexibility of adjusting the speed of the process depending on the demands. This is achieved by means of rapid changes in the shaft torque of the electrical machine incorporated in the drive. In the past, d.c. motors were used extensively in variable-speed drives since their flux and torque could be easily controlled by the field and armature currents respectively. However, the commutator and the brushes in a d.c. motor lead to additional maintenance costs. This is a major drawback compared with alternating current machines, which present the advantage of having smaller dimensions and therefore higher output ratings for low weight and low rotating mass. The developments in the fields of power electronics and computing capability in the last 15 years brought cheaper and more sophisticated converters and digital signal processors (DSP), which made possible the incorporation of a.c. motors into variable speed drives, where new control strategies could be implemented.

The conventional way of controlling the voltages fed into the motor from a frequency converter is to maintain constant the ratio between the amplitude of the voltage and its frequency, i.e. the flux in the machine. With these drives, more commonly known as 'v/f drives', the ratio of the supply frequency to the motor voltage can be increased in the converter, which also increases the slip. This in turn leads to a higher induced voltage in the rotor and subsequently to a larger rotor current. This process is to a large extent dictated by the large rotor time constant, which implies that rapid torque changes are difficult to

implement using a conventional controller.

In order to achieve better transient response, a new control strategy known as 'vector control' was introduced. The basic principle is that the alternating currents in the machine can be expressed as a rotating vector, and by controlling the amplitude and the phase of this vector, both the amplitude of the flux and the torque can be changed independently. Hence, the dynamics of the machine are set directly by controlling the currents, as in the case of the d.c. motor. However, in an a.c. machine the process is more complicated since not only the modulus of the current vector but also its phase has to be controlled. The control problem of an a.c. motor would then be reduced to the same case as for the d.c. motor if the current vector could be seen as stationary from a proper coordinate system.

The current vector rotates with the synchronous speed ω_s, and the flux in the machine rotates with the same frequency although 'delayed' in phase with respect to the current under a certain load. An observer that is oriented towards the flux vector will see a constant current vector, which can be expressed as a combination of two d.c. components, one pointing in the same direction as the flux vector and the other perpendicular to this direction, as shown in Figure 2.1. Two different coordinate systems can be distinguished. On one hand the $\alpha\beta$

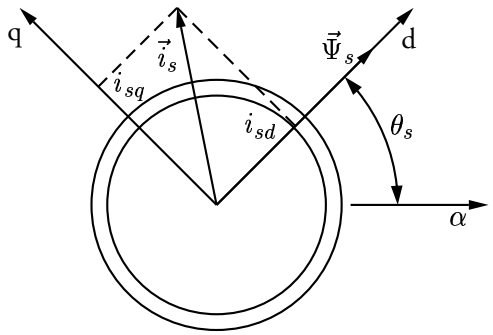

Figure 2.1: Stator flux oriented model.

system which is stationary and is fixed to the stator structure of the motor. On the other hand the dq system, rotating with the speed ω_s, where the direct axis d coincides with the stator flux vector (or the rotor flux vector, depending on the control strategy) and the quadrature axis q lies perpendicular to this

vector. The stator current $\vec{i}_s$ has two components: i_{sd} along the d-axis, which is the magnetizing component of the current that controls the magnitude of the flux in the machine; and i_{sq} along the q-axis which controls the phase change and thus the speed of the flux vector. In most cases the direct current will be constant, except in the field weakening region. In general, the torque produced in any a.c. machine is expressed as (Krause, 1986):

$$T_e(t) = \frac{3p}{2K^2} \left[\psi_{sd}(t) i_{sq}(t) - \psi_{sq}(t) i_{sd}(t)\right] \tag{2.1}$$

where p represents the number of pole pairs and K is a scaling constant of the space vector. In an asynchronous machine ψ_{sq} is zero, while ψ_{sd} is maintained constant, so the torque can directly be controlled by changing i_{sq}. While in v/f drives the torque and flux response are coupled with each other, using vector control allows independent control of the currents governing the torque and the flux in an induction motor, and the transient response characteristics become similar to those of separately excited d.c. machines. In terms of control, the 'd.c.' nature of the direct and quadrature currents in an a.c. motor suggests some sort of similarity with the control of d.c. machines. In fact, i_{sd} and i_{sq} correspond to the field and the armature currents respectively in a d.c. motor, and the stationary field imposes a fixed current distribution in the rotor, as shown in Figure 2.2(a). A similar current distribution appears in the rotor of an induction motor under load, with the difference that this distribution is shifted continuously, driven by the time varying stator flux, see Figure 2.2(b). However, an observer placed in the rotating dq system will see a stationary distribution, as in the case of the d.c. motor. Under zero slip conditions, the rotor current is negligible in an induction motor, and only a direct axis current distribution will appear, as shown in Figure 2.3(a). When a load is applied, the slip increases and a quadrature current is induced in the rotor, which must be compensated by an additional stator current, as indicated in Figure 2.3(b), and the sum of the current from the rotor and the stator for the quadrature axis must be close to zero. The resultant current distribution in the stator winding is found by the superposition of the direct and quadrature current distributions. In order to change the torque, the instantaneous three phase currents are changed so that a certain quadrature current is produced, while the direct current remains unchanged. In case that a transient error appears in i_{sd}, that will not result in any significant flux transient, since the flux dynamics are slow. This decoupled response between flux and torque control constitutes the main advantage of

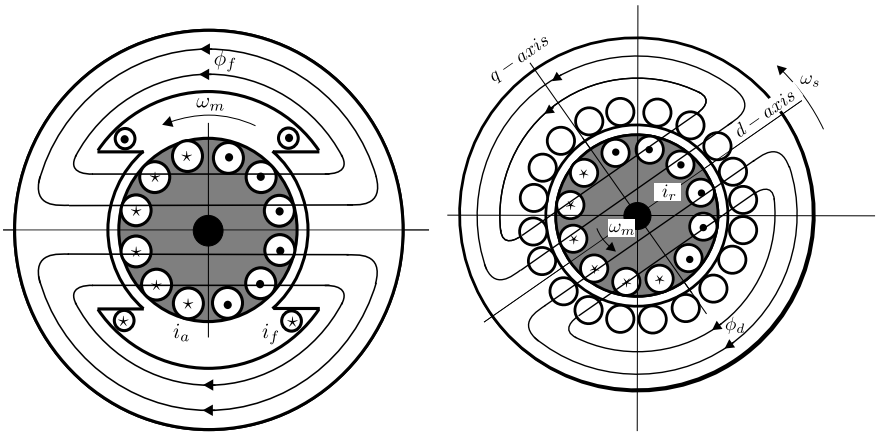

(a) D.C. motor (b) Induction motor

Figure 2.2: D.C. and Induction motor structures.

vector controlled drives compared to v/f drives, improving the response under transient conditions. However, the behaviour of both drives should be similar under steady state operation. Vector drives are most frequently used with a speed control loop where the torque reference is continually adjusted, in what could be defined as a quasi-continuous transient operation. The advantages of vector control both in ease of control and faster transient response have increased the range of applications where vector drives are being used and thus, the implications of using this type of drive in terms of acoustic noise emissions must, as a result of this market trend, be examined and compared with competing solutions.

2.2 Noise emissions in vector controlled drives

The electromagnetic noise emissions in an electric motor are directly determined by the harmonic content of the relevant forces in the airgap of the machine, where the electro-mechanic energy conversion takes place. Every structure tends to vibrate at certain frequencies with a characteristic deformation, which is inherent to that frequency. These frequencies are called 'resonance fre-

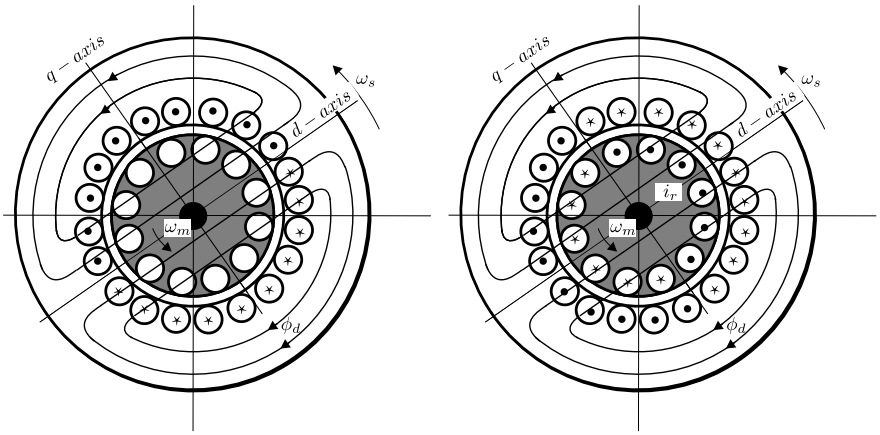

(a) Direct axis current distribution.

(b) Quadrature axis current distribution.

Figure 2.3: Field oriented current distributions in the induction motor.

quencies' and the characteristic deformations correspond to the 'modes of vibration'. When the frequency of one harmonic in the airgap force coincides with one of the resonance frequencies of the stator, it vibrates with that frequency in a certain fashion producing noise. It is important to note that not only the amplitudes of the airgap force harmonics determine the noise emissions, but also their frequencies. A small force with a frequency corresponding to one resonance will produce much more noise than a greater force not matching any of the resonance frequencies of the structure.

The harmonic content of the airgap forces is directly determined by the harmonics present in the motor currents as well as other construction factors such as the effects of the slots, eccentricity... It is not the aim of this work to analyze the influence of such construction factors, but to experimentally determine how the motor responds acoustically to different current excitations using vector control, and try to verify these measurements with the aid of computational tools. The capability of decoupling the stator current in two components, one of them in the radial direction (d-current), controlling the flux, and the other in the tangential direction (q-current), controlling the torque, would allow to

measure the difference in the motor acoustic behaviour when the flux or the torque are modulated, as well as it would provide information about the role that radial and tangential forces play in the overall acoustic emissions.

The desired excitation can be achieved by adding to the reference direct and/or quadrature currents an external a.c. signal, that could be a sine wave with a certain amplitude and with a frequency corresponding to one of the natural frequencies of the stator, which is the part of the motor mainly responsible for the sound radiation into the surrounding areas. When this 'extra noise' is added to the direct current, the amplitude of the current vector will vary in a sinusoidal fashion along the radial direction, providing that the quadrature current is set to zero, and thus exciting the stator with pure radial forces. If the extra noise is added to the quadrature current instead, while the direct current is maintained constant to keep the flux in the machine, the flux vector will rotate around the direct axis, provided that no net quadrature current exists, i.e. no average torque is produced. The forces exciting the stator will now be a combination of radial and tangential components. The radial component is due to the already existing direct current (which may be modulated or not) and the tangential component is produced by the phase shift of the flux vector. Hence, while it is possible to electrically excite the structure with pure radial forces, by modulating the direct current and setting the quadrature current to zero, it is not possible to produce pure tangential forces by modulating the quadrature current, since the direct current can not be set to zero as the magnetization would disappear. Figure 2.4 illustrates how the stator is excited and the force pattern in the air gap when modulating the torque and the flux.

2.3 Stator flux control

The aim of this section is to show how the principles of vector control can be applied to asynchronous machines and how to deduce a controller for the direct and the quadrature currents. In general, depending on the variable that has to be controlled in the motor, different stages can be differentiated in the control of electrical machines which can be represented as cascade loops interacting with each other, as showed in Figure 2.5. In the inner loop, current control is implemented and the set point for the controller is determined by the speed loop, which in turn is governed by the position loop. Current and speed control are the most commonly demanded features in induction machines whereas other kind of motors present better performance for position control applica-

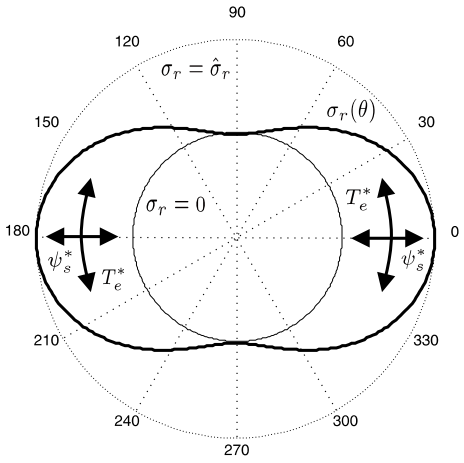

Figure 2.4: Airgap stress distribution and stator excitation under flux and torque modulation.

tions. Measuring the current is not a complicated task whereas the speed is measured by a tachometer and more often estimated using observers that provide sufficient accuracy for most practical applications. The current controller outputs the control signal u^* that will determine the magnitude and phase of the currents feeding the motor in order to achieve the required torque or speed response. For simplicity reasons, the conversion of the control signal into the machine phase voltages have been symbolically grouped under the 'decoding' (Dcf) box.

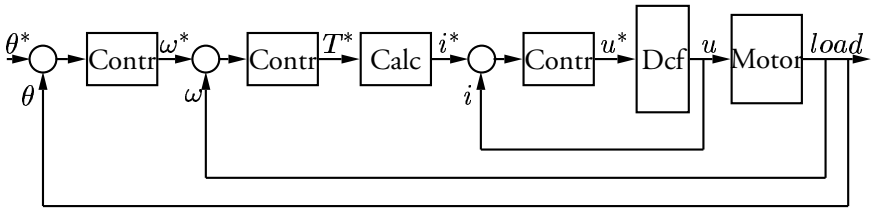

Figure 2.5: Cascade control.

The electrical behaviour of an asynchronous motor can be simplified in

terms of an electrical circuit and there are namely two ways of representing the equivalent diagram of an induction motor, depending on the number of parameters taken into account. The five parameter model is presented in Figure 2.6, where the steady state value R_r/s has been replaced by the rotor resistance in series with a voltage source which corresponds to the back EMF. In the equivalent four parameter model the rotor and stator leakage inductances are grouped together in the stator side, as shown in Figure 2.7.

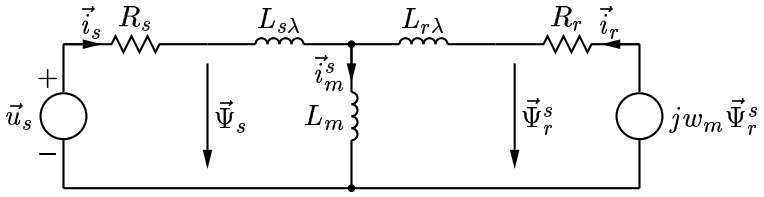

Figure 2.6: Five parameter model.

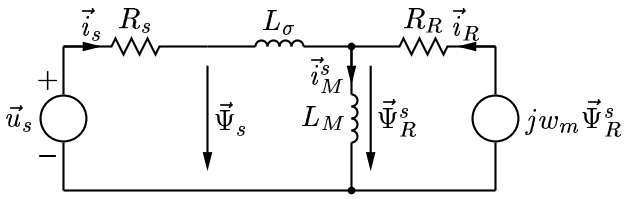

Figure 2.7: Four parameter model.

The parameters in both models are related in the following way:

$$R_R = \left(\frac{L_m}{L_r}\right)^2 \cdot R_r \tag{2.2}$$

$$L_M = \frac{L_m^2}{L_r} \tag{2.3}$$

$$L_\sigma = \sigma L_s \tag{2.4}$$

$$\sigma = 1 - \frac{L_m^2}{L_s L_r} \tag{2.5}$$

In this chapter, the four parameter model will be used to deduce the parameters in the controllers for the direct and the quadrature currents. The

procedure to follow can assume that either the rotor or the stator flux vector coincides with the direction of the direct axis. Since measuring the stator currents and estimating the stator flux is more convenient than the rotor flux and currents, the stator flux model represented in Figure 2.1 will be followed. In the stationary $\alpha\beta$ coordinate system the stator voltage can be written in vector form as follows:

$$\vec{u}_s^{\alpha\beta}(t) = R_s \vec{i}_s^{\alpha\beta}(t) + \frac{d\vec{\psi}_s^{\alpha\beta}(t)}{dt} \tag{2.6}$$

This equation can be transformed into the synchronous dq reference frame where the direct axis is aligned with the stator flux vector, which sets the speed of rotation ω_s. The rotor will rotate with the electrical speed ω_m and the slip frequency becomes $\omega_{sl} = \omega_s - \omega_m$. The stator voltage in synchronous coordinates is expressed as:

$$\vec{u}_s^{dq}(t) = R_s \vec{i}_s^{dq}(t) + \frac{d\vec{\psi}_s^{dq}(t)}{dt} + j\omega_s \vec{\psi}_s^{dq}(t) \tag{2.7}$$

The voltage can be separated in its direct and quadrature components, introducing that $\psi_{sq} = 0$ and $\psi_{sd} = \psi_s$ for the coordinate system selected:

$$u_{sd}(t) = R_s i_{sd}(t) + \frac{d\psi_s(t)}{dt} \tag{2.8}$$

$$u_{sq}(t) = R_s i_{sq}(t) + \omega_s \psi_s(t) \tag{2.9}$$

Based on this equations, the direct and quadrature current controllers will be deduced separately, following the strategy of 'predictive dead beat control' (Alaküla et al., 1995).

2.4 Controller for the direct current

Predictive dead beat control assumes that the reference value for one signal (denoted in the following by the superscript '*') set at one discrete time t_k is achieved by the actual value of the signal with one sampling time delay, i.e. at time t_{k+1}. For the voltage signal this implies that $u_{sd}^*(t_k) = \overline{u}_{sd}(t_{k+1})$. The average voltage at time t_{k+1} can be expressed as a moving average filter of the form:

$$\overline{u}_{sd}(t_{k+1}) = \frac{1}{T_s} \int_{t_k}^{t_{k+1}} u_{sd}(\tau) d\tau \tag{2.10}$$

Introducing 2.8 into this equivalence and multiplying by the sampling time T_s leads to:

$$T_s u^*_{sd}(t_k) = R_s T_s \frac{1}{T_s} \int_{t_k}^{t_{k+1}} i_{sd}(\tau) d\tau + \psi_s(t_{k+1}) - \psi_s(t_k) \tag{2.11}$$

where the derivative of the flux has been approximated with a forward difference, using Euler's method. The average value of the current within one sampling interval is denoted by $\overline{i}_{sd}(t_{k+1})$, following the same equivalence as for the voltage in expression 2.10. Assuming that the current varies linearly within one sampling interval, it can be approximated as follows:

$$\overline{i}_{sd}(t_{k+1}) \simeq \frac{i_{sd}(t_{k+1}) + i_{sd}(t_k)}{2} \tag{2.12}$$

If the leakage inductance is neglected, the flux is expressed as $\psi_s \simeq i_{sd} L_M$. For dead beat control $i_{sd}(t_{k+1}) = i^*_{sd}(t_k)$ and introducing these changes into expression 2.11 yields:

$$T_s u^*_{sd}(t_k) = \frac{R_s T_s}{2} \left[i^*_{sd}(t_k) + i_{sd}(t_k) \right] + i^*_{sd}(t_k) - i_{sd}(t_k) \tag{2.13}$$

This expression can be transformed using the following equivalence:

$$\frac{R_s T_s}{2} = R_s T_s - \frac{R_s T_s}{2} \tag{2.14}$$

which leads to the expression below:

$$T_s v^*_{sd}(t_k) = R_s T_s i_{sd}(t_k) + \left(L_M + \frac{R_s T_s}{2} \right) \left[i^*_{sd}(t_k) - i_{sd}(t_k) \right] \tag{2.15}$$

Assuming dead beat control, the current at one point in time t_k can be written as the sum of all the set point changes up to the time t_{k-1}:

$$i_{sd}(t_k) = \sum_{j=0}^{j=k-1} \left[i^*_{sd}(t_j) - i_{sd}(t_j) \right] \tag{2.16}$$

and the final expression for the direct current controller takes the following form:

$$T_s v^*_{sd}(t_k) = R_s T_s \sum_{j=0}^{j=k-1} [i^*_{sd}(t_j) - i_{sd}(t_j)] + \\ + \left(L_M + \frac{R_s T_s}{2} \right) [i^*_{sd}(t_k) - i_{sd}(t_k)] \tag{2.17}$$

This controller can be implemented as a PI controller with a proportional gain equal to $L_M + \frac{R_s T_s}{2}$ and an integral gain equal to $R_s T_s$. The actual value of the direct current is obtained from the flux level in the machine, which is difficult to measure. As an alternative, this flux can be estimated as will be presented later in this chapter.

2.5 Controller for the quadrature current

Expression 2.9 for the quadrature current can be transformed into 2.18 using the equivalence that the synchronous speed ω_s is the sum of both the slip and rotor electrical frequencies, ω_{sl} and ω_m respectively.

$$u_{sq} = R_s i_{sq} + \omega_{sl} \psi_s + \omega_m \psi_s \tag{2.18}$$

In order to deduce an expression for the slip frequency, it is helpful to consider the rotor equation, which in stationary coordinates takes the form below:

$$-j\omega_m \vec{\psi}^{\alpha\beta}_R + \vec{i}^{\alpha\beta}_R R_R + \frac{d\vec{\psi}^{\alpha\beta}_R}{dt} = 0 \tag{2.19}$$

This equation is translated into the synchronous dq reference frame:

$$\frac{d\vec{\psi}^{dq}_R}{dt} + j(\omega_s - \omega_m)\vec{\psi}^{dq}_R + \vec{i}^{dq}_R R_R = 0 \tag{2.20}$$

where the rotor flux and current in synchronous coordinates are written as:

$$\vec{\psi}^{dq}_R = \vec{\psi}^{dq}_s - \vec{i}^{dq}_s L_\sigma \tag{2.21}$$

$$\vec{i}^{dq}_R = \frac{\vec{\psi}^{dq}_R}{L_M} - \vec{i}^{dq}_s \tag{2.22}$$

The rotor current can be expressed in terms of stator variables substituting 2.21 in 2.22, and introducing the equivalence $L_s = L_M + L_\sigma$, where L_s is the stator inductance, L_M is the magnetizing inductance and L_σ is the combined leakage inductance from the stator and the rotor in the four parameter model:

$$\vec{i}_R^{dq} = \frac{\vec{\psi}_s^{dq}}{L_M} - \frac{L_s}{L_M}\vec{i}_s^{dq} \tag{2.23}$$

Introducing expressions 2.21 and 2.23 into 2.20 yields:

$$\frac{d\vec{\psi}_s^{dq}}{dt} - L_\sigma \frac{d\vec{i}_s^{dq}}{dt} + j\omega_{sl}\left(\vec{\psi}_s^{dq} - \vec{i}_s^{dq}L_\sigma\right) + \\ + \frac{R_R}{L_M}\vec{\psi}_s^{dq} - \frac{R_R L_s}{L_M}\vec{i}_s^{dq} = 0 \tag{2.24}$$

This expression can be divided into a real and an imaginary part, still considering that $\psi_{sq} = 0$ for the reference system selected, as follows:

$$\frac{d\psi_s}{dt} - L_\sigma \frac{di_{sd}}{dt} + \omega_{sl} i_{sq} L_\sigma + \frac{R_R}{L_M}\psi_s - \frac{R_R L_s}{L_M} i_{sd} = 0 \tag{2.25}$$

$$-L_\sigma \frac{di_{sq}}{dt} + \omega_{sl}\left(\psi_s - L_\sigma i_{sd}\right) - \frac{R_R L_s}{L_M} i_{sq} = 0 \tag{2.26}$$

From equation 2.26 the slip frequency is obtained, assuming that $\psi_s - L_\sigma i_{sd} \simeq \psi_s$ since the leakage flux can be neglected compared to the linkage flux in the machine:

$$\omega_{sl} = \frac{\frac{R_R L_s}{L_M} i_{sq} + L_\sigma \frac{di_{sq}}{dt}}{\psi_s} \tag{2.27}$$

Substituting equation 2.27 into 2.18 leads to:

$$u_{sq} = \left(R_s + \frac{R_R L_s}{L_M}\right) i_{sq} + L_\sigma \frac{di_{sq}}{dt} + \omega_m \psi_s \tag{2.28}$$

In the same way as for the direct voltage, $u_{sq}^*(t_k) = \overline{u}_{sq}(t_{k+1})$ where the quadrature voltage is averaged using a moving average filter of the form shown

in expression 2.10. Introducing equation 2.28 in the expression for the moving average filter and multiplying by the sampling time T_s yields:

$$T_s u^*_{sq}(t_k) = \left(R_s + \frac{R_R L_s}{L_M}\right) T_s \frac{1}{T_s} \int_{t_k}^{t_{k+1}} i_{sq}(\tau) d\tau +$$

$$+ L_\sigma [i_{sq}(t_{k+1}) - i_{sq}(t_k)] + T_s \frac{1}{T_s} \int_{t_k}^{t_{k+1}} \omega_m(\tau) \psi_s(\tau) d\tau \qquad (2.29)$$

where the derivative of the current has been approximated with a forward difference, using Euler's method. The integral of the quadrature current divided by the sampling time becomes $\overline{i}_{sq}(t_{k+1})$ which can be approximated as in equation 2.12 for the direct current. Another approximation is applied to the speed dependent term as follows:

$$\frac{1}{T_s} \int_{t_k}^{t_{k+1}} \omega_m(\tau) \psi_s(\tau) d\tau \simeq \omega_m(t_k) \psi_s(t_k) \qquad (2.30)$$

If the main flux and the speed change, they do it slowly and these components can be assumed to be constant during one sampling period. Assuming dead beat control for the quadrature current leads to:

$$i_{sq}(t_k) = \sum_{j=0}^{j=k-1} \left[i^*_{sq}(t_j) - i_{sq}(t_j)\right] \qquad (2.31)$$

Taking into consideration all these assumptions, equation 2.29 can be rewritten in the following form:

$$T_s u^*_{sq}(t_k) = \left(R_s + \frac{R_R L_s}{L_M}\right) T_s \sum_{j=0}^{j=k-1} \left[i^*_{sq}(t_j) - i_{sq}(t_j)\right] +$$

$$+ \left[L_\sigma + \left(R_s + \frac{R_R L_s}{L_M}\right) \frac{T_s}{2}\right] \left[i^*_{sq}(t_k) - i_{sq}(t_k)\right] +$$

$$+ \omega_m(t_k) \psi_s(t_k) T_s \qquad (2.32)$$

As well as for the direct current, the controller for the quadrature current can be implemented as a PI controller, now with a proportional gain equal to

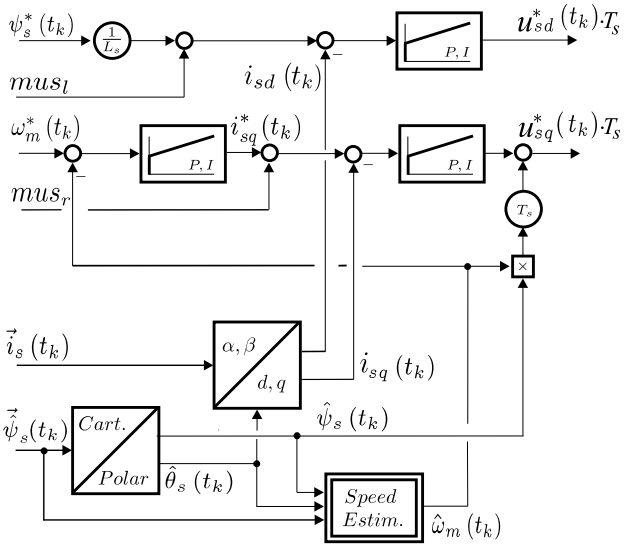

Figure 2.8: Controller structure.

$L_\sigma + \left(R_s + \frac{R_R L_s}{L_M}\right)\frac{T_s}{2}$ and an integral gain equal to $\left(R_s + \frac{R_R L_s}{L_M}\right)T_s$, plus the feed forward term $\omega_m(t_k)\psi_s(t_k)T_s$ which depends on the speed of the machine. This controller assumes as an input the reference value of the quadrature current, which can be easily obtained from the torque equation using the *amplitude invariant* transformation, as shown below, where only the flux has to be estimated, as in the case of the direct controller.

$$i_{sq}^*(t_k) = \frac{2}{3}\frac{T_e^*(t_k)}{\psi_s(t_k)} \tag{2.33}$$

2.6 Implementation

The complete controller structure is presented in Figure 2.8. The set point value for the direct current results from the addition of two signals: the magnetizing current, obtained as the reference flux divided by the stator inductance, and an external noise signal defined as mus_l. The reference value for the quadrature current is set by a speed controller, and another noise signal mus_r is added. The measured three phase currents in the motor are input into the controller

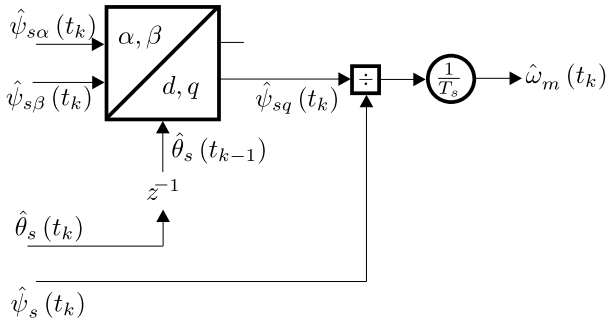

Figure 2.9: Speed observer.

in stationary coordinates and then transformed to the synchronous frame. This transformation is achieved by estimating the angle of rotation $\hat{\theta}_s$ from the flux vector as follows:

$$|\psi_s| = \sqrt{\psi_{s\alpha}^2 + \psi_{s\beta}^2} \qquad \cos\hat{\theta}_s = \frac{\psi_{s\alpha}}{|\psi_s|} \qquad \sin\hat{\theta}_s = \frac{\psi_{s\beta}}{|\psi_s|} \tag{2.34}$$

In order to get the maximum noise radiation from the stator structure, the noise signals mus_l and mus_r are selected to be sine waves with a frequency corresponding to one of the natural frequencies of the stator. As saturation should be avoided, the magnetizing current will be reduced in the same ratio as the amplitude of the added noise signal, so that the direct current plus the a.c. noise signal does not exceed the value of the current corresponding to the nominal flux in the machine. In practice it is enough to reduce the mean value of the flux no further than 10 per cent of its nominal value, since operating close to a resonance frequency increases the radiation efficiency of the structure for a relatively small amplitude of the exciting force. The noise signals can contain passages with a d.c. offset, which added to the quadrature current component will cause the rotor to accelerate since a non zero average torque will be produced. This phenomenon can be avoided by implementing a speed control loop, where the actual speed is estimated from the flux vector, as shown in Figure 2.9.

The speed of rotation of the flux vector is approximated as the rate of change of the quadrature component of the flux during one sampling interval with respect to its modulus. Figure 2.10 shows the path followed by the flux vector

between two consecutive samples. At time t_{k-1} the synchronous frame is rotated so that the direct axis d_{k-1} is aligned with the position of the flux sampled at that time, $\vec{\psi}_{k-1}$. The flux vector will continue rotating but its actual position will not be read until the next sample at time t_k, when the synchronous frame is again rotated so that the new direct axis d_k coincides with the new sampled flux $\vec{\psi}_k$. An observer placed in the old synchronous frame d/q_{k-1} will see that the flux vector was rotated by an additional quadrature component ψ_{qk}. The flux at time t_k can be expressed in the old coordinate system as the sum of a direct component $|\vec{\psi}_{k-1}| \equiv |\vec{\psi}_k|$, and a quadrature component ψ_{qk}. The angle of rotation between the two samples is approximated as:

$$\delta = \theta_k - \theta_{k-1} = \frac{\psi_{qk}}{|\vec{\psi}_k|} \tag{2.35}$$

The speed of rotation of the flux vector is calculated as the derivative of δ, which in a sampled system can be approximated as $\frac{\delta}{T_s}$, where T_s is the sampling time. This is actually the process described in Figure 2.9, where the quadrature component of the flux is obtained using in the transformation the angle corresponding to the old synchronous frame, which is easily stored working in a digital system.

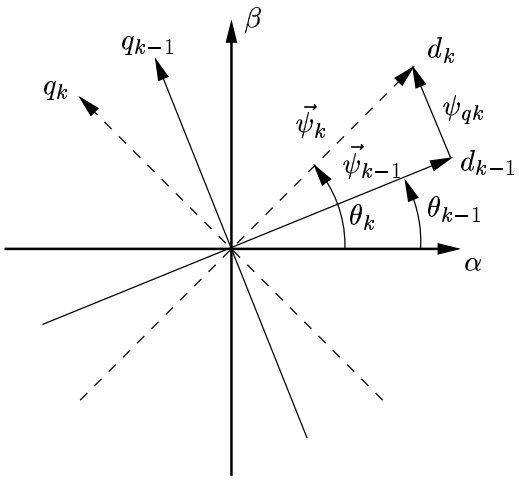

Figure 2.10: Flux vector path.

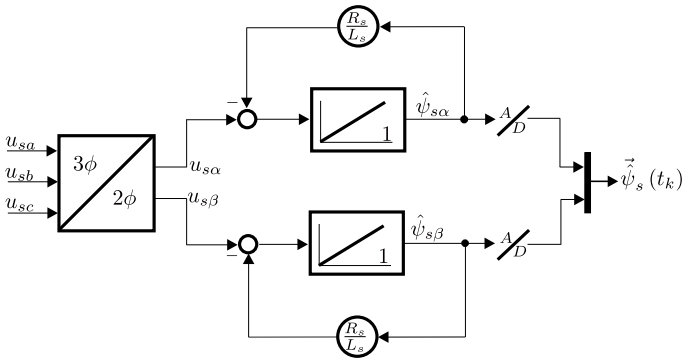

Figure 2.11: Flux observer.

The flux is estimated by substituting the stator current $\vec{i}_s^{\alpha\beta} \simeq \frac{\vec{\psi}_s^{\alpha\beta}}{Ls}$ into the stator equation 2.6, leading to the following expression of a low pass filter:

$$\vec{u}_s^{\alpha\beta} = \frac{R_s}{L_s}\vec{\psi}_s^{\alpha\beta} + \frac{d\vec{\psi}_s^{\alpha\beta}}{dt} \tag{2.36}$$

The three phase voltages are transformed into the stationary frame and equation 2.36 is implemented in an analog circuit as shown in Figure 2.11. The control system and the whole process were implemented in SIMULINK, and the overall structure is presented in Figure 2.12. The voltage time area output from the controller in stationary coordinates is transformed into three phases which are symmetrized in order to increase the modulation depth of the drive, by centring the reference voltages with respect to the bus voltage window (Holmes, 1997). The switches in the converter are controlled by the modulator, where regularly sampled sine-triangle modulation is used. Since the model of the induction motor is based on the stator and rotor equations in stationary coordinates, the three phase voltage output from the converter have to be transformed back to stationary coordinates in the simulation. From the motor model, the measured current is fed back to the controller, and from the applied voltage the flux and the speed are estimated in the observer. The external noise signals for the direct and the quadrature current are the controller inputs named as mus_l and mus_r respectively.

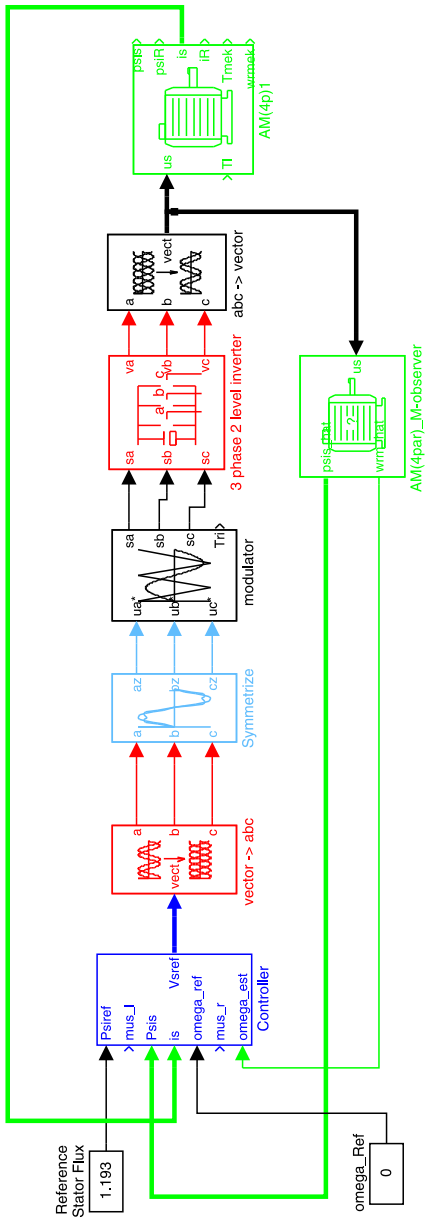

Figure 2.12: Structure of the 'musical' drive.

2.7 Musical drive test

An indication of the torque response to a given music sequence was obtained from the simulated results using the structure showed in Figure 2.12. In this case the audio signal is fed into the torque modulation input mus_r, while mus_l is set to zero. The input signal and simulated torque response are given in figures 2.13(a) and 2.13(b). The results provide an overall indication in terms of the ability of the motor torque to track the sound signal.

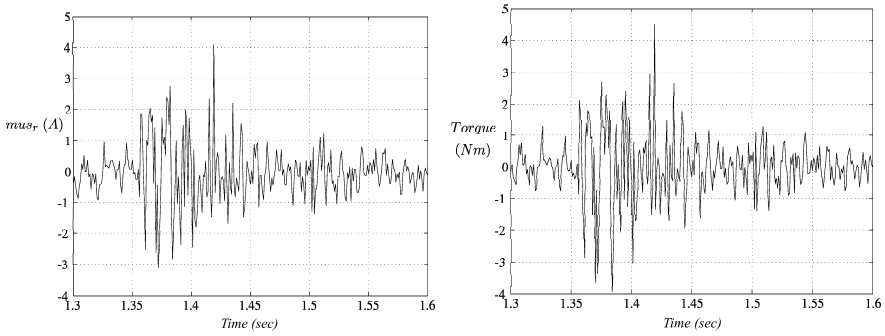

(a) Music input sequence.

(b) Torque response.

Figure 2.13: Music input and torque response for $mus_r(t)$, $mus_l = 0$.

The performance of the drive has also been experimentally tested. The drive developed consists of a commercial inverter which was re-fitted with a new controller and pulse width modulation boards. The control, vector transformation and symmetrization modules from Figure 2.12 are implemented in software and reside on a dedicated DSP board. The modulator unit, which has a carrier frequency of 19.582 kHz, produces regularly symmetrically sampled PWM signals which are connected to the IGBT modules in the converter. A 2.2 kW two pole asynchronous motor was used, which was not connected to any external load. The line currents and the motor voltage are measured and used by the controller and the combined speed/stator flux estimator respectively. The drive was tested by providing either one or both channels of a stereo input amplifier to the drive. As predicted by the simulation, the torque and/or flux ripple fol-

lowed the musical torque and/or flux reference up to high input frequencies, which is possible using a switching frequency in the modulator of almost 20 kHz. This ripple induces vibrations in the motor structure with the frequency of the music and the machine behaves as a loudspeaker. If the motor is placed on a surface the vibration from the motor structure will be transferred to that surface and further sound amplification will be obtained. Interesting is also to compare the different music quality that was obtained from different surfaces, being the most suitable a wooden box, which best resembles the commercial loudspeakers. When only the torque was modulated, a listener could perceive more low frequency components in the music emitted, whereas the high frequency passages were more accentuated when pure flux modulation was used. As a consequence, the music quality as perceived by the listener was found to be at its 'best' when both flux and torque inputs were used simultaneously. An indication of the audio sound capabilities from this setup was achieved by measuring the 'A' weighted sound power over the audio frequency range. In this case only the audio input mus_r (which modulates the torque reference) was connected to a sinusoidal voltage source whereby the frequency was varied from 200 Hz to 10 kHz. The obtained results, measured in a reverberating room, are shown in Figure 2.14. Included in this figure, by way of reference, is a loudspeaker transfer function. These results indicate that the drive sound levels at opposing ends of the frequency band are lower than those obtained from the loudspeaker. The low frequency sound level fall off is caused by the radiation efficiency of the motor, i.e. the sound radiation efficiency is reduced at lower frequencies (Wang et al., 2000). The high frequency fall off is due to the bandwidth of the current control loop. For a fixed PWM frequency, the number of carrier wave pulses in each period decreases for an increasing frequency of the reference signal and the resolution is then affected by this factor. Also, readily apparent from Figure 2.14 are two motor resonance peaks found near the frequencies 1.3 kHz and 2.7 kHz.

2.8 Summary

Vector control provides faster transient response compared to conventional v/f drives, and this is achieved by an efficient decoupling of the currents controlling the flux and the torque in the machine. These currents are easily controlled since they are regarded as d.c. components from a rotating coordinate system linked to the stator flux vector. The controllers for the direct and the quadrature cur-

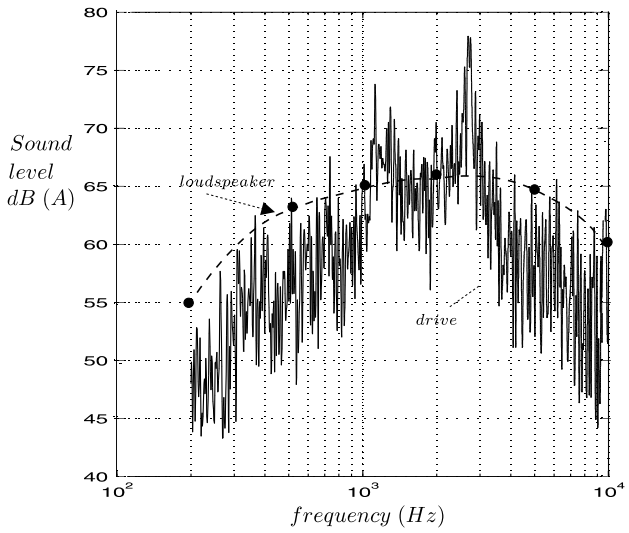

Figure 2.14: Measured sound power, $mus_l = 0$ of the 'musical' drive.

rents have been deduced, where the flux and the speed of the synchronous frame need to be estimated. A simulation program including the control system and simplified models for the power electronics, motor and observers has been presented. The control system has been implemented in a DSP card, which in turn is connected to a PWM card where the switching frequency was set to 20 kHz. The performance of the drive was tested by modulating music signals as noise references added to the direct and the quadrature currents. The motor structure resembled the behaviour of the core of a loudspeaker, reproducing efficiently the noise signals. The musical motor application served to demonstrate the capabilities of vector controlled drives implemented in advanced digital systems, leading to a suitable tool for acoustic research in electrical machines (Martínez Muñoz et al., 1999). This tool will be used in this thesis to analyze more in detail the acoustic radiation from a similar motor using different combinations of direct and quadrature current excitation at key frequencies, so as to ascertain the mechanisms of noise production in electrical machines.

Chapter 3

Analytical force computation

In this chapter an analytical expression will be deduced for the estimation of the radial air gap magnetic force in the motor used in the experiments. The procedure, which is based in the one presented by Bakhuizen (1973), is extended from a one-phase winding to a three-phase winding distribution, and the slotting effects are also taken into account. The results will serve to check the FEM calculations, which will be used for the noise prediction presented in Chapter 4.

The motor used in the experiments is a 2.2 kW, three phase, four pole induction machine, with 36 and 44 stator and rotor slots respectively. The effective no load and load currents are 2.24 A and 4.6 A, producing a torque of 15 Nm at full load. The conductors are distributed in the slots forming a combined single and double layer winding as shown in figure 3.1. Each slot contains the side of either one short pitched coil with 88 conductors or two fully pitched coils with 44 conductors each. Thus, the number of conductors in each slot is constant and equal to 88, although each one of the two 44-conductor coils sharing the same slot contributes to the flux in a different pole. Figure 3.2 shows the distribution of one phase along a quarter of the stator. Each one of the three-slot groups has a winding distribution as shown in Figure 3.1.

3.1 One phase winding distribution

In order to obtain an analytical expression for the radial airgap flux density, as a function of time and space, it is enough to develop the Fourier analysis of the applied MMF in one quarter of the machine since there are four poles. For the sake of convenience a reference magnetic coordinate system is defined with its

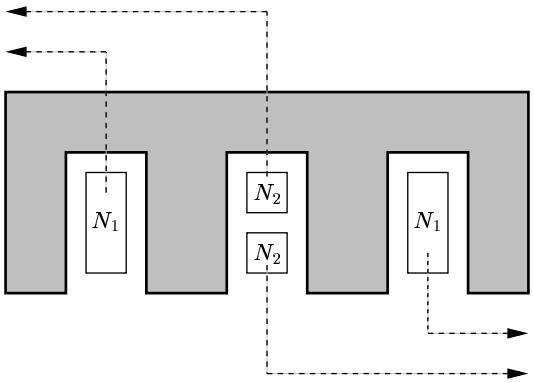

Figure 3.1: Winding distribution in the slots.

horizontal axis coinciding with the line of maximum airgap MMF, at an angle ζ with the horizontal axis of the machine as shown in Figure 3.2. The 10 degrees angle between two slots will be referred as ξ and the applied MMF in each slot will be considered to be evenly distributed along an angle 2ϵ. The absolute value of the infinitesimal applied MMF along one slot will be defined as $\frac{N \cdot i_a}{2\epsilon}$, and the total contribution of one slot to the airgap MMF will be $N \cdot i_a$, where N is the total number of conductors in one slot. With this nomenclature the applied MMF, which will be referred as $F_a(\alpha)$, can be expressed as follows:

$$-\frac{N \cdot i_a}{2\epsilon} \qquad -\zeta - \xi - \epsilon < \alpha < -\zeta - \xi + \epsilon \tag{3.1}$$

$$-\frac{N \cdot i_a}{2\epsilon} \qquad -\zeta - \epsilon < \alpha < -\zeta + \epsilon \tag{3.2}$$

$$-\frac{N \cdot i_a}{2\epsilon} \qquad -\zeta + \xi - \epsilon < \alpha < -\zeta + \xi + \epsilon \tag{3.3}$$

$$\frac{N \cdot i_a}{2\epsilon} \qquad \zeta - \xi - \epsilon < \alpha < \zeta - \xi + \epsilon \tag{3.4}$$

$$\frac{N \cdot i_a}{2\epsilon} \qquad \zeta - \epsilon < \alpha < \zeta + \epsilon \tag{3.5}$$

$$\frac{N \cdot i_a}{2\epsilon} \qquad \zeta + \xi - \epsilon < \alpha < \zeta + \xi + \epsilon \tag{3.6}$$

$$0 \qquad elsewhere \tag{3.7}$$

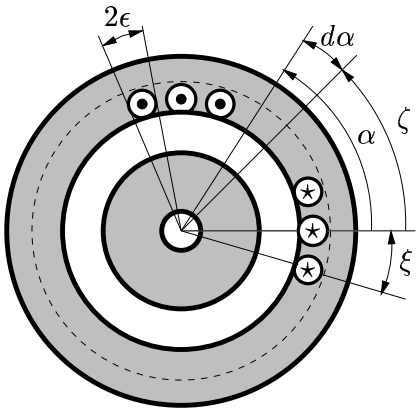

Figure 3.2: One phase winding distribution along one quarter of the machine

In order to examine the harmonic components in the airgap MMF, it is useful to develop the Fourier analysis of equations 3.1 to 3.7, defining F_a as follows:

$$F_a(\alpha) = \sum_{\nu=-\infty}^{\nu=\infty} C_\nu \cdot e^{-jp\nu\alpha} \tag{3.8}$$

where p is the number of pole pairs and ν is the number of the harmonic. From this equation, and for p=2, C_ν is defined as:

$$C_\nu = \frac{1}{\pi} \int_{-\frac{\pi}{2}}^{\frac{\pi}{2}} F_a(\alpha) \cdot e^{j2\nu\alpha} d\alpha \tag{3.9}$$

Combining equations 3.1 and 3.9, and after some mathematical transformations, the following expression is obtained for C_ν:

$$C_\nu = \frac{N \cdot \vec{i_a}}{\pi} 2j \frac{\sin(2\nu\epsilon)}{2\nu\epsilon} [\sin(2\nu(\zeta+\xi)) + \sin(2\nu(\zeta-\xi)) + \\ + \sin(2\nu\zeta)] \tag{3.10}$$

A so called slot factor $f_{g,2\nu}$ is introduced, which is defined as:

$$f_{g,2\nu} = \frac{\sin(2\nu\epsilon)}{2\nu\epsilon} \tag{3.11}$$

This factor can be approximated to one, considering the small slot opening and a reasonable number of ν harmonics. A closer look to equation 3.10 shows that the number of slots is multiplied by a factor of three if a concentrated winding is considered, i.e. if ξ is zero. This is reasonable since the winding is distributed in three slots with N conductors each. If the winding was concentrated in one slot instead, the number of conductors would be three times bigger.

The relation between the applied and airgap MMF can be deduced applying Ampere's law to an infinitesimal sector of the machine enclosing a certain applied MMF, as shown in Figure 3.3.

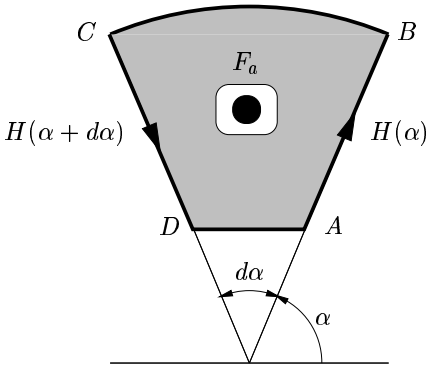

Figure 3.3: Infinitesimal sector of the machine.

The sign of the MMF has been selected to be positive in the outward direction. Considering that the applied MMF is evenly distributed within the sector, Ampere's law can be expressed as:

$$\oint H\,dl = F_a(\alpha)d\alpha \tag{3.12}$$

Evaluation of the line integral along the path ABCD, and neglecting the tangential components, leads to the following expression for the radial magnetic field strength H across the airgap g:

$$[H(\alpha) - H(\alpha + d\alpha)] \cdot g = F_a(\alpha)d\alpha \tag{3.13}$$

The second term on the left hand side of this equation can be rewritten using the following first order Taylor expansion:

$$f(x) = f(a) + \frac{f'(a)}{1!}(x-a) + ... \tag{3.14}$$

where $f = H$, $a = \alpha$, and $x = \alpha + d\alpha$ in this case. With these modifications:

$$H(\alpha + d\alpha) = H(\alpha) + \frac{\partial H(\alpha)}{\partial \alpha} d\alpha \tag{3.15}$$

Combining this equation with 3.13 leads to the expression:

$$H(\alpha) = -\frac{1}{g} \int F_a(\alpha) d\alpha \tag{3.16}$$

where $H(\alpha) \cdot g$ corresponds to the airgap MMF, which will be referred as F_δ. Hence, the relation between the applied and the airgap MMF is the following:

$$F_\delta = -\int F_a(\alpha) d\alpha \tag{3.17}$$

Introducing equation 3.8 in 3.17, the following expression is obtained for a four pole machine.

$$F_\delta = -\sum_{\nu=-\infty}^{\nu=\infty} \int C_\nu \cdot e^{-j2\nu\alpha} d\alpha \tag{3.18}$$

Developing the integral:

$$F_\delta = \sum_{\nu=-\infty}^{\nu=\infty} \frac{1}{2j\nu} C_\nu \cdot e^{-j2\nu\alpha} \tag{3.19}$$

Taking the expression for C_ν from equation 3.10:

$$F_\delta = \sum_{\nu=-\infty}^{\nu=\infty} \frac{N \cdot \vec{i}_a}{\pi\nu} f_{g,2v} \cdot e^{-j2\nu\alpha} [\sin(2\nu(\zeta+\xi)) + \sin(2\nu(\zeta-\xi)) + \\ + \sin(2\nu\zeta)] \tag{3.20}$$

This expression is valid for one phase, where the current $\vec{i}_a$ is defined as:

$$\vec{i}_a = \hat{i} \cdot e^{j\omega t} \tag{3.21}$$

representing a current vector rotating with an angular frequency ω. For the case of a concentrated winding, i.e. ξ = 0, the sum of the three sine terms in equation 3.20 is reduced to $3 \cdot \sin(2\nu\zeta)$. The value of $\sin(2\nu\zeta)$ is equal to zero for all even harmonics. For a given pair of odd harmonics $\pm\nu$, the sum of $\sin(2\nu\zeta)$ will be equal to ± 2. Thus, the amplitude of the airgap MMF for the different harmonics is given by the expression:

$$\frac{2 \cdot N\hat{i}}{\pi}\frac{3}{|\nu|} \tag{3.22}$$

with $\{|\nu| = 1, 3, 5, 7, ...\}$. The direction of rotation will alternate between two adjacent odd harmonics. Dividing equation 3.20 by the airgap length g and taking the real part yields the magnetic field strength H. Assuming infinite permeability in the iron, the airgap flux density B_δ is directly obtained multiplying H by μ_0. Figure 3.4 shows B_δ over one half of the motor when a current with an amplitude of 1.82 A (which corresponds to the no load phase current in the real motor) and a frequency of 50 Hz is used.

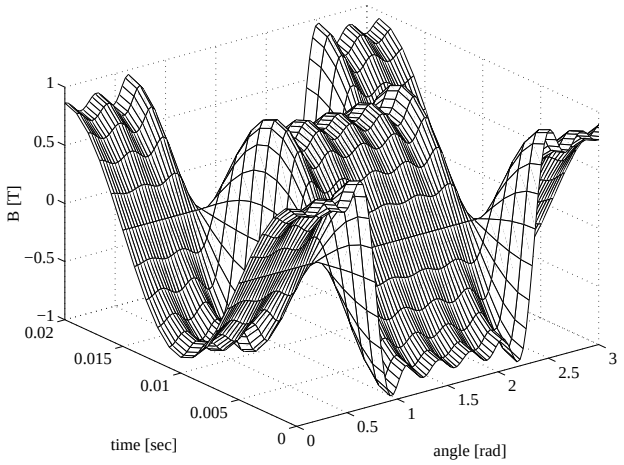

Figure 3.4: One phase concentrated winding.

In the case of the distributed winding, it can be shown that the sine terms inside the brackets in equation 3.20 still add zero for all even harmonics, leading

to the following expression for the amplitude of the airgap MMF:

$$\frac{2 \cdot N\hat{i}}{\pi} \frac{\sin(2\nu(\zeta + \xi)) + \sin(2\nu(\zeta - \xi)) + \sin(2\nu\zeta)}{|\nu|} \tag{3.23}$$

For the odd harmonics, the sum of the sine terms decreases and increases periodically for $\{|\nu| = 1, 3, 5, 7, 9, 11, ...\}$, but the contribution of higher order harmonics is little since $|\nu|$ in the denominator increases a well. This is also true for the concentrated winding, but there the factor introduced from the sine term is constant and equal to 3, whereas in the distributed winding it decreases for the first 9 odd harmonics. Hence, the influence of these harmonics in the distributed winding is less compared to the concentrated winding, as can be appreciated in Figure 3.5. The amplitude of the fundamental airgap MMF decreases when the winding is distributed, although the difference is rather small. For the winding distribution in the test motor, the sine terms in equation 3.23 add 2.968 for $|\nu| = 1$, which represents a negligible decrease of 1.07 % with respect to the concentrated winding.

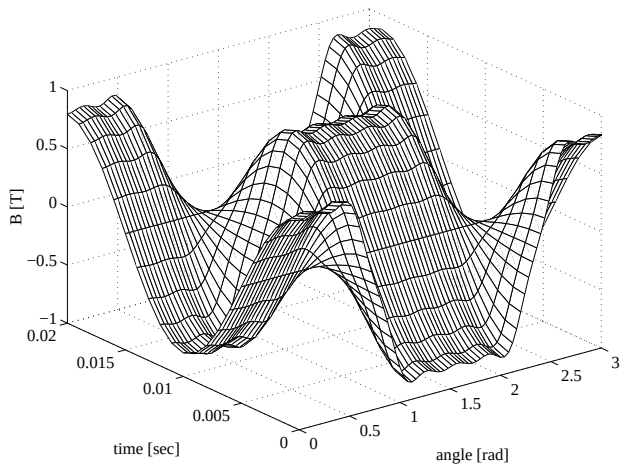

Figure 3.5: One phase distributed winding.

3.2 Three phase winding distribution

The airgap MMF for one phase can easily be extended for the case of a three phase machine where the current vector has the following form:

$$\vec{i}_{a,b,c} = \hat{i}\left(1 + e^{j\nu\frac{2\pi}{3}} \cdot e^{-j\frac{2\pi}{3}} + e^{j\nu\frac{4\pi}{3}} \cdot e^{-j\frac{4\pi}{3}}\right) e^{j\omega t} \tag{3.24}$$

In one hand, this expression takes into account the electrical phase difference between the currents from the three phases. This phase difference will be 120 degrees for the fundamental, and a multiple of this number for the corresponding harmonics. On the other hand it considers also the fact that the coils are shifted in space around the stator of the motor by an angle of 120 degrees. Introducing this three phase current in equation 3.20 and taking the real part, the total airgap MMF in the machine can be written as:

$$\begin{aligned} F_\delta = \sum_{\nu=-\infty}^{\nu=\infty} \frac{N\hat{i}}{\pi\nu} f_{g,2\nu}(\sin(2\nu(\zeta+\xi)) + \sin(2\nu(\zeta-\xi)) + \sin(2\nu\zeta)) \\ (\cos(\omega t - 2\nu\alpha + \frac{2\pi}{3}(\nu-1)) + \cos(\omega t - 2\nu\alpha + \frac{4\pi}{3}(\nu-1)) + \\ + \cos(\omega t - 2\nu\alpha)) \end{aligned} \tag{3.25}$$

The effect of introducing three phases and distributing the winding around the motor results in a further decrease of the winding harmonics, as shown in Figure 3.6.

3.3 Modelling the slots

So far, a constant airgap g around the motor has been assumed, which should be modified by the Carter factor to take into consideration the higher reluctance in the slot openings. The following formula has been proposed for the calculation of the Carter factor, based in the slot dimensions (Lipo, 1996):

$$K_c = \frac{\tau_s}{\tau_s - \frac{b_0^2}{(5g+b_0)}} \tag{3.26}$$

where τ_s is the combined length of one slot and one tooth, and b_0 corresponds to the slot opening. In the test motor, the 10 degrees angle ξ between two slots, at an inner stator radius of 47.66 mm gives a length of 8.32 mm. For a slot

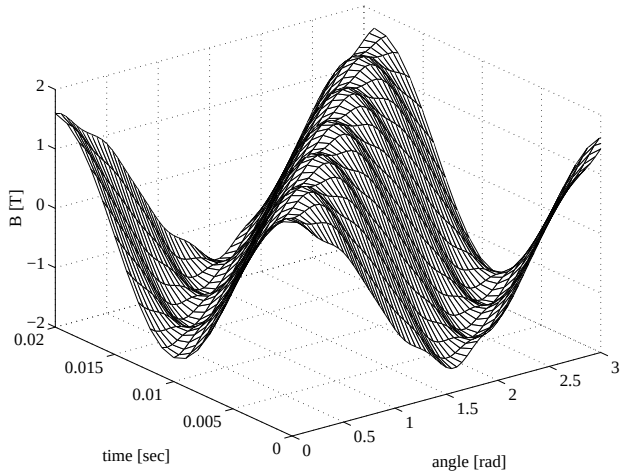

Figure 3.6: Three phase distributed winding.

opening of 2.54 mm and an airgap equal to 0.3 mm the Carter factor becomes 1.2375.

However, it is possible to calculate the slotting harmonics by considering the inverse airgap function between two slots, as shown in Figure 3.7. The value of h_e corresponds to the actual length of the path that the flux follows through the air along one slot opening before penetrating one of the adjacent stator teeth. This value has been estimated based on the work presented by Gerling (1994). A 'magnetically effective slot depth' h_e is defined to be equal to the geometrical slot depth h if the slot opening is greater or equal to double the geometrical slot depth. Otherwise $h_e = \frac{\pi \cdot b_0}{8}$, as it is the case in the test motor. For a geometrical slot depth of 20.085 mm, h_e becomes 0.997. Based on Figure 3.7, the inverse airgap function is expressed as:

$$\hat{g} \quad -\tfrac{\xi}{2} < \alpha < -\epsilon \tag{3.27}$$

$$\breve{g} \quad -\epsilon < \alpha < +\epsilon \tag{3.28}$$

$$\hat{g} \quad +\epsilon < \alpha < +\tfrac{\xi}{2} \tag{3.29}$$

Following the same procedure as for the applied MMF, a Fourier expansion

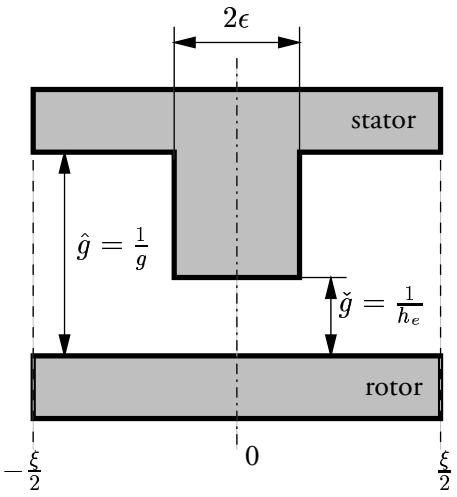

Figure 3.7: Inverse airgap function.

of equations 3.27 to 3.29 leads to:

$$q(\alpha) = \sum_{n=-\infty}^{n=\infty} C_n e^{-jnN_s\alpha} \tag{3.30}$$

where n is the number of the slot harmonic and N_s is the number of stator slots. From this expression C_n is defined as:

$$C_n = \frac{N_s}{2\pi} \int_{-\frac{\pi}{N_s}}^{\frac{\pi}{N_s}} g(\alpha) e^{jnN_s\alpha} \tag{3.31}$$

Developing the integral term a final expression for C_n is obtained:

$$C_n = \frac{N_s \cdot \epsilon}{\pi} \cdot \frac{\sin(n\epsilon N_s)}{n\epsilon N_s}(\check{g} - \hat{g}) + \hat{g}\frac{\sin(n\pi)}{n\pi} \tag{3.32}$$

where a new slotting factor appears, which can be approximated to one:

$$f_{g,n} = \frac{\sin(n\epsilon N_s)}{n\epsilon N_s} \tag{3.33}$$

Introducing equation 3.32 into 3.30 and taking the real part:

$$q(\alpha) = \sum_{n=-\infty}^{n=\infty} \left(\frac{N_s \cdot \epsilon}{\pi} f_{g,n}(\breve{g} - \hat{g}) + \hat{g} \frac{\sin(n\pi)}{n\pi} \right) \cos(nN_s\alpha) \qquad (3.34)$$

Finally, the radial magnetic field strength including slotting harmonics is obtained multiplying this expression by equation 3.25:

$$\begin{aligned} H(\alpha) = \sum_{\nu=-\infty}^{\nu=\infty} \sum_{n=-\infty}^{n=\infty} & \left(\frac{N_s \cdot \epsilon}{\pi} f_{g,n}(\breve{g} - \hat{g}) + \hat{g} \frac{\sin(n\pi)}{n\pi} \right) \cos(nN_s\alpha) \\ & \frac{N \cdot \hat{i}}{\pi\nu} f_{g,2\nu}(\sin(2\nu(\zeta + \xi)) + \sin(2\nu(\zeta - \xi)) + \sin(2\nu\zeta)) \\ & (\cos(\omega t - 2\nu\alpha + \frac{2\pi}{3}(\nu - 1)) + \cos(\omega t - 2\nu\alpha + \frac{4\pi}{3}(\nu - 1)) + \\ & + \cos(\omega t - 2\nu\alpha)) \end{aligned} \qquad (3.35)$$

The airgap flux density obtained when the slotting effects are included is shown in Figure 3.8.

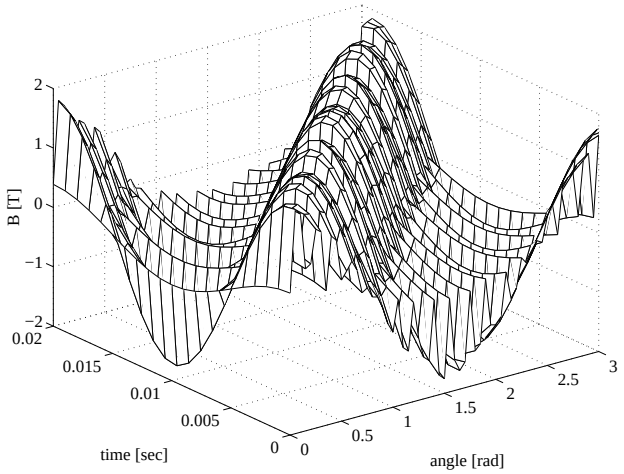

Figure 3.8: Three phase distributed winding with slots.

3.4 FEM validation

It is instructive to use the procedure presented in this chapter to compare the analytical solution to the one obtained digitally using the finite element method (FEM). The software used for the calculations is OPERA 2D. Figure 3.9 shows one quarter of the geometry, indicating the rotor, stator and surrounding air. The option of defining air around the stator was preferred rather than imposing the Dirichlet condition in the outer surface of the stator (vector potential equal to zero). Although the number of elements in the model increases, the fact that leakage flux can appear in the surface of the motor under very heavy saturation was taken into consideration. The thickness of the layer of air surrounding the stator was made equal to the radius of the motor.

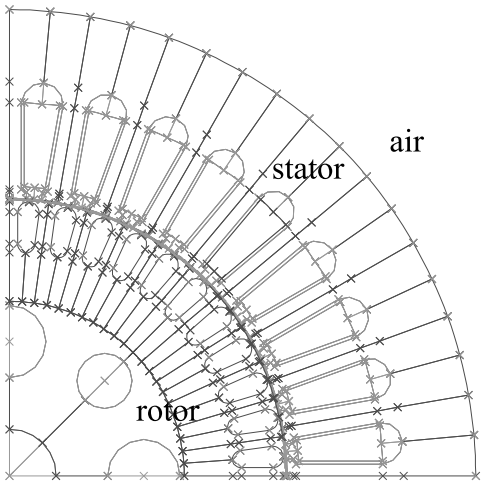

Figure 3.9: Wired plot of the geometry modelled in OPERA 2D.

Since this model will be also used for transient calculations, where the rotor mesh is rotated with respect to the stator, a new boundary condition needs to be imposed between the stationary and the rotating parts. This was achieved by defining a 'rotating airgap'. In order to obtain a very fine calculation of the airgap forces, five layers of elements were modelled in the airgap of the machine. Two of them were attached to the rotor mesh, other two to the stator

mesh and the rotating airgap was set in between. In this way, the number of elements in both sides of the boundary condition was optimized, and also it was ensured that the calculation of the forces could be done through the middle of the airgap without passing across any node, since the field there is multivalued. Defining the rotating airgap also had the advantage that the rest of the boundary conditions were set automatically so as to match both the magnetical and mesh properties in any of the solvers available. Figure 3.10 shows the element distribution in the area surrounding the airgap. The mesh was automatically generated using triangular elements, although it could be adapted defining the facets in a proper way and changing the number of subdivisions at the edges.

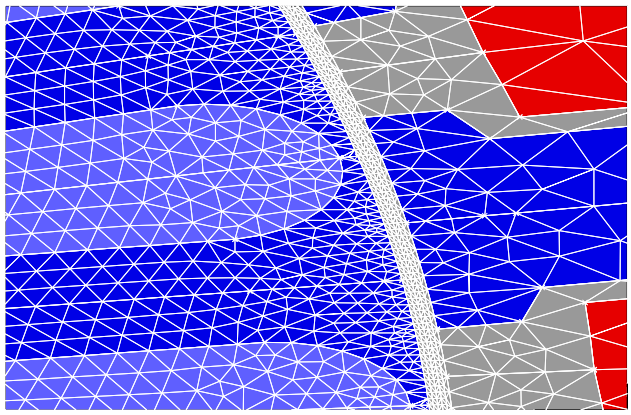

Figure 3.10: Mesh generated in the surroundings of the airgap.

The flux density distribution through the middle of the airgap was calculated performing a static solution at no load. Since the analytical solution assumes infinite permeability for the iron, a first calculation was undertaken defining a very high linear isotropic permeability for the iron. The results from both FEM and the analytical calculations are shown in Figure 3.11, where a similar behaviour can be observed. It should be remarked that the phases of the curves in this plot have been displaced in order to improve their visual inspection.

When the non linearities in the iron are considered in the FEM calculation, the airgap flux density drops to a more reasonable level around 1 T and its shape resembles a square wave, as shown in Figure 3.12. Besides, more irregularities

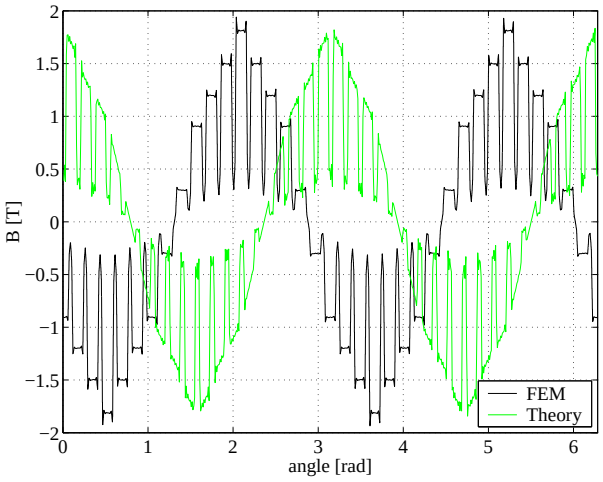

Figure 3.11: Comparison between analytical and FEM flux densities for ideal iron, phase displaced.

appear due to the saturation effects which are more predominant in the tip of the teeth. The radial stress in the laminated stator stack can be implemented applying Maxwell's stress equation for radial forces:

$$\sigma_r(\alpha) = \frac{B_\delta^2(\alpha)}{2\mu_0} \tag{3.36}$$

and the result from the analytical calculation is shown in Figure 3.13, where the slotting effects have not been included in order to make the picture more clear. The stress in the airgap of the machine was also calculated in FEM and the results when using non linear iron are presented in Figure 3.14.

3.5 Summary

An analytical expression has been deduced for the radial airgap forces in the test motor. The method is based in the Fourier analysis of the applied MMF. The expressions have been gradually developed from a one phase concentrated winding to the three phase distributed winding setup in the machine. The slotting effects have been incorporated in the model, developing the Fourier

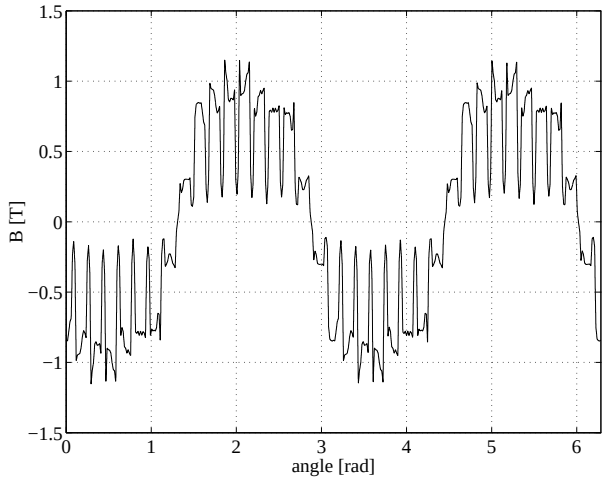

Figure 3.12: FEM solution considering non linear iron.

analysis of an inverse airgap function. Although the method assumes ideal iron, it is useful as a check of the results obtained from an ideal finite element model of the machine, and it could be appreciated that the results using both methods showed a good agreement.

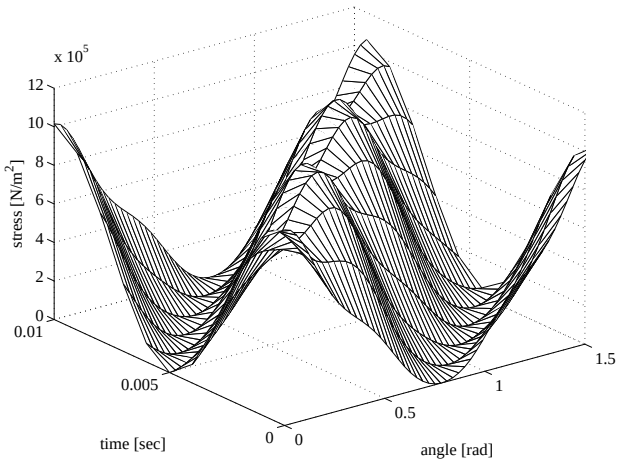

Figure 3.13: Analytical radial Maxwell stress, ideal iron.

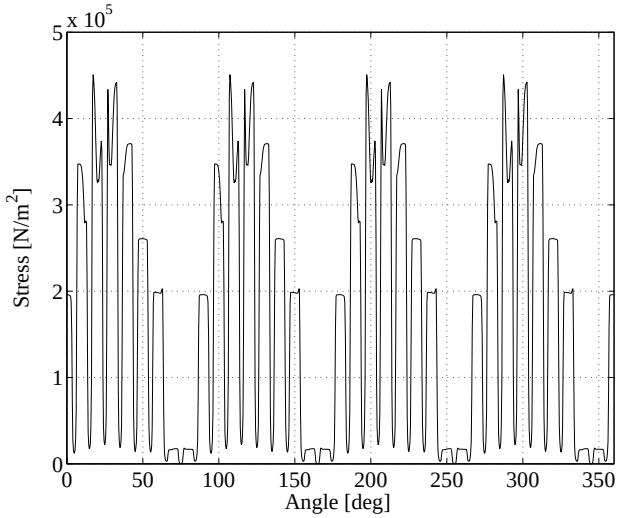

Figure 3.14: FEM Maxwell stress, non linear iron.

Chapter 4

Acoustic noise prediction

4.1 Introduction

The aim of this chapter is to study more in detail the mechanisms of acoustic noise production in vector controlled electrical machines, and establish a method for the prediction of the sound power radiation, based exclusively on the use of finite element modelling.

The analytical model presented in Chapter 3 introduced an understanding on how the linear airgap force distribution can be calculated based on the winding distribution in the machine. It served also to verify the results obtained from a finite element model of the machine, when the iron was considered to behave ideally. However, in order to perform an accurate calculation of the electromagnetic airgap forces, both the iron non linearities and the details of the motor geometry must be taken into consideration, and this can be achieved using finite element softwares (OPERA 2D/3D). The electromagnetic airgap forces are responsible for the vibration of the machine structure, which will radiate noise depending on its inherent mechanical properties. By performing a modal analysis (ANSYS), the properties of the structural modes of vibration can be calculated. The acoustic response of the motor to the excitation of these modes by the electromagnetic forces can be modelled in a third package (SYSNOISE) using the information provided by the other two electromagnetic and mechanical FEM softwares. This process is described schematically in Figure 4.1. The electromagnetic excitation force is imported into SYSNOISE from OPERA, and the modal information as well as the geometry are taken from ANSYS.

Both the mode shapes of a structure and the noise that it radiates when it is

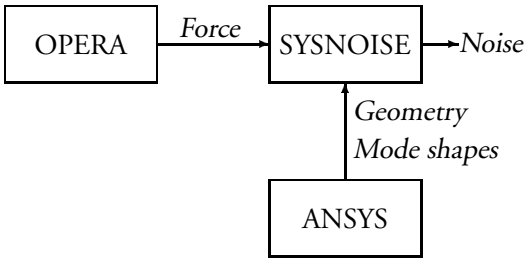

Figure 4.1: Finite element modelling process.

excited with a certain force can be measured experimentally. Hence, if the excitation force is a known quantity, the process shown in Figure 4.1 may be experimentally validated. The inconvenient with an electrical motor is that the airgap forces are very difficult to measure, but it is possible to get an estimation of them through finite element calculations. Instead, the process described in Figure 4.1 can be verified performing an experimental modal analysis of the structure, and measuring the acoustic response when a predefined excitation force is applied in a convenient location. However, for simplicity reasons, it is preferable to experiment with a smaller two-dimensional object, where the vibration pattern is easier to measure compared to the three-dimensional behaviour of the electrical machine. In order to ascertain the capabilities of the FEM simulation process explained above, the structural and acoustic analysis of a one axis symmetric aluminium plate was performed, and the details of the experiments and the results are presented in the appendices A and B. The natural frequencies of the plate as well as the shape of the modes of vibration are obtained from the *free response synthesis*, where the plate is excited by a random force and the vibration pattern at different points in the plate is analyzed. This procedure will be explained later in this chapter, and the details of the experimental set-up as well as the results obtained from the plate are presented in Appendix A. The acoustic behaviour of the plate is obtained from the *forced response synthesis*, where the plate is excited by a force with a fixed frequency, corresponding to one of the natural frequencies previously calculated, and the overall sound power radiated is measured. This procedure will also be explained in this chapter and the de-

tails about the experiment are included in Appendix B. The data obtained from the experiments is compared in each case with the results provided by the finite element method for verification.

The procedure aiming for a noise prediction in the electrical motor is similar to the one followed with the plate, but with the difference that the force applied to the inner surface of the stator will have to be estimated instead. However, the modes of vibration can be measured and simulated in ANSYS in the same manner, of course, with the increased difficulty of working with a three-dimensional structure. This work was performed by Wang (1998), and the procedure and results are summarized in Wang and Lai (1999).

The following sections describe the details of the different finite element models, and the calculations performed within the structural, electromagnetic and acoustic analyses involved in the process shown in Figure 4.1, as a basis for the experimental acoustic validation discussed in Chapter 5.

4.2 Structural modal analysis

One way of comparing the overall sound power level radiated by the motor when the flux or the torque are modulated is to add a reference noise signal to the direct or quadrature current respectively, while the other noise input is set to zero. The noise signal can be a sine wave of a frequency coinciding with one of the natural frequencies of the stator-casing combination, which is the path leading the vibrations responsible for the external sound radiation. The selection of a natural frequency for the excitation force amplifies the acoustic response, and hence the importance of determining them. This is achieved through the free response synthesis and both the experimental and FEM procedures used for their calculation are presented in this section.

Experimental free response synthesis

Resonance occurs when the dynamic forces in a process excite the natural frequencies in the structure, and a suitable way to identify them is to analyze the frequency response function (FRF) of the system. This is for efficient examination drawn as a plot of the ratio between the output vibration (X) and the input force (F) spectrums over a defined frequency range (ω).

$$H(\omega) = \frac{X(\omega)}{F(\omega)} \tag{4.1}$$

Vibration can be measured as displacement, velocity or acceleration of the particles in the structure and the FRF will be called *receptance, mobility* and *inertance* respectively. A resonance is represented in the FRF plot of the system as a peak. However, not all the peaks encountered must be related to a resonance, actually some of them may only be present in the input force exciting the structure. Since this excitation force is usually difficult to measure in most industrial processes, the identification of the natural frequencies of a structure is better done in the laboratory, where the applied force can be selected conveniently. Modal analysis is a common tool used in the laboratory not only to identify the natural frequencies but also the way the structure vibrates at those frequencies -mode shapes- as well as the rate at which the vibrations decay -modal damping. These two components, together with the modal frequency, constitute the 'modal parameters' of a structure and they fully characterize the vibration of single degree of freedom (SDOF) models. In fact, each resonance peak can be considered as the response of a SDOF system. Since a FRF consists of a collection of resonance peaks, thus the importance of understanding how these systems can be modelled in the physical, time and frequency domains.

SDOF models

A SDOF model can be described as a combination of a point mass m, a massless linear spring k and a linear viscous damper c, and the constrain that it can move in only one direction (x) is assumed. The mathematical model in the time domain when a force f is applied is easily obtained from Newton's second law:

$$m\ddot{x}(t) + c\dot{x}(t) + kx(t) = f(t) \tag{4.2}$$

An analytical model can also be developed in the frequency domain, where the behaviour of each component is expressed mathematically as a function of the frequency of the system: $\frac{1}{k}$ for the spring, $\frac{1}{j\omega c}$ for the damper and $\frac{1}{-\omega^2 m}$ for the mass (Ewins, 1984). At low frequencies the response of the system is dominated by the spring and it is in phase with the excitation. When the frequency increases, the inertial force of the mass becomes more important, until a point is reached where the mass and the spring terms cancel each other. At this frequency, called 'undamped natural frequency', the response is controlled only by the damping term and it lags the excitation by 90 degrees. If the frequency increases even further, the mass term takes control over the system and the response lags the excitation by 180 degrees.

The values of the mass, stiffness and damping used in the analytical model are usually unknown in the real structure. However there is an experimental way of modelling the vibration of a SDOF system, which indirectly leads to these parameters (Brüel & Kjær, 1988). The properties of the system are now defined in terms of the pole location p and the residue R, which are quantities that can be measured from the FRF plot of the system. The pole location consists of a real part equal to half the -3 dB bandwidth of the FRF peak and an imaginary part which is directly the modal frequency. The peak amplitude of the mode is also equal to $\left|\frac{R}{\sigma}\right|$, and this yields the value of the residue since the real part of the pole is the value of the damping σ. The modal frequency is defined as the damped natural frequency ω_d, and equation 4.3 shows how it is related to the undamped natural frequency ω_0. The stiffness η is also related to the natural and modal frequencies through equation 4.4, and the mass is linked to the value of the residue, as shown in equation 4.5.

$$\omega_0^2 = \omega_d^2 + \sigma^2 \tag{4.3}$$

$$\omega_d = \omega_0\sqrt{1-\eta} \tag{4.4}$$

$$R = -j\frac{1}{2m\omega_d} \tag{4.5}$$

Two of the modal parameters are contained in the pole location itself. The third one, the mode shape, is related to the residue. When a structure is excited with a force, each SDOF experiments a relative modal displacement. The residue of a particular mode is proportional to the product of the modal displacement at the response and excitation SDOF. The combination of the relative displacements of all the SDOF of the structure gives the mode shape, which is the same for a given frequency of the exciting force, independently of its magnitude.

In practice, the FRF is measured using a dual-channel analyzer, which in turn is connected to a computer where the data is stored for further post-processing. For each mode, the pole location and the residue need to be estimated from this data, but for each FRF measurement the analyzer provides around 800 complex values. With this enormous amount of data the use of a computer is essential, where advanced mathematical algorithms for the estimation are implemented. From the estimated parameters a new analytical FRF curve is obtained, which is superimposed on the measured data so that the operator can evaluate how they fit. This process is known as 'curve fitting'.

Curve fitting

The aim of curve fitting is to extract reliable modal data from the measurements. There are different types of curve fitting techniques that are used depending on the application, and they contain algorithms so as to reduce the effects of random noise in the measurements and the bias errors, such as any leakage or phase errors, which would cause erroneous parameter estimations. SDOF curve fitters can be used with lightly coupled modes, i.e. when the interaction between different modes is not important. Under these conditions a SDOF behaviour can be assumed around the modal frequencies. The user specifies a band around each mode containing the relevant data that will be used in the curve fitting process. The selection of the band is often a compromise between including as much data as possible and avoid moving far away from the resonance so that the effects of nearby modes makes the assumption of SDOF behaviour invalid. When the modes are heavily coupled, MDOF curve fitters are used instead. In this case, the operator specifies a region over which the curve fitter will seek the parameters and the number of modes contained in that region. The results using this technique depend to a large extent on the user's skill and experience in specifying the correct number of modes for the model. An example of a plot of the FRF function is presented in Figure 4.2, where the cursors define the band for one of the modes. The plot corresponds to one part of the FRF obtained from the experimental modal analysis done with the plate.

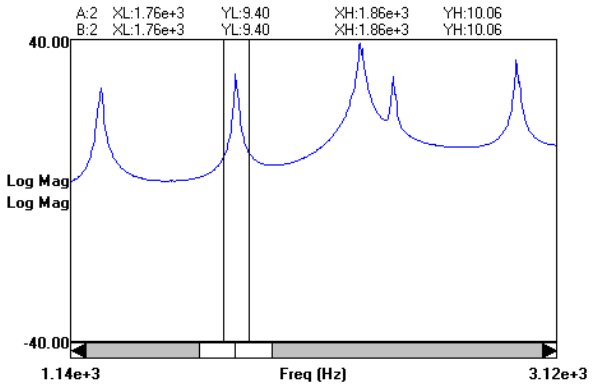

Figure 4.2: Frequency Response Function plot.

After the curve fitting process, each group of the resulting modal parameters is associated with the corresponding mode number. The different modes of vibration contain important information about the inherent dynamic properties of the free structure, i.e. when no forces are acting.

In order to get familiarized with the estimation of the modal parameters of a structure through the curve fitting process, the free response synthesis of the plate was performed. The practical details of the procedure described above, as well as the equipment used are included in the appendix. However, the modal analysis of the motor used for the experiments, see Figure 4.3, had already been performed by Wang and Lai (1999). It is necessary to describe this process though, since it will provide information about how the modal properties that will be used in future calculations have been determined.

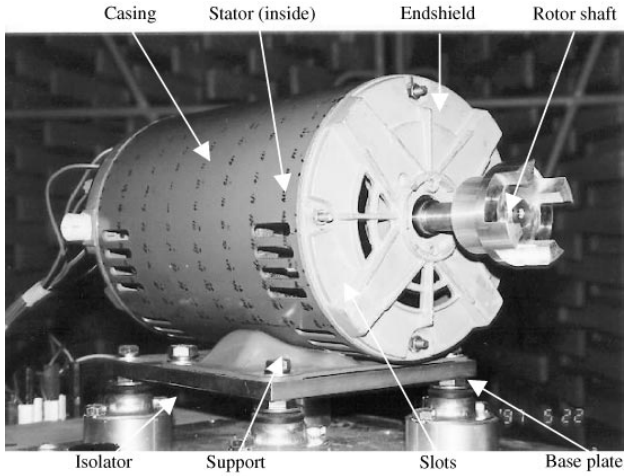

Figure 4.3: The test motor. Source (Wang and Lai, 1999).

The free vibration of the machine structure was achieved using two kinds of excitation: random excitation, provided from a shaker, and impact excitation, using a hammer with a steel tip but without extra mass. The frequency band for the analysis spanned from 0 to 3.2 kHz. The motor was tested resting on the test bench, through four isolators, and also without isolators, suspended together with the support and the base plate by soft rubber bands. In order to

examine the contribution to the overall vibration of the different parts of the motor, the response was measured with five different motor configurations: the whole motor structure; without the rotor; without isolators; without rotor and isolators; and finally, without rotor, isolators and end-shields. Only acceleration in the radial direction was measured and the modes of vibration were determined with reasonable accuracy, except perhaps those caused by the isolators.

In order to verify the modal results, the sound power spectra obtained from the machine when driven by three inverters under no load was also examined. It was observed that almost corresponding to each peak in the sound power spectra, a vibration mode was identified when the whole motor or the motor without the rotor was tested, indicating that the modal testing results obtained were reliable. The end-shields had also a great influence on the vibration of the motor, since they load the structure at the same time that they determine the boundary conditions of the motor casing. Besides, the modes determined without the rotor were similar to those with the rotor, implying that experimental modal testing or numerical modelling may be conducted without the rotor if low-frequency modes are not of interest.

FEM free response synthesis

Experimental modal tests should be combined with finite element analyses in order to compare the accuracy and reliability of the results. While FEM will provide all the modes of vibration, the less significant are likely to be missing in the experimental results. Nevertheless, all the measured modes should correspond to modes calculated with FEM. The experimental results obtained from the plate were verified using the modal analysis solver in ANSYS version 5.2, and the results are included in Appendix A.

Wang and Lai (1999) used the same solver to verify the experimental results obtained with the motor. In order to investigate the effects of the various substructures on the overall vibration behaviour, six motor models were developed taking into consideration the teeth of the stator, casing, slots on the casing, support and end-shields, as shown in Figure 4.4.

It is important to describe these models and the results obtained, in order to justify the selection of one of them for the acoustic calculations presented in this thesis, in the detriment of the other models.

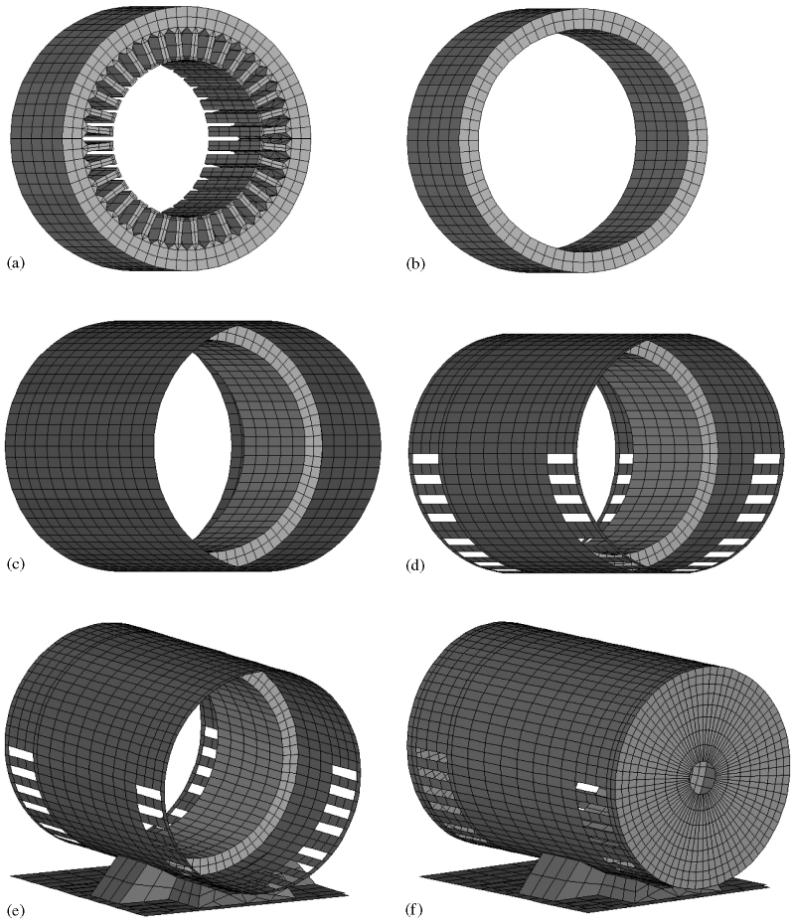

Figure 4.4: Finite element structural models: (a), the actual stator model; (b), a cylindrical shell stator model; (c), a two cylindrical shell model of the motor; (d), a two cylindrical shell model of the motor with slots on the outer casing; (e), a two cylindrical shell model of the motor with slots, the support and the base plate; (f), a two cylindrical shell model of the motor with slots, the support, the base plate and end-shields. Source (Wang and Lai, 1999).

The stator of the test motor is 0.092 m long and has 36 teeth. Each steel lamination has a density of 7800 kg/m^3, and the Young's modulus was determined to be 13.6 x 10^{10} N/m^2. The total masses of the stator and the windings are 6.6 and 2.88 kg respectively. The material of the stator was first assumed to be isotropic. The element types were Brick eight-node Solid45 and Tetrahedron Solid72 and the boundary conditions of the stator were set to be free at both ends. The effect of the winding was examined first. The windings were taken into account by treating them as an additional mass uniformly distributed in the stator, and this was done by changing the density of the material to 1193 kg/m^3 in model A. It was observed that the windings affect the natural frequencies of the stator very much. Hence, the mass of the windings must be taken into account in developing a structural model with reasonable accuracy.

The effect of the teeth was investigated next. For this purpose, the stator without teeth was considered, model B, which corresponds to the non-teeth region of model A. Both cases with and without windings were also investigated, again by changing the density of the iron material. It was observed that without windings the teeth had a strong influence on the calculated natural frequencies, with variations up to 18%. Also, the natural frequencies with teeth were lower than without teeth, which suggests that the mass of the teeth influences more the results, rather than their stiffness. When the winding was considered, the differences in frequency variations compared to model A were less than 10% in general. The reason for this behaviour is that the total mass of the stator and windings (9.48 kg) is much greater than that of the teeth (2.5 kg) and consequently, the vibration behaviour is dominated by the cylindrical shell, which in this case turns to be a good approximation of the stator structure when the windings are considered. However, it was indicated that such an approximation might not be valid for other stators, where the different number of teeth and dimensions could lead to a different vibration behaviour of the stator structure.

The effect of the casing coupled to the stator and the end-shields was analyzed as well. Previous studies cited in the paper concluded that its effect could be neglected. However, the different physical properties of the material used, as well as the different ratio between the length of the casing and the stator in the test motor, suggested that the effect of the casing might not be negligible in this case. A two cylindrical shell model, which included the mass of the windings in the stator, was developed as model C. The material was first defined as isotropic, but a closer study of the results suggested that the material in the stator should be orthotropic instead. The laminations are compressed in the axial direction

and, although the density of the material in the stator remains approximately the same, the stiffness of the stator in the axial direction would not be equal to the one of the stator made in solid material. As it is difficult to determine the pressure between the laminations, a typical value of Young's modulus in the axial direction was chosen, corresponding to 2% of the Young's modulus in the circumferential direction. The results obtained with this modification showed more agreement with the experimental results, proving essential to consider the material of the stator to be orthotropic. From the results, it could be observed that the vibration modes of the stator and the casing were influenced by the coupling between them. The modes of vibration of the casing were different to those without the coupling, as it would be expected since now the part of the casing attached to the stator is constrained while the rest of the casing is not. The effect of the coupling in the stator was to increase the natural frequencies in the low frequency range, corresponding also to an increase of the stiffness of the stator. At high frequencies the outer casing acts as a mass load to the stator, thus decreasing the natural frequencies. It was concluded therefore that the outer frame of the stator can play an important role in the vibration of small and medium-sized motors, where the mass of the frame is not negligible compared to that of the stator, and this effect would be further emphasized if the dimensions of the two structures are also quite different.

In order to further improve the calculated frequencies, the ventilation slots in the motor casing were included in model D. The reduction in the mass of the casing, and thus the load on the stator, increased the frequencies of the stator modes marginally, while the change in the stiffness of the casing decreased the frequency of its modes substantially, showing a better agreement with the experimental results.

The motor structure could be more accurate if the support and base plate are included, as shown in model E. The inclusion of these parts reduces the frequencies of the casing due to the increase of its effective mass. The effect of the stator teeth was again examined with this new model, and the results were within 5% compared to the model without teeth. Hence, the teeth of the stator can be neglected in the vibration analysis.

Finally, the end-shields made of aluminium by casting are incorporated in model F. Since their real geometry is rather complicated and the interest is not in their vibration itself but in their influence on the vibration of the casing, an equivalent end-shield with the form of a circular flat plate of the same mass, 0.36 kg, and a thickness of 6 mm was considered. The end-shields are coupled

to the casing by coupling the corresponding nodes in all degrees of freedom. From the analysis of the results, most of the vibration modes could be predicted, although the results show more discrepancy than the previous model. This is due to the complicated coupling between the end-shields and the casing, not all the points along the edges of the two structures are coupled and those who are, present different coupling strengths from each other. These details are too complex to consider in the model and nevertheless, the natural frequencies of all the modes identified in the calculations were within 10% of the experimental results, concluding that the model may be acceptable for acoustic prediction. Further studies showed that the details of the motor structure such as slots, support, base plate and end-shields affect the vibration behaviour of the motor very much, so they need to be modelled.

The geometry and modal results obtained from model F are the ones that will be introduced in SYSNOISE for the noise calculations in the next section, and their availability is acknowledged. It was important though to explain how this model was built, under which assumptions, and the relative influence that different parts of the motor have on the overall vibrations and noise emissions.

4.3 Electromagnetic analysis

The purpose of this section is to explain how the electromagnetic models were built and how the airgap forces were calculated and applied to the SYSNOISE model. A comparison between these results and the experiments would provide an idea of the accuracy of the noise prediction using FEM/BEM methods.

In order to establish a comparison between the sound emissions when the direct and/or the quadrature currents are modulated, a harmonic of the same amplitude and frequency is added to these currents separately. This can be achieved experimentally using the musical test drive presented in Chapter 2. The added harmonic would be the responsible for the noise emissions from the motor in each case, assuming that the mechanical and aerodynamic noise components are negligible, which can be achieved by rotating the rotor slowly. The harmonic added to the direct and quadrature currents had a frequency of 490 Hz and an amplitude of 0.25 A. This amplitude was symbolically referred as 'm' since in the experiments other amplitudes multiples of this value were also tested. The value of the direct current was reduced by 13% in order to avoid reaching over its nominal value when the noise current was added. The cases where this harmonic was added either to the direct or the quadrature current

under no load were simulated, as well as the case with no modulation at all. These cases will be referred as [d=m,q=0], [d=0,q=m] and [d=0,q=0] respectively. In the experiments, the machine was set to rotate at 70 r.p.m. and the corresponding currents were calculated in SIMULINK using the system presented in Chapter 2 (Figure 2.12). An example of the three phase currents for direct and quadrature modulation is presented in Figure 4.5.

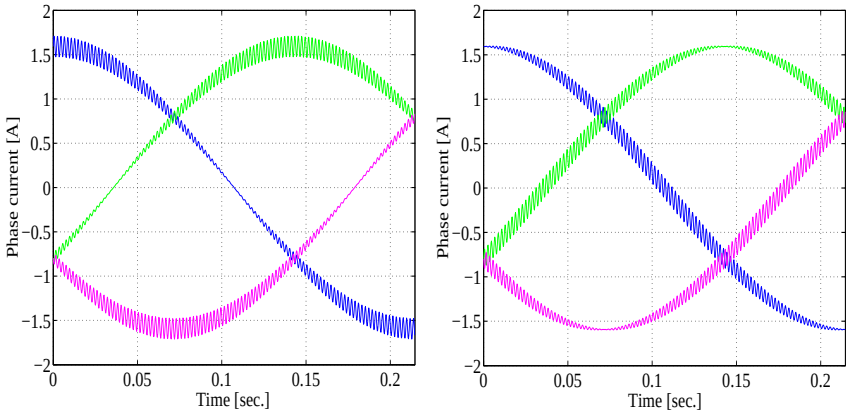

(a) Direct modulation currents (b) Quadrature modulation currents

Figure 4.5: Simulated phase currents for direct and quadrature modulation.

These currents were applied to the coils in the FEM electromagnetic model, where the airgap stresses were calculated. After some post-processing, the stresses were applied in SYSNOISE to the nodes located in the inner surface of the cylinder representing the core of the machine in model F, and the overall sound power was calculated. The information introduced in SYSNOISE for each one of these points is the Fourier transform of the force in the X and Y directions. This is achieved by storing the forces around the motor for a certain number of points in time, which thereafter will be transformed into the frequency domain with the help of the FFT function in MATLAB. For a rotational speed of 70 r.p.m. one cycle of the fundamental component of the current is completed every 0.4286 seconds, and it contains 210 noise cycles. In order to capture the effect of the added noise with a good resolution, the sampling time was

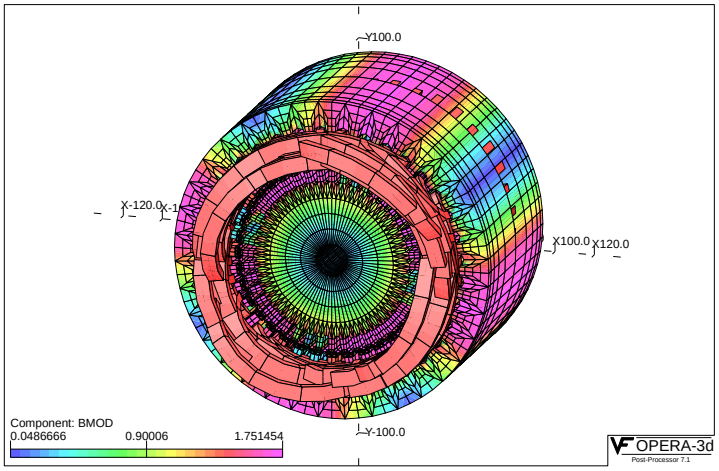

Figure 4.6: 3D FEM model of the test motor.

$2.2\text{x}10^{-4}$ seconds, which gave a ratio of 9.295 samples per noise cycle. Each sample corresponded to one simulation, so a total of 1952 simulations were performed for each case.

The 3D model

The software used for the 3D calculations was OPERA 3D, versions 7.1 and 7.5. Both in the 3D and 2D packages the currents in the rotor slots were induced when using the dynamic solvers.

The aim was to simulate the motor with a 3D model in order to take into consideration end winding effects, and also the influence of skewing in the rotor slots, which contributes to decrease the torque ripple and thus the noise emissions. This model is shown in Figure 4.6, where the modulus of the flux density is plotted under no load operation. The aluminium in the rotor was removed from the picture for simplicity reasons. Part of the conductors are visible on the surface of the stator along the extrusion direction, but this is only due to a display problem in the version of the software used (ver. 7.1). The number of nodes and elements was 44020 and 32352 respectively.

The solution presented in Figure 4.6 was obtained from a harmonic analysis, where no extra noise was added to the fundamental current. This could

be achieved using one of the transient solvers, where the rotor was locked, by defining two currents in the same coil: a d.c. component for the fundamental wave and an a.c. component for the noise, with a frequency equal to the noise frequency minus the slip frequency. However, the forces obtained using this procedure would correspond approximately to the forces observed from the rotor side, not from the stator as it was desired. There was the possibility of using another transient solver, where the rotor was rotated with a user-defined speed. In this case, the real frequency of the currents was defined in the stator coils. This was actually the option that would provide the required force, but the model could not be simulated since the simulations crashed due to convergence problems in the solver. Besides, although symmetry could be exploited in the extrusion direction, it was not possible to apply it along the circumferential direction, which increased dramatically the number of elements in the model and hence the computation time. These problems contributed to the transition towards the 2D software.

The 2D model

The software used for the 2D calculations was OPERA 2D, version 7.5. In order to check the model, a harmonic analysis was performed at full load. The number of elements in the model, specially in the airgap, the rotor slots and the surrounding regions, was increased until no change was appreciated in the amount of torque produced by the machine. The final torque was 10% higher than the rated value specified in the data sheets. The differences were mainly attributed to the fact that no inductance and resistance were included in the aluminium end-ring.

In order to simulate the cases that will be analyzed in SYSNOISE, the rotating machine transient analysis module was used. This is the equivalent to the 3D transient solver with the rotating rotor, but symmetry can be exploited in the circumferential direction, so it was sufficient to model one quarter of the machine. The currents calculated in SIMULINK were introduced as tables for the different coils. The fact that the maximum number of output cases was limited to 99 implied that 20 analyses had to be carried out in order to obtain the results at the 1952 points within one fundamental cycle. Each analysis was re-started from the last value in the previous one. Before starting to rotate the rotor, a static solution was performed, in order to reduce the starting transients. Actually, under no load, no significant transients were observed in the

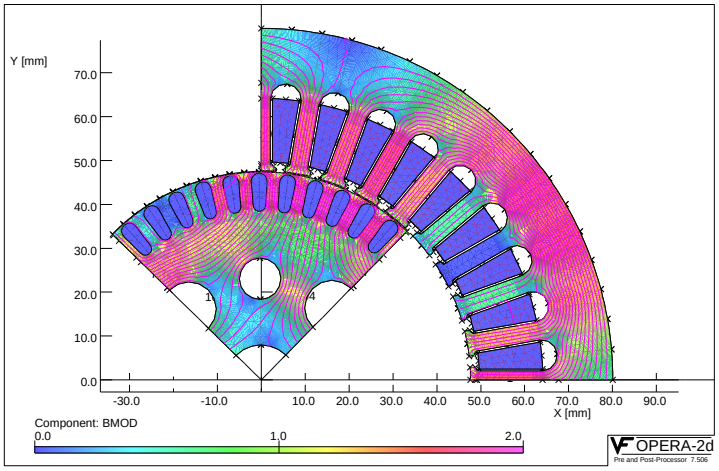

Figure 4.7: 2D FEM model of the test motor.

first fundamental cycle of the current. These results were compared up to the third cycle (one turn later, 1.2876 seconds), obtaining the same results. So it was concluded that the forces could be extracted already from the first fundamental cycle. A picture showing the flux density in the motor at one position is presented in Figure 4.7.

Force computation

The number of divisions in the acoustic model around the inner side of the cylinder representing the stator core is 72 in the circumferential direction and 5 in the longitudinal direction. The forces were applied at the nodes between the elements. The nature of the 2D force calculation implied that all the nodes along the extrusions in the 3D acoustic model were assigned the same force as their corresponding node in the first layer. The force applied at one node corresponds to the one that should be applied in the middle of the adjacent element. Since there is actually one more layer of nodes than of elements, the nodes around both edges of the cylinder were assigned half of the force that is applied at the inner nodes.

The forces were calculated in the electromagnetic model, by implementing equations 4.8 and 4.9 through the middle of the airgap. The values of h_x and

h_y correspond to the cartesian components of the airgap magnetomotive force, b_x and b_y are the flux densities and n_x and n_y are unit length vectors corresponding to the x and y components around the motor. The force densities, f_x and f_y, were transformed into force by multiplying with the area of an imaginary element at the airgap spanned through the same angle as one element in the back core of the acoustic model, and with the same length. In this way, the total force applied is maintained constant, although the force density in the back core is reduced since the area of the elements is increased.

$$h_n = h_x n_x + h_y n_y \tag{4.6}$$

$$h_m = b_x h_x + b_y h_y \tag{4.7}$$

$$f_x = b_x h_n - n_x \frac{h_m}{2} \tag{4.8}$$

$$f_y = b_y h_n - n_y \frac{h_m}{2} \tag{4.9}$$

There are several ways of integrating the force in the electromagnetic model. Since one extrusion in the acoustic model consists of 72 elements and there are 36 teeth around the stator, half of the elements could be assigned the force in the teeth, and the other half the one in the slots, alternating each other between adjacent elements. Since the width of the teeth and the slots is not the same, in practice part of the force in the sides of the teeth was also applied to the slot element. The integration performed in this way received the name of *odd function integration*. The other possibility is to do the integration of the forces around groups of half a tooth and half a slot, and vice-versa for the adjacent group, and it received the name of *even function integration*. An example of the forces calculated with both methods is presented in Figure 4.8. Since the odd function integration presented more similarities with the force distribution around the airgap of the real machine, it was selected for the simulations. However, it could be argued that the gradient of the forces in the back core between adjacent elements would be little and therefore the even function should be used instead.

The resolution for the integration of the forces was 13 points per element. The table of the forces for one layer of elements consisted of 1952 lines and 72 columns, corresponding to the time values and the element number respectively. These results were transformed into the frequency domain, and two tables were created for each one of the cartesian components of the forces that should be applied at each node in the acoustic model. Each table consisted of three columns,

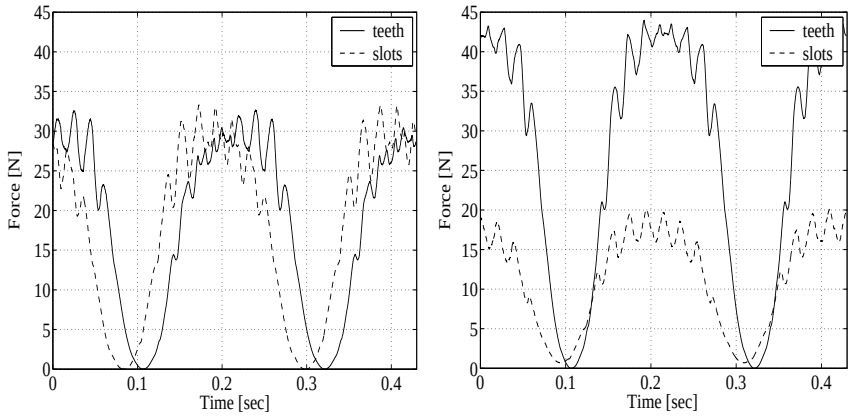

(a) Even integration.

(b) Odd integration.

Figure 4.8: Force at the teeth and slots for the even and odd integration functions.

the first one specifying the frequency and the second and the third ones specifying the real and imaginary components of the Fourier transform. In order to establish a comparison between the applied force for the different cases simulated, the spectrum of the total force was also computed. This was done by adding the absolute value of the spectrums at the 72 nodes around one layer of elements, implementing equation 4.13.

$$F_{nx} = \sqrt{\Re\left(f_{nx}\right)^2 + \Im\left(f_{nx}\right)^2} \tag{4.10}$$

$$F_{ny} = \sqrt{\Re\left(f_{ny}\right)^2 + \Im\left(f_{ny}\right)^2} \tag{4.11}$$

$$F_N = \sqrt{F_{nx}^2 + F_{ny}^2} \tag{4.12}$$

$$F_T = \sum_{N=1}^{72} F_N \tag{4.13}$$

In this way, the values of the total force were calculated when the machine rotated at 70 r.p.m. under no load. Figure 4.10 presents the results of the total force in one extrusion for no modulation ([d=0,q=0]), direct current modula-

tion ([d=m,q=0]) and quadrature current modulation ([d=0,q=m]) with a noise frequency of 490 Hz. In order to compare more easily the forces at the different cases, the narrow band results were transformed into 1/12 octave bands by linearly adding all the components within each band, and the results are presented in Figure 4.10(d).

BH curve sensitivity analysis

From Figure 4.7 it can be observed that a wide region in the back core, and also in the stator and the rotor teeth, are under saturation. The operation point of the machine is therefore located in the saturated part of the BH curve. Since the measurement of the properties of the iron in this part is not accurate, a sensitivity analysis of the BH curve was performed in order to determine how this factor influences the force distribution in the motor, and hence the accuracy in the prediction of the noise emissions. The values along the saturated part of the curve were increased by 10%, see Figure 4.9(a), and a new electromagnetic analysis was performed for the case [d=m,q=0]. The rate of change of the forces is presented in Figure 4.9(b), synthesized in 1/12 octave bands.

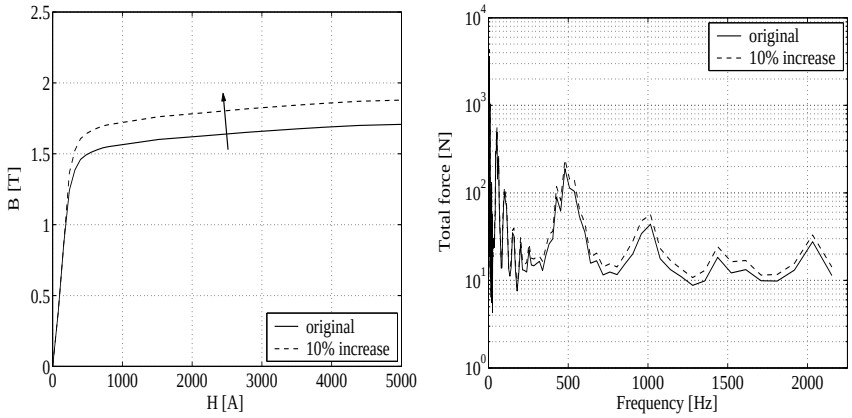

(a) BH curve increase.

(b) Force comparison for d=m,q=0.

Figure 4.9: Effect of a BH curve change in the forces for the case d=m,q=0.

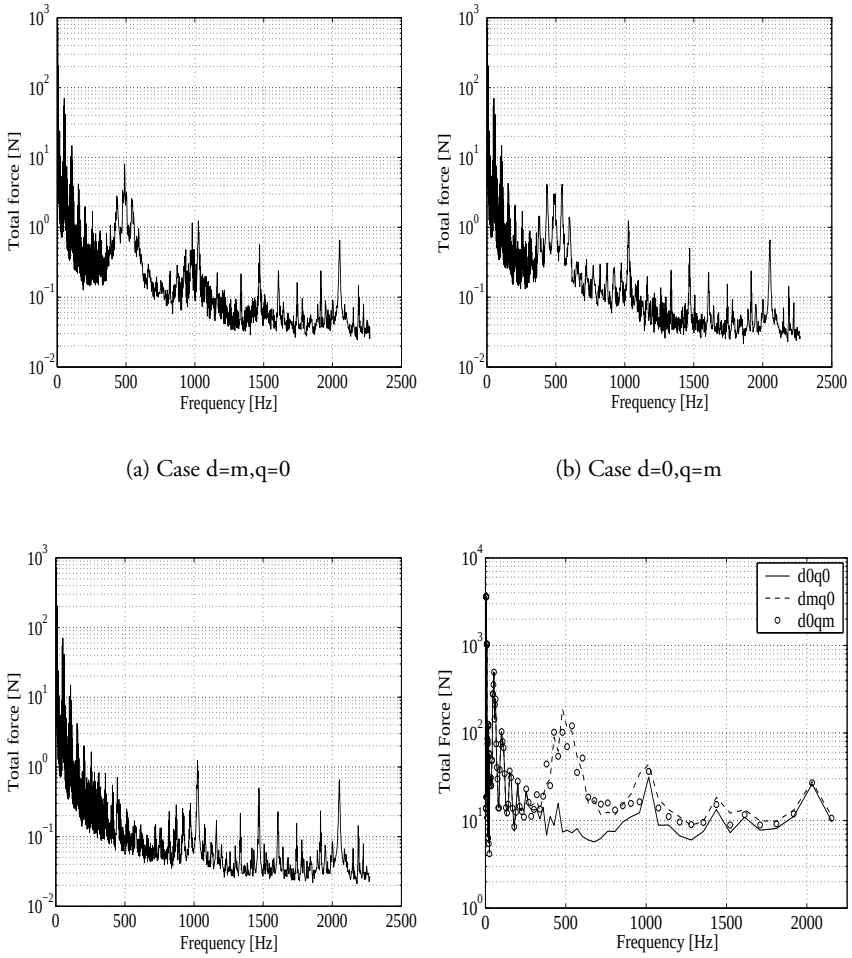

(a) Case d=m,q=0

(b) Case d=0,q=m

(c) Case d=0,q=0

(d) 1/12 octave band comparison.

Figure 4.10: Spectrum of the total force for the different simulation cases.

4.4 Acoustic analysis

The acoustic analysis was performed using SYSNOISE, version 5.3. The main advantage of using the boundary element method is that only the boundary of the problem domain needs to be discretized, i.e. there is no interior mesh. Although the mathematics involved in BEM are more difficult, the modelling effort is lower compared to FEM and it also presents the advantage of solving both interior (inside the defined model) and exterior (in the surrounding fluid) problems, with different possibilities of fluid-structure interaction.

For the acoustic calculations, both the surface mesh and the results file containing the modes of vibration of the structure were imported from ANSYS. All the modes were assigned the same damping factor, and two values were tested, 0.01 and 0.05. The tables of the forces calculated in OPERA were assigned to the corresponding nodes as boundary conditions in the cartesian coordinates. The simulations were performed for a frequency range between 80 Hz and 2250 Hz, in steps of 10 Hz. The sound power results at these frequencies were stored and converted into 1/3 octave bands since this was the format used in the measurements. A complete description of the measurements is presented in Chapter 5. However, the no load sound power results are included in this section as a reference for the validation of the simulations. A comparison between the different cases when a noise harmonic of 490 Hz is added to the currents at no load is presented in Figures 4.11(a), 4.11(b) and 4.11(c), when a damping of 0.01 is applied to the acoustic model. Another way of comparing the results is to plot the rate of change when one of the currents is modulated, with respect to the case when there is no modulation at all, both for the experiments and the simulations. These results are presented in Figures 4.11(d) and 4.11(e), and a comparison between the direct and the quadrature current modulation is shown in Figure 4.11(f).

In general, from these plots it can be observed that there is a lack of agreement below 400 Hz between the simulated and the experimental results, and this is due to the fact that the rotor was not included in the acoustic model (Wang and Lai, 1999). Also, for the case when no extra noise is added to the currents, the sound power level at the 1 kHz, 1.25 kHz and 2 kHz centre frequencies is considerably higher compared to the measurements. These levels are maintained when any of the currents is modulated. When the noise component is added to the direct current, the effect at the 500 Hz centre frequency is clearly visible, although the amplitude is in the order of 15 dB higher than

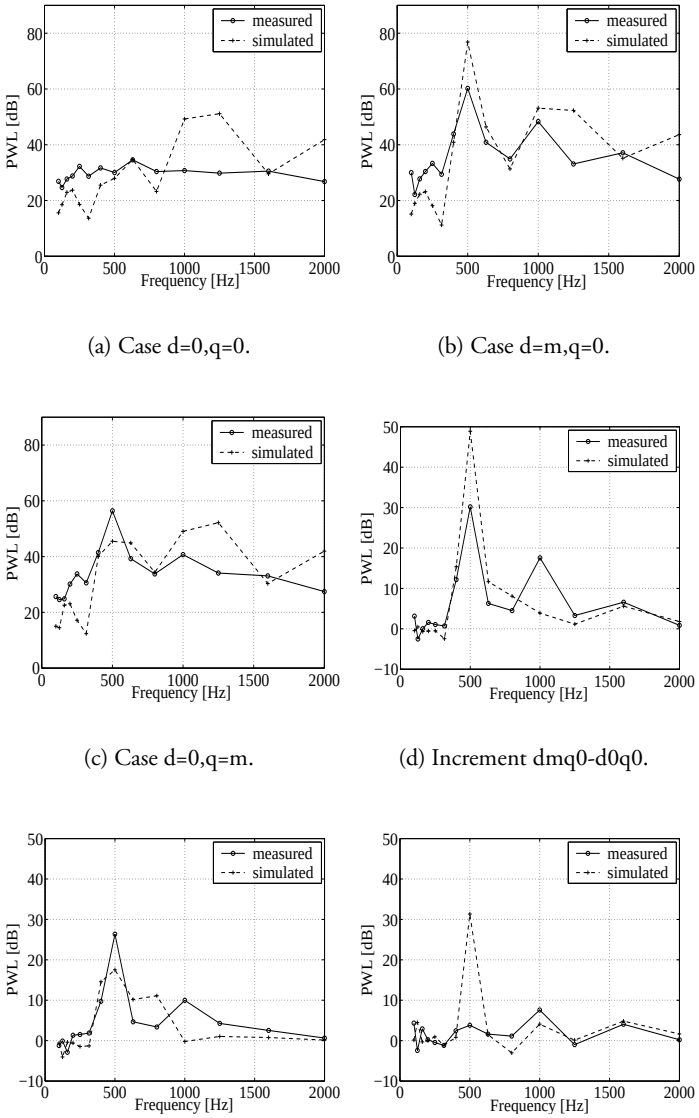

(a) Case d=0,q=0.

(b) Case d=m,q=0.

(c) Case d=0,q=m.

(d) Increment dmq0-d0q0.

(e) Increment d0qm-d0q0.

(f) Increment dmq0-d0qm.

Figure 4.11: Comparison of the acoustic results.

in the measurements. When the quadrature current is modulated instead, the response at 500 Hz is considerably decreased in the simulations. However, the rate of change at that frequency for the same cases in the experiments is around 4 dB.

From the incremental plots, it can be observed that the behaviour between 400 Hz and 1 kHz does not follow the same trend for the simulations and the experiments. However, at higher frequencies both the trends of the curves and their amplitudes are more similar. This seems to indicate that the acoustic model does not reproduce accurately the behaviour of the experimental motor below 1 kHz. The modes of vibration and the part of the motor they are associated with are presented in Table 4.1, both for the acoustic and the experimental model up to 2 kHz. It can be appreciated that below 1 kHz only three modes are calculated in ANSYS for the acoustic model, and all of them are associated with the seat. However, the experimental motor presents ten modes of vibration in the same frequency range, associated with the stator, rotor, casing and seat. Also, the mode close to the 490 Hz frequency of the noise harmonic is related to the seat instead of with the stator/casing as in the experiments. Hence, the response of the structure at this frequency would be expected to be considerably different compared to the measured one. Above 1 kHz, there is more agreement between the experimental and simulated results, not only in the frequencies but also in the part of the motor the modes are associated with. This actually supports the results presented in Figure 4.11, it explains the disagreement observed in the acoustic calculations below 1 kHz, and also the fact that the acoustic model and the experimental motor behave in a similar way at higher frequencies.

Although the trends of the curves and the increments are similar above 1 kHz, there is a considerable difference between the simulated and experimental results specially at the 1 kHz, 1.25 kHz and 2 kHz centre frequencies, even in the case when no noise harmonic is added to the currents. This seems to indicate that there is some problem in the force calculations. Actually, from Figure 4.10 it can be observed that the force spectrum seems to be stabilized at the same level above 1 kHz, instead of following a decaying trend, as it is expected for all physical systems. Besides, the fact that the skewing effects are not included in the 2D model influences the amplitude of the rotor harmonics, which might be considerably higher at these frequencies compared to the ones observed in the experimental motor.

The effect of the damping can also play an important role. Therefore, a change in the damping of the material was investigated, from 0.01 to 0.05, and

Experiment	*Simulation*	*Experiment*	*Simulation*
294 rotor		1105 stator	1123 stator
	375 seat	1240 seat	1097 seat
392 st/casing		1270 casing	
490 st/casing		1307 casing	
567 seat	485 seat	1393 seat	1353 seat
664 rotor		1480 seat	1559 seat
717 seat	695 seat		1535 casing
770 casing		1655 casing	1572 casing
816 casing		1743 stator	1682 stator
928 rotor		1795 stator	1933 stator
961 casing		1869 casing	1897 casing
1057 stator	1121 stator	1919 casing	

Table 4.1: Comparison between the simulated and the experimental modes.

the results are presented in Figure 4.12(a). It can be observed that a change in the damping affects in a different way the response obtained at different frequencies, specially above 500 Hz. The rate of change is in the order of 10 dB at 500 Hz, 800 Hz, 1250 Hz and 2000 Hz, whereas it is negligible at the rest of centre frequencies. Finally, a change in the properties of the material was considered, and the results obtained when the saturated part of the BH curve is increased by 10% is presented in Figure 4.12(b). It can be observed that the change in the sound power level is around 3 dB or less at different frequencies.

Finally, the sound pressure distribution in the motor and the surroundings obtained from SYSNOISE at 490 Hz is presented in Figure 4.13, for the case with no modulation. The results when the direct and the quadrature currents are modulated are presented in Figures 4.14 and 4.15 respectively. These plots actually confirm that at this frequency the vibration of the motor in the acoustic model is associated with the seat instead of with the stator, where no displacement is recorded on the surface of the casing. It should be noted that the scales used for these plots are different since otherwise the cases [d=0,q=0] and [d=0,q=m] can not be distinguished compared to the case [d=m,q=0]. The lower limit of the scales is 35 dB for all the plots, and the upper limit is 40 dB, 70 dB and 85 dB for the cases [d=0,q=0], [d=0,q=m] and [d=m,q=0] respectively.

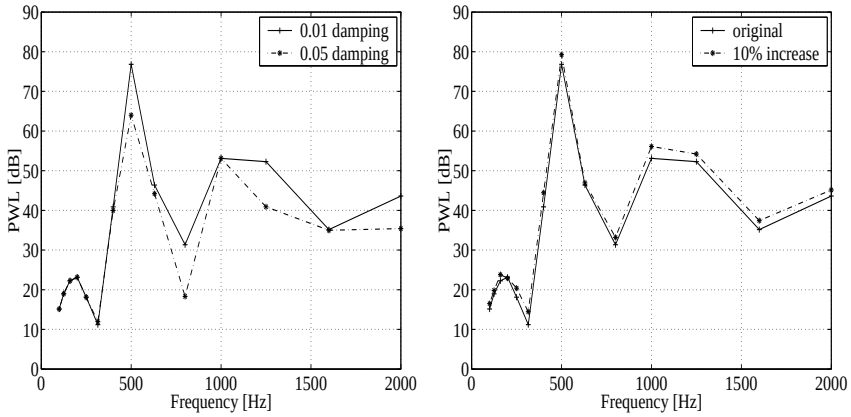

(a) Change in damping.

(b) Change in BH curve.

Figure 4.12: Effect of a change in the damping and in the BH curve for the case

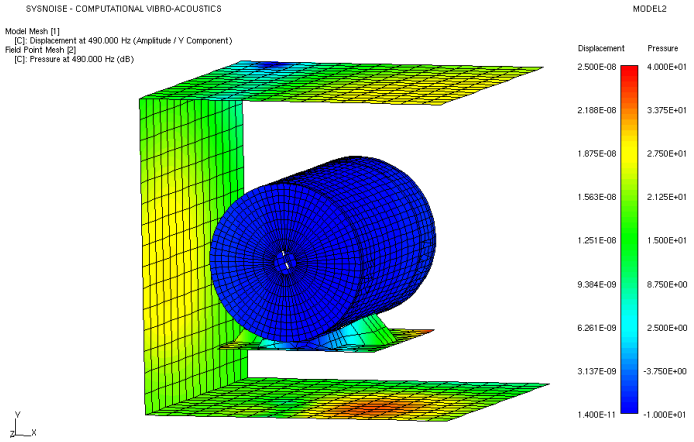

Figure 4.13: SPL distribution at 490 Hz, case d=0,q=0.

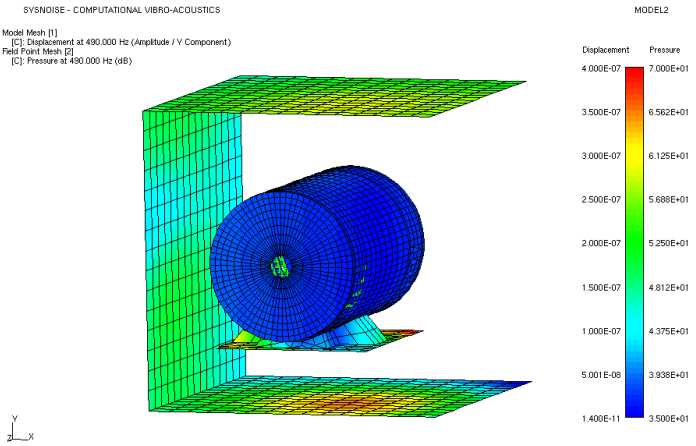

Figure 4.14: SPL distribution at 490 Hz, case d=0,q=m.

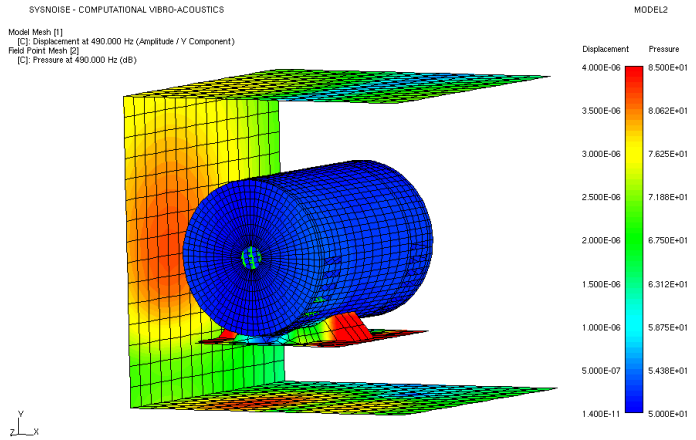

Figure 4.15: SPL distribution at 490 Hz, case d=m,q=0.

4.5 Summary and Discussion

In order to establish a method for the prediction of the sound radiation from an electrical motor, three different types of analysis need to be performed. First of all, a structural analysis provides information on how the structure vibrates at the different modal frequencies. The airgap forces exciting the structure are calculated through an electromagnetic analysis, and finally the results are combined in an acoustic analysis.

The structural analysis had already been performed and validated both experimentally and using FEM (Wang and Lai, 1999). Different studies showed that the teeth could be neglected when modelling the stator of the machine, since their contribution to the mass of the stator was more important than to its stiffness. Hence, an equivalent FEM model of the stator was developed removing the teeth and increasing the density in the stator core accordingly.

The electromagnetic analysis was performed using 2D software, due to the problems found in the available 3D package. This implied that the influence of skewing the rotor slots and the end-winding effects could not be modelled. The spectrum of the force up to 2250 Hz was calculated around the motor and integrated through the areas corresponding to the elements used in the acoustic model.

The results from the structural and electromagnetic analyses were imported into SYSNOISE, where the BEM was used for the acoustic analysis. Since the aim of the noise prediction is to be able to measure the noise radiation without building the motor, a general damping was assigned to all the modes of vibration. The fact that the rotor was not included in the model affected the results below 400 Hz. Actually, the behaviour of the acoustic model and the test motor were found to be quite different below 1 kHz. The number of modes of vibration predicted in ANSYS was considerably less, and also they were associated with different parts of the motor, specially at the 490 Hz frequency, which corresponded to the mode excited in the measurements. Therefore, there was little agreement between the simulated and the experimental results in this frequency range. However, the acoustic and the experimental models present a similar behaviour above 1 kHz, as could be observed from the modal results as well as from the noise prediction. The force calculation may also need to be trimmed. The force calculated presented a stationary level above 1 kHz, instead of decreasing as it is the case for all physical systems. This, added to the fact that the rotor harmonics at these frequencies were not damped by the skewing,

could explain why the levels of noise were considerably higher above 1 kHz in the simulations, when the currents were not modulated with extra noise.

Increasing five times the general damping applied to all the modes did not affect the response at different frequencies in the same way. Basically, some of them remained unchanged whereas others experimented a decrease of 10 dB. Hence, the damping should be selected carefully. A change in the material properties corresponding to a 10% increase in the saturated part of the BH curve was associated with a change of 3 dB or less in the acoustic simulations. Therefore, compared to the other factors discussed above, the change in the BH curve has a relatively low impact in the noise prediction.

Chapter 5

Measurements

5.1 Introduction

The purpose of the experiments was to compare the sound radiated when the direct and quadrature currents excited the structure with different amplitudes and frequencies, both under no load and load conditions. The modulation of the direct current will excite the stator structure with pure radial forces whereas the modulation of the quadrature current will contribute to the vibration both with radial and tangential forces. In this chapter the equipment used for the experiments as well as the results of the different tests will be presented and discussed. Before that, it is necessary to introduce the basic acoustic terminology and some background about sound measurement techniques, which will complete the understanding of the experimental work, post-processing and results.

5.2 Acoustic terminology

In acoustics it is important to distinguish between sound pressure and sound power. Sound power relates to the rate at which a sound source radiates energy, i.e. energy per unit time. A noise source radiating a certain amount of sound power will produce a change in the sound pressure depending on the surrounding environment. This concept can be better understood considering its analogy with a heater placed in a room. The heater radiates a certain amount of heat into the room (sound power), but the actual temperature (sound pressure) will depend on the dimensions of the room, materials, other heat sources... Sound pressure is therefore the physical quantity that is perceived by the ear. The unit

of pressure is Pascal (Pa), and 1 Pascal is equivalent to 1 N/m^2. The human ear is sensitive to a range of frequencies from 20 Hz to 20 kHz and a range of acoustic pressure from 20 μPa to 200 Pa. Owing to the wide range of pressure (10 million times) that causes the sensation of hearing, a logarithmic scale is used to express the sound pressure level (SPL, L_p) in decibels (dB). The SPL is defined by equation 5.1, where p is the root-mean-square sound pressure in Pa and p_0 is the reference sound pressure, which is 20 μPa for air.

$$L_p = 10 \log \left(\frac{p}{p_0} \right)^2 \tag{5.1}$$

In general, for noise due to a composite of sounds with different frequencies, the total sound pressure level is given by equation 5.2.

$$L_p = 10 \log \sum_{i=1}^{n} 10^{0.1 L_{pi}} \tag{5.2}$$

The amount of noise produced by a machine can not be necessarily quantified by measuring the sound pressure. The sound power has to be determined instead, which is a better descriptor of the noisiness of a sound source. The sound power level (PWL, L_W) of a source is defined in dB by equation 5.3, where W_0 is the reference power, which is 10^{-12} W for air.

$$L_W = 10 \log \frac{W}{W_0} \tag{5.3}$$

Related to the sound power is the concept of sound intensity, which is the sound power in watts per unit area in m^2, and is defined as the average rate of energy flow through a unit area normal to the direction of propagation, as given by equation 5.4, where $\vec{u}$ is the particle speed. The instantaneous sound intensity, $p\vec{u}$, is a vector quantity whose magnitude and direction at any point in space may vary with time. Note also that energy travelling back and forth does not contribute to the averaged intensity, and thus there will be some net intensity flow only if there is a net energy flow through the area considered.

$$\vec{I} = \frac{1}{T} \int_0^T p\vec{u} dt \tag{5.4}$$

The sound intensity level, L_I, of a source is defined in dB by equation 5.5, where I_0 is the reference intensity which is 10^{-12} W/m^2 for air.

$$L_I = 10 \log \frac{I}{I_0} \tag{5.5}$$

The sound pressure or sound intensity levels can be displayed and stored in a spectrum analyzer for further post-processing. Frequency analyzers may be based on either constant bandwidth or proportional bandwidth devices. The constant bandwidth device is basically a tunable narrow-band filter with constant bandwidth $\Delta f = f_u - f_l$, where f_l and f_u are the lower and upper half-power frequencies. The proportional bandwidth device consists of a series of relatively broadband filters such that the ratio f_u/f_l is constant. The centre frequency f_c of a proportional bandwidth filter is given by equation 5.6. The most common proportional bandwidth filters are in the form that satisfies that $f_u/f_l = 2^x$, where x=1 for octave band filters and x=1/3 for 1/3-octave band filters.

$$f_c = \sqrt{f_l f_u} \tag{5.6}$$

In order to reflect the response of the ear to different frequencies, a weighting function (known as A-weighting function) approximating an inverted 40-phon loudness contour is usually applied to the measured sound pressure level and the result is expressed as dB(A). There are other weighting functions, as shown in Figure 5.1. The B and C functions approximate the human response at loudness levels of 70 phon and 90 phon respectively while D is a standarized function for use in aircraft noise measurements. The A-weighting scale is the most widely used since it best approximates the human response. Below 1 kHz and over 6 kHz the A-scale is negative, representing a reduction in the sound level in order to compensate for the human ear sensitivity in the lower and higher frequency ranges.

5.3 Sound measurement techniques

Sound power can be related to sound pressure only under carefully controlled conditions, where special assumptions are made about the sound field (Lai, 2000). The 'free field' describes sound propagation in idealized free space where there are no reflections. These conditions are held in open air far from the

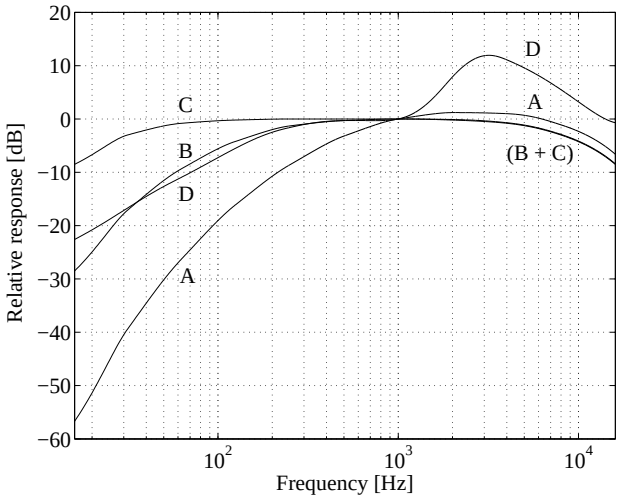

Figure 5.1: The frequency weighting functions.

ground or in an anechoic room, where all the sound striking the walls is absorbed. In a free field the intensity I is related to the root-mean-square pressure p by equation 5.7, where c is the speed of sound.

$$I = \frac{p^2}{\rho c} \tag{5.7}$$

Introducing this equation into 5.5 leads to equation 5.1, implying that in a free field the sound intensity level is equal to the sound pressure level. Hence, the sound power of a source can be determined by measuring the averaged sound pressure level over a hypothetical closed surface in an anechoic room, and is given by equation 5.8, where $\overline{L_p}$ is the averaged surface sound pressure level in dB and S is the area of the test surface in m^2.

$$L_W = \overline{L_p} + 10 \log S \tag{5.8}$$

In a 'diffuse field' sound is reflected so many times that it travels in all directions with equal magnitude and probability, and this field is approximated in a reverberant room. In a diffuse field, equation 5.9 gives the relation between

the intensity and the pressure.

$$I = \frac{p^2}{4\rho c} \tag{5.9}$$

The sound power level of a source can be determined by measuring the average sound pressure level inside a reverberation room. It can be calculated from equation 5.10, where T is the reverberation time of the room in seconds, V is the volume of the room in m^3, S is the total surface of the room in m^2 and λ is the wavelength at the centre frequency of the frequency band in meters.

$$L_W = Lp - 10\log T + 10\log V + 10\log\left(1 + \frac{S\lambda}{8V}\right) \tag{5.10}$$

Traditionally, the only way of measuring how much sound power a machine radiates was to place the machine in one of these rooms and measure the sound pressure, which is related to sound power depending on the nature of the room. However the sound power can also be calculated by means of sound intensity measurements, where the power level is measured directly in situ. Although this theory is old, it was not until the middle of the 1980's when the new technology made possible to develop devices for its practical application, and the interest about this technique increased dramatically.

Sound intensity measurement technique

The intensity at one point is expressed as the product of the pressure and the particle velocity at that point. This relation can be further developed and the expression linking the sound intensity and the sound power is deduced as shown in equation 5.11 (Brüel & Kjær, 1986).

$$I = p\vec{u} = \frac{Force}{Area} \cdot \frac{Distance}{Time} = \frac{Energy}{Area \cdot Time} = \frac{Power}{Area} \tag{5.11}$$

Sound intensity measurements are conducted placing the noise source of interest inside an enclosing surface. For simplicity, the enclosure is usually selected to be a rectangular frame, where the area of the different sides is calculated straightforward. The average intensity flowing through each surface is measured with a sound intensity probe, and the information is stored in a spectrum analyzer. Multiplying this intensity by the area of the surface gives directly the

power. The total sound power radiated by the source is calculated adding the contributions from all the surfaces.

The advantage of this technique is that the measurements can be performed in situ, even with steady background noise and in the near field of machines. The requirement is that no other noise source apart from the one subject to study must be located inside the enclosure. An external noise source will not produce any net contribution to the calculated intensity, since the energy will flow in and out of the enclosure and its overall effect will cancel when the power contributions of the different sides are added. It is important to note that this only holds if the external source is stationary, i.e. its noise does not vary in time, and if there is no absorption material within the box as otherwise some background noise will not flow out of the box again.

Sound pressure can be measured with a single microphone, but particle velocity is more complicated. The equation governing the motion of the fluid particles is the Navier-Stokes equation (Lai, 2000). Neglecting viscous effects and in the absence of mean flow and turbulence it can be expressed as in equation 5.12, where r represents the direction of the flow.

$$\rho \frac{\delta u_r}{\delta t} = -\frac{\delta p}{\delta r} \tag{5.12}$$

This equation can be further linearized and expressed as:

$$u_r = -\frac{1}{\rho \Delta r} \int (p_B - p_A) dt \tag{5.13}$$

Hence, the particle velocity can be determined by measuring the pressures p_A and p_B detected by two microphones closely spaced at a distance Δr, as shown in Figure 5.2. Sound pressure is a scalar quantity, i.e. it is the same whatever the angle of incidence. However, sound intensity is a vector quantity. When a two-microphone probe is used, only the component of the vector along one direction, the probe axis, is measured. The dashed circumferences in figure 5.2 show an approximation to the dipole behaviour of the sound intensity probe. For sound incident at 90^o from the axis there is no component along the probe's axis, as there will be no difference in the pressure signals from the two microphones. Hence, the reduction in the measured intensity will be infinite and there will be zero particle velocity and zero intensity. For sound incident at 0^o, there will be zero reduction and the probe will measure the correct value.

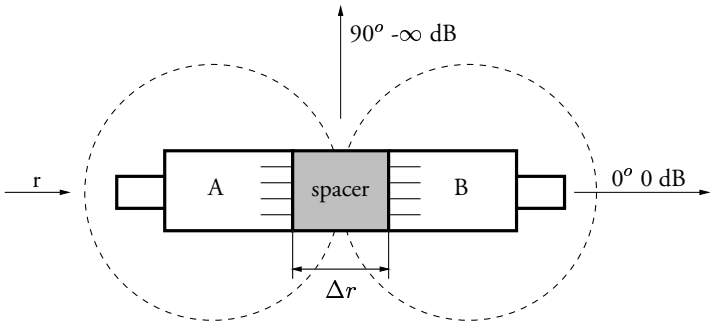

Figure 5.2: Sound intensity microphone and dipole characteristic.

For sound incident at any other arbitrary angle θ from the axis, the intensity component along the axis will be reduced by a factor of $\cos\theta$.

The choice of spacer depends on the frequency range to be covered, the higher the frequency the shorter the spacer should be for the linearization in equation 5.13 to hold. However, accuracy at low frequencies also depends on the spacer used. In all analyzing systems there will be a small time delay between the two channels which introduces a small phase change, influencing the results. This is a bias error called *phase mismatch error*. For a given probe and analyzer combination, this error can be estimated to be around $\pm$ 0.3^o (Brüel & Kjær, 1986). For an accuracy within 1 dB the phase change over the spacer distance should be more than five times the phase mismatch. In order to obtain a negligible high frequency error, the wavelength must be at least six times the spacer distance. Thus, for a given spacer the inherent phase mismatch of the equipment will cause a significant error in the measured intensity at low frequencies. Since no single spacer can cover a wide frequency range, the spacer should be selected depending on the frequencies of interest.

When the sound is incident at a certain angle from the probe's axis, the phase change that is detected is smaller since the effective spacer distance is reduced, and this will imply that the phase mismatch error will become more significant and the measurement range will be further reduced. One indicator of the accuracy of the measurement is the *reactivity index*, L_K, which is measured simply as the intensity level minus the pressure level during the measurement. By measuring the reactivity index the phase change across the spacer can be determined, and the influence of the phase mismatch in the accuracy of the

results can be calculated. In a general sound field, the phase change varies from point to point, but an average global value is often sufficient to give an idea of the accuracy. In an ideal free field, the difference between the sound pressure and sound intensity levels is zero. However, the phase mismatch causes a small difference between the two signals, as if there were some intensity along the spacer. Hence, apart from the errors introduced by the operator during the measurements, which are reported through the reactivity index, there is another source of error inherent to the equipment that can not be further reduced, and it is called the *residual intensity index*, L_{KO}. This index can be determined by using calibrating equipment to feed the same signal to the two microphones and measuring the difference between the sound level and the intensity level. The dynamic capability L_D of the sound intensity measuring system is defined in equation 5.14.

$$L_D = L_{K0} - K \tag{5.14}$$

The measured reactivity index should be below the dynamic capability for an acceptable accuracy in the measurements. For an accuracy within 1 dB, the constant K is equal to 7 dB, which corresponds to a phase change in degrees along the spacer distance of five times the phase mismatch.

5.4 Experimental set-up and instrumentation

The acoustic experiments were conducted in an anechoic room located in the School of Aerospace & Mechanical Engineering, University College, The University of New South Wales. The internal dimensions of the room are 3.5 m x 3.5 m x 3.5 m, and the cut-off frequency is 150 Hz. The motor was mounted in the centre of the room and rested on a test surface. In order to minimize the noise contribution from the load, a 10 mm thick aluminium plate softly connected on the surface was inserted between the motor and the load, as shown in Figure 5.3. For the sound pressure level measurements a B&K type 4134 microphone was used, fed from a B&K type 2804 power supply. The signal from the microphone was amplified using a B&K type 2639 amplifier and then sent to the analyzer. The microphone was calibrated using a B&K type 4220 piston-phone, taking into consideration the corrections that should be applied depending on the temperature and pressure measured inside the anechoic chamber.

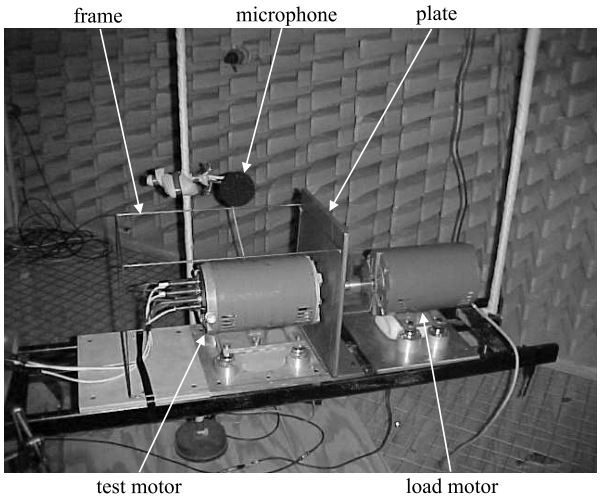

Figure 5.3: Set-up inside the anechoic chamber.

The equipment for driving the motor was placed outside the anechoic room, see Figure 5.4. The load motor was driven by an inverter type VSC2000, manufactured by Zener Electric. The inverter was set with a fixed switching frequency of 8 kHz. The test motor was driven from a conventional converter connected to a control system module developed at the Dept of Industrial Electrical Engineering and Automation, Lund University. The control module was fed by a separate voltage source and contained several cards with different functions: estimation of the flux from the three phase measured voltage, measurement of the current from two phases, and scaling of the d.c. link voltage in the converter. These signals were connected to the DSP card through a maximum of 16 analog inputs, and a 50 pin connector cable was used for the connection between the DSP and PWM cards. The switching frequency in the modulator was 20 kHz. The reference values for the direct and quadrature main currents in the DSP were set with two potentiometers, and the added noise currents were controlled by two separate signal generators. The response of the motor to random noise current excitation in the range from 0 Hz to 10 kHz was also tested using a separate B&K type 4205 sound power source. The microphone was connected to a HP 3569 A real time frequency analyzer, where the spectrum of

the measured noise was stored for further post-processing.

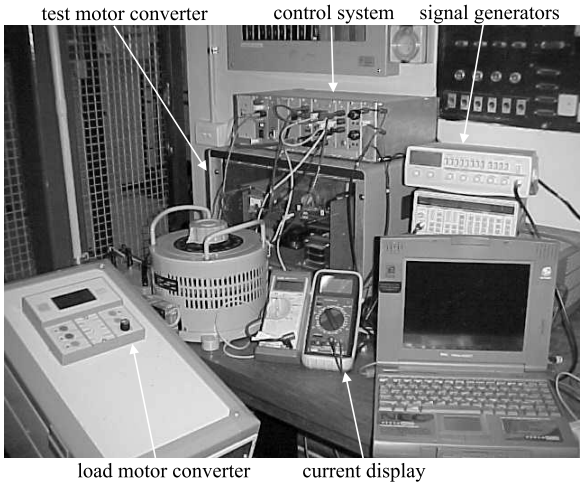

Figure 5.4: Set-up for the control equipment.

The noise components added from the signal generators had the same frequency, and different amplitude combinations were selected for the direct and quadrature currents, in order to study how the sound emissions were influenced by this phenomena. The maximum amplitude of the added noise current, defined as '2m', was determined taking into consideration the saturation limits in the machine. The value of the direct current was reduced so that when the noise current was added, the maximum value of the resultant waveform did not reach over the nominal value of the direct current, see Figure 5.5. The effective magnetizing current in the motor was equal to 2.21 A, which led to a peak direct current of 3.82 A, if the power invariant transformation is used. The maximum amplitude of the noise excitation, 2m, was selected to be 0.5 A, so the new d.c. value for the direct current became 3.82 - 0.5 = 3.32 A, which corresponds to 87% of the rated value. The rest of the excitation amplitudes for the experiments were selected corresponding to half and one quarter of the maximum excitation, i.e. 0.25 A and 0.125 A, defined as 'm' and 'm/2' respectively. The effective quadrature component of the current was equal to 3.6 A, which using the power invariant transformation led to a peak quadrature current of 6.23 A. In the same way as for the direct excitation, the current was reduced in order

not to reach over the nominal value when the noise excitation was added.

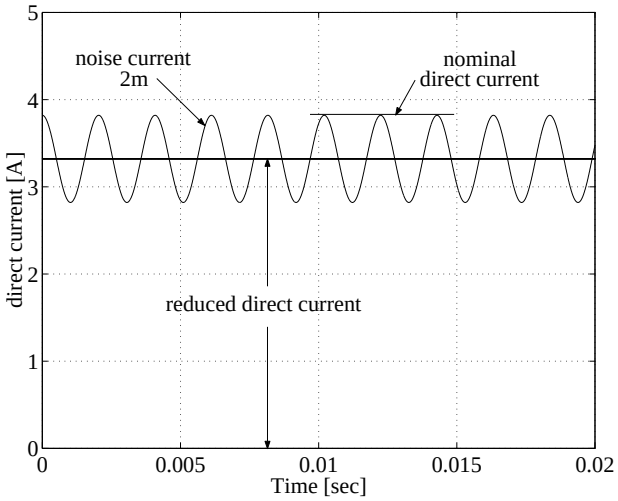

Figure 5.5: Modulation of the direct current.

The direct and quadrature currents calculated in the DSP were written in the digital outputs. Their d.c. components were displayed in two multimeters and their frequency components were checked in a ONO SOKKI CF-350 real time spectrum analyzer. The peak value was displayed using a hanning window and the spectrum was averaged for 256 samples with 50% overlap. The spectrum of the currents was flat except at the frequency of the noise added with the signal generators. Before starting the measurements, the amplitude of the noise current in the signal generators was adapted until the desired average value was obtained in the spectrum analyzer, corresponding to an amplitude of either '2m', 'm' or 'm/2' as described above.

Regarding the sound intensity measurements, a HP 35230 A sound intensity arm was used, equipped with two condenser microphones of the type HP 35237 A. The spacer used was 12 mm long, covering frequencies up to 5 kHz. The measurements were performed according to ISO 9614-2, which is a draft international standard for measurement of sound power via surface scanning of sound intensity. One requirement is to measure the residual intensity index for the entire measurement system. This value is directly related to the dynamic ca-

pability L_D, by subtracting 7 dB, and should be saved since ISO 9614 requires it to be compared with the reactivity index obtained from the measurements. If the reactivity index is greater than L_D in any 1/1 or 1/3-octave band, the sound power measurement is inadequate in that band. The residual intensity index of the measurement system was determined using a B&K ZI0055 pistonphone mounted on a B&K UA0914 sound intensity calibrator, and it is shown in Figure 5.6.

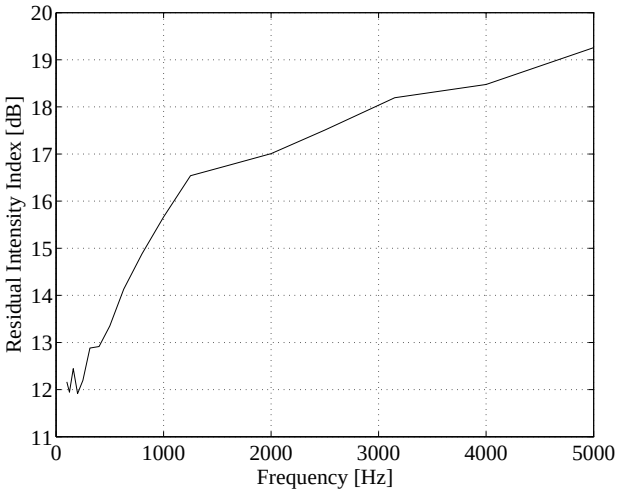

Figure 5.6: Measured residual intensity index.

Sound pressure as well as sound intensity measurements were conducted with the motor placed inside the anechoic chamber. The sound pressure measurements were carried first with the machine at stand still, and four different positions of the rotor were studied in order to quantify the importance of the eccentricity. The response was measured when two different excitation frequencies were used, at 490 Hz and 1105 Hz. These frequencies corresponded to two of the resonance frequencies of the stator-casing coupling measured experimentally. Different combinations of the amplitude of the direct and quadrature noise current components were selected, as shown in Figure 5.7. The case when the noise current is fed from the white noise source is noted with 'wn'. The same experiments were conducted with the machine rotating at 70 r.p.m. This low speed was selected in order to minimize the effects of the aerodynamic and

the mechanical noise. The sound intensity measurements require considerably more effort, and a lower number of combinations were tested, as shown in Figure 5.8. Under load, the same experiments as in no load were conducted, with the exception of the stand still tests.

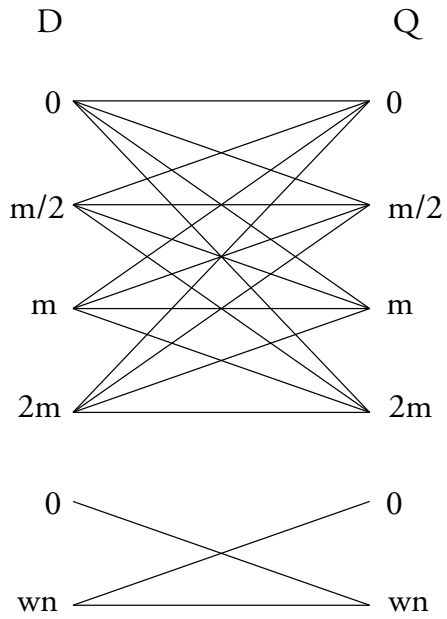

Figure 5.7: Diagram of combinations tested with SPL measurements.

5.5 No load tests results and analysis

Sound pressure tests of the motor at stand still and no load.

The measurements were conducted with the rotor fixed at four different positions, spaced 90 degrees between each other. In order to accurately determine the position of the rotor, a mechanical system was attached to the shaft and fixed to the test frame, as shown in Figure 5.9. Four holes were drilled around the wheel attached to the shaft, and by coupling them with the bar resting on the test frame the rotor was rotated to the desired position.

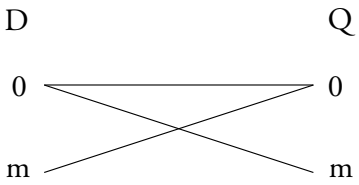

Figure 5.8: Diagram of combinations tested with PWL measurements.

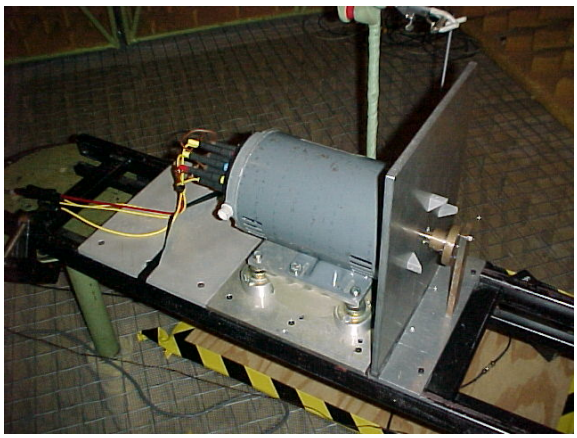

Figure 5.9: Set-up for the stand still tests.

The motor was fed with direct and quadrature current components corresponding to the combinations shown in Figure 5.7, with a frequency of 490 Hz and 1105 Hz. The sound pressure level measured with a single microphone inside the anechoic chamber were stored in the spectrum analyzer, where the resolution for the narrow band plot of the spectrum was 1600 lines in a range from 0 Hz to 6.4 kHz. These results were post-processed in order to obtain a single representative value for each measurement, which would serve as a basis for their comparison. This was achieved by adding the values at the 1600 point frequencies from the spectrum, using equation 5.2. An example of the results using this procedure is presented in Figure 5.10, which shows the spectrum at

the four positions for a noise excitation of amplitude 'm' and a frequency of 490 Hz, added both to the direct and quadrature currents. Above each window, the overall SPL both in dB and dB(A) is included.

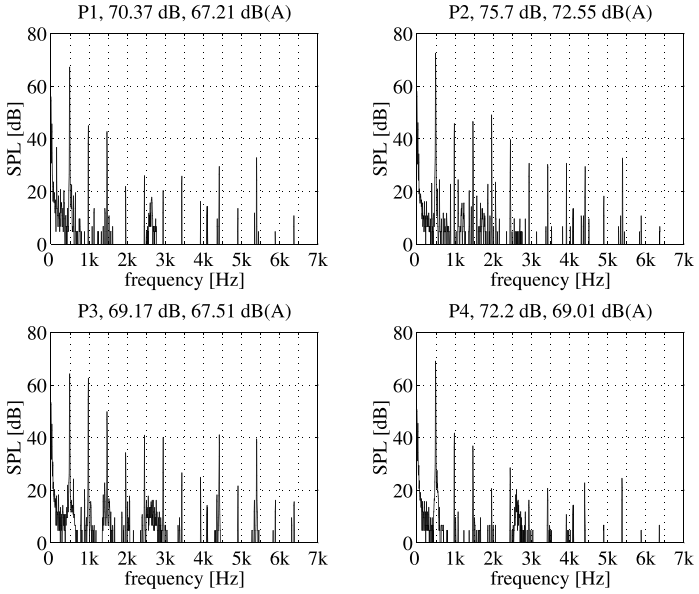

Figure 5.10: Measured SPL when d=m, q=m, f=490 Hz. No load, stand still at four different positions.

A comparison between all the cases at the four different positions is shown in Figure 5.11. This comparison is based on the total SPL in dB for each measurement, which was preferred to dB(A) since it gives more appropriate information about the real sound emitted from the motor, without been modified by any sensitivity factor.

In Figures 5.11, 5.12 and similar figures in this Chapter, the different cases are represented as a combination of two terms separated by a coma along the horizontal axis. The values of the curve corresponding to the 'd' current in the legend should be read as the case where the direct current corresponds to the first term and the quadrature current to the second term of the combination. And the opposite is applied for the values of the curve corresponding to the 'q' current in the legend: the quadrature current corresponds to the first term, and the direct current to the second term of the combination. For example, in the

combination [m/2,0] the value of the curve associated with the 'd' in the legend corresponds to the combination [d=m/2, q=0], whereas the value of the curve associated with the 'q' corresponds to the combination [d=0, q=m/2]. Also note that the combinations have been selected so that the value of the modulation of the first term is greater than the second one. This means that the d-curve will represent the cases when the modulation of the direct current is greater than the quadrature current (direct modulation), while the q-curve will correspond to the cases when the modulation of the quadrature current is greater than the direct current (quadrature modulation). Taking this into consideration, it can be observed that for every case the total L_p for the direct modulation is greater than the corresponding quadrature modulation. However, the values for the same case at different rotor positions may vary considerably, and this behaviour was associated with the variation of the eccentricity of the rotor with respect to the stator at the different positions, i.e. the dynamic eccentricity. In this case, the closest point between the stator and the rotor is shifted with the rotation, and the airgap at the point in the line of the microphone is changed. This in turn changes the airgap force, and hence the level of sound radiation in that direction.

The results obtained by averaging the values between the four different positions are presented in Figure 5.12. As it should be expected, the overall L_p increases with the level of modulation, from 'm/2' to '2m'. The graphs also show that, in all the cases, the level is higher when modulating the direct current than in the case of the quadrature current. At 490 Hz, the differences are around 7 dB when one of the noise currents is set to zero and the other one is modulated with different amplitudes. At 1105 Hz, the difference at these points changes from 4 dB to 9 dB. These increments are maintained at 1105 Hz when both currents are modulated, while at 490 Hz the direct and quadrature response are closer to each other. Comparing the results at both frequencies, the L_p at 490 Hz is around 10 dB higher than at 1105 Hz.

The main indications obtained from the stand still tests are the higher noise emissions obtained in the case of direct current modulation, as well as the influence of the dynamic eccentricity in the measurements. It is thus important to perform the measurements under rotation, in order to obtain an average value from all the positions of the rotor.

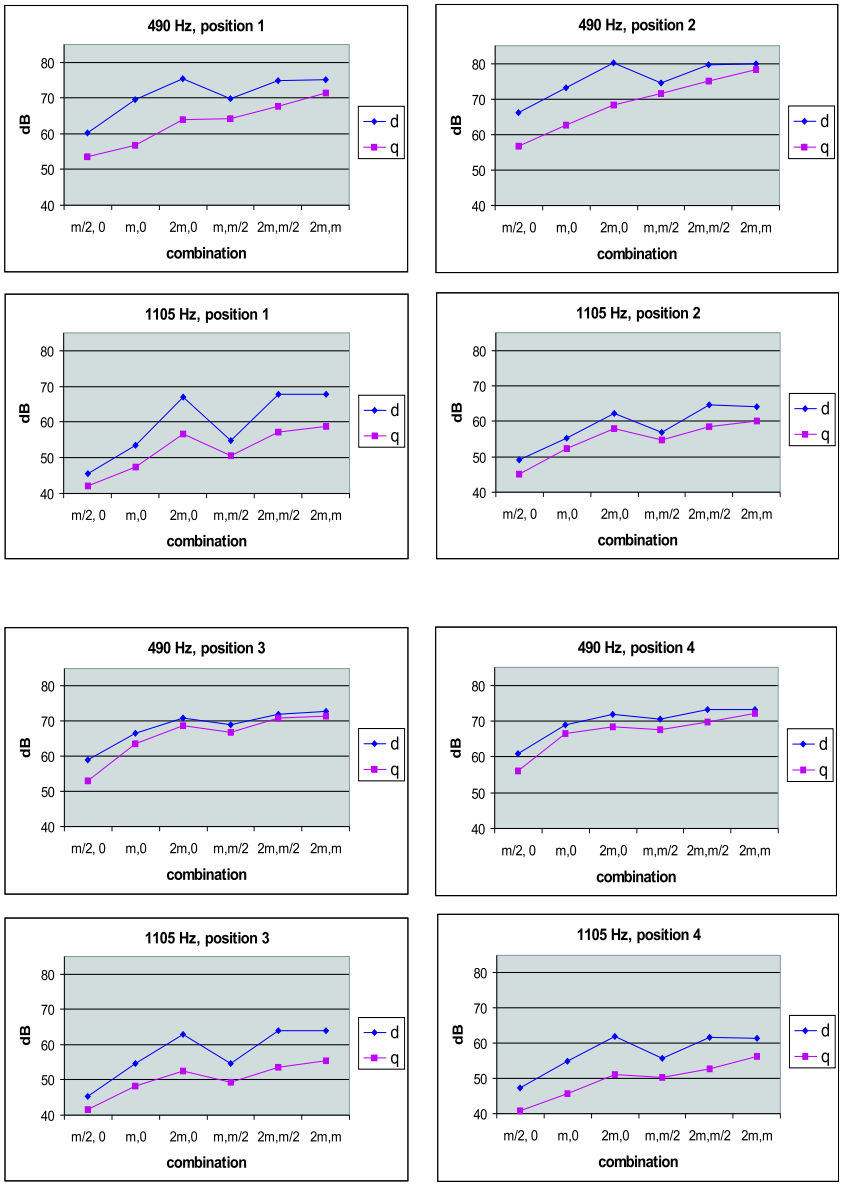

Figure 5.11: No load SPL at 4 different positions.

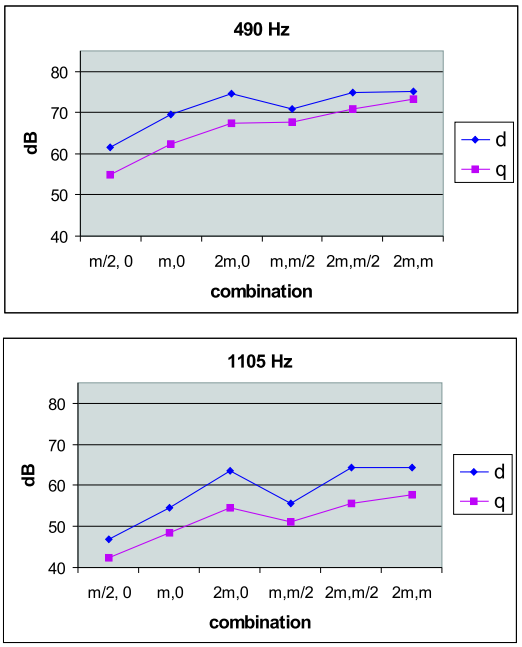

Figure 5.12: Averaged no load SPL results at stand still.

Sound pressure tests of the motor at low speed and no load.

The set-up for the experiments with the machine rotating was the same as for the stand still tests, now without any constrain in the shaft of the rotor. A low rotation speed of 70 r.p.m. was selected in order to minimize the mechanical noise caused by the vibrations of the machine. Also, the aerodynamic noise is reduced since the machine is cooled by means of a fan attached to the rotor. Nevertheless, the case when no noise current is added to the fundamental was also measured, in order to account for these effects. Since the switching frequency in the inverter is very high, around 20 kHz, it was assumed that no electromagnetic noise contributions with converter harmonic origin were produced in the frequency range for the measurement. In this way the contribution of the combined mechanical and aerodynamic noise was estimated, and the results are presented in Figure 5.13. The narrow band plot was post-processed

and converted into a 1/3 octave band plot, in order to improve its visual inspection. The centre frequency was calculated using equation 5.6 and the single L_p values for the frequencies included in each band were added using equation 5.2. The total L_p is included above the narrow band plot as the parameter *Lpav*.

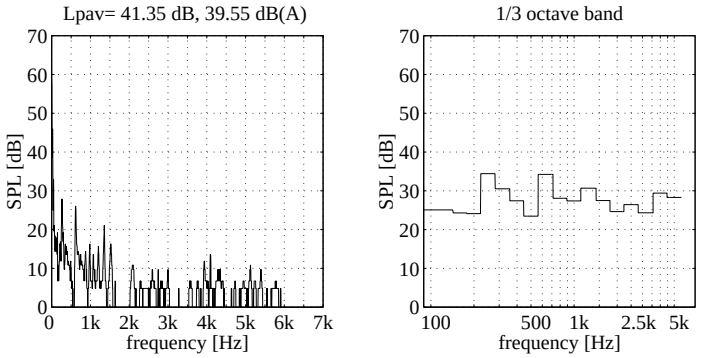

Figure 5.13: Measured SPL when d=0, q=0, no load, 70 r.p.m.

In order to see the rate of change in the noise emissions of electromagnetic origin, the direct and quadrature noise currents were fed alternatively from a white noise source, and the results are presented in Figures 5.14 and 5.15. It can be observed that the increase in the L_p when introducing the noise is in the order of 20 dB, which implies that the contributions of the mechanical and aerodynamic components can be neglected in the measurements.

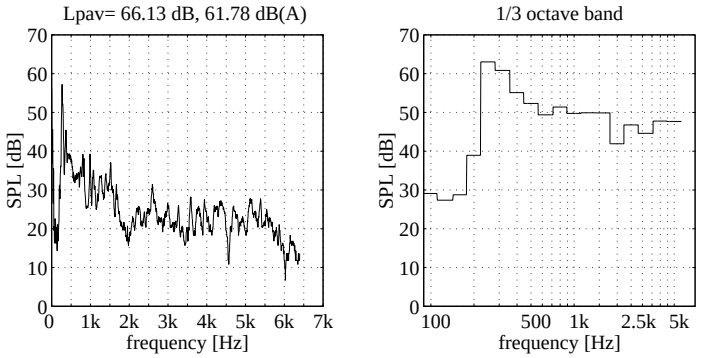

Figure 5.14: Measured SPL when d=wn, q=0, no load, 70 r.p.m.

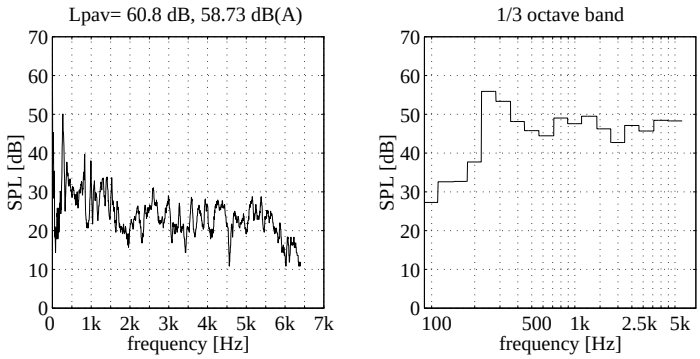

Figure 5.15: Measured SPL when d=0, q=wn, no load, 70 r.p.m.

A summary of the results for the different current excitations both at 490 Hz and 1105 Hz is presented in Figure 5.16. It can be appreciated that the direct modulation still produces more noise than the quadrature modulation. The difference is more accentuated at 490 Hz, where the average difference in sound pressure level is 5 dB, whereas at 1105 Hz this difference decreases to 2 dB. As in the stand still results, the L_p increases linearly with the modulation, except in the case of direct modulation when noise is added to both the direct and quadrature currents. Comparing both frequencies, the overall sound pressure level is higher at 1105 Hz compared to 490 Hz. The increment is more clearly visible in the quadrature modulation, with an average difference of 6 dB, than in the direct modulation, where the average difference is 3 dB.

Compared to the averaged results from the stand still tests, it can be appreciated that the SPL is lower when the machine rotates. Actually, the values from the stand still tests are not a good representation of the average around the whole motor. It might be the case that the values at the four positions give higher results compared with other positions along the circumference.

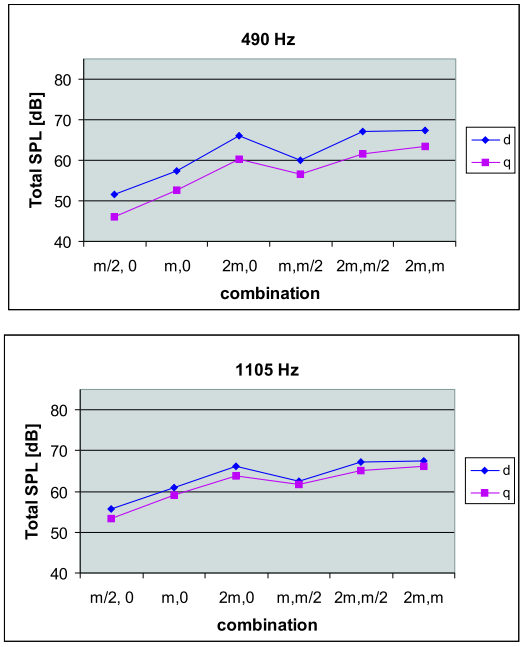

Figure 5.16: No load results at 70 r.p.m.

5.6 Load tests results and analysis

Sound pressure tests of the motor at low speed and load.

The machine was loaded with another identical asynchronous motor. A plate was set between the two machines in order to minimize the influence of the noise produced by the load in the sound measurements. Also, the load motor was covered with eight layers of barium loaded vinyl, with a thickness of 1 mm each approximately, so as to further reduce its noise emissions. The magnitude of the mechanical and aerodynamic noise from the load coupling were estimated as in no load, by measuring the noise emissions when no extra noise is added to the fundamental current. The results are presented in Figure 5.17, and compared to the no load case, it can be observed that the new coupling is producing less noise.

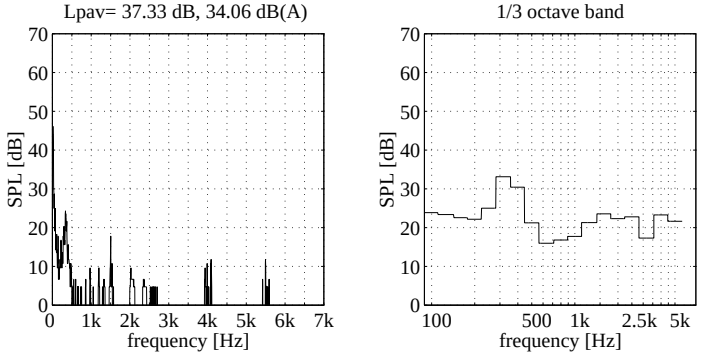

Figure 5.17: Measured SPL when d=0, q=0, load, 70 r.p.m.

As in no load, the increase in the noise emissions of electromagnetic origin was measured by feeding with white noise signals the direct and quadrature noise currents, and the results are presented in Figures 5.18 and 5.19. It can be observed that the increase in the sound pressure when the noise is modulated is around 25 dB, which leads to the conclusion that the aerodynamic and mechanical contributions to the overall noise can be neglected. Comparing these plots with the corresponding under no load, the noise produced when the machine is loaded is around 5 dB lower.

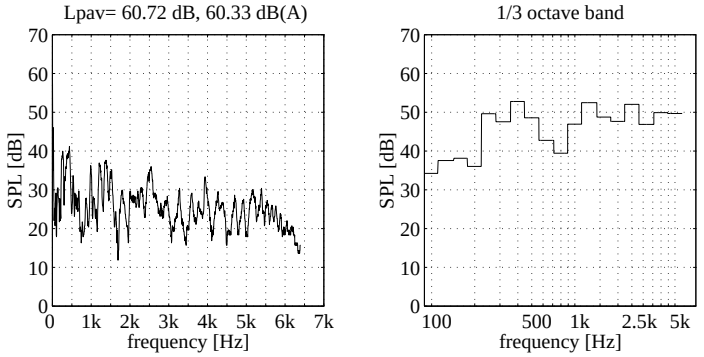

Figure 5.18: Measured SPL when d=wn, q=0, load, 70 r.p.m.

A summary of the results obtained for the different combinations of noise currents at the frequencies of 490 Hz and 1105 Hz is presented in Figure 5.20.

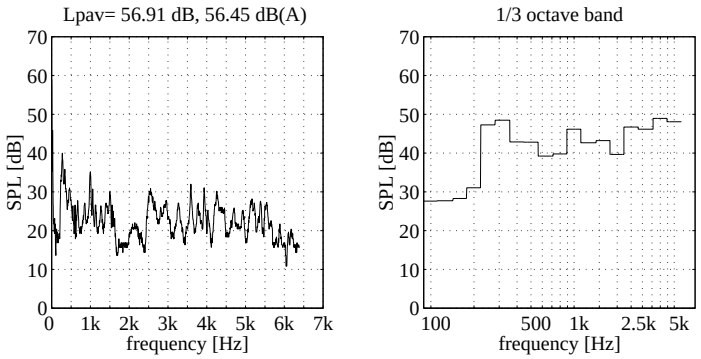

Figure 5.19: Measured SPL when d=0, q=wn, load, 70 r.p.m.

As well as it happened in the no load case, the noise emissions are increased in the direct modulation compared to the quadrature modulation, again by an averaged factor of 5 dB and 2 dB at 490 Hz and 1105 Hz respectively. The sound pressure level at 1105 Hz is also slightly higher than at 490 Hz, with an increment of 1 dB and 3 dB for the direct and quadrature currents respectively. Comparing the load and no load results, it can be observed that the sound pressure level decreases when the machine is loaded. The decrease in the direct and quadrature currents at 490 Hz is 6 dB and 4 dB respectively, whereas at 1105 Hz it reaches 8 dB for the direct current and 7 dB for the quadrature current.

5.7 Sound intensity measurements

The sound pressure measurements provide quick information about the level of noise at one particular point inside the anechoic chamber. However, due to the directionality of the sound radiation in an electrical machine, which can be quite different for different modes, the results obtained from one single point measurement are likely misleading. Using several microphones would provide more accurate results, but still the level of accuracy is limited. Hence, the most proper way to quantify acoustic noise from motors is to use sound intensity measurements, in order to determine the total sound power radiated. These measurements were conducted both under no load and load for the cases presented in Figure 5.8. For each case, the averaged spectrum of the sound intensity level flowing through each one of the four free sides of the frame containing

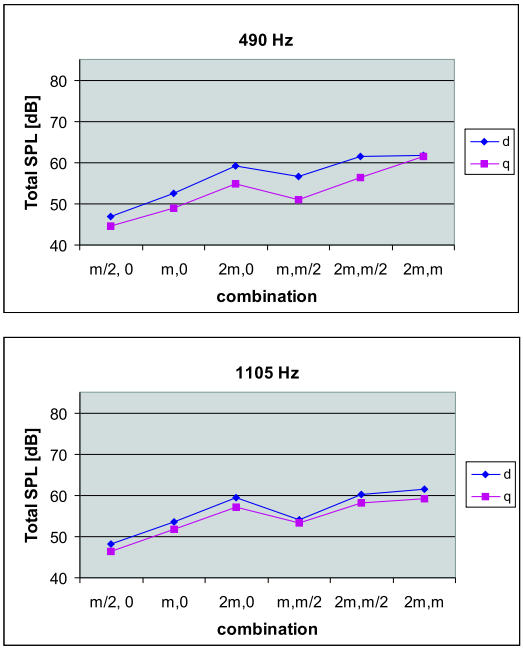

Figure 5.20: Load results at 70 r.p.m.

the motor was measured, and the results for the no load case are presented in Appendix C, and for the load case in Appendix D. These appendices present the values of the intensity measured through each side of the frame, as well as the measured reactivity index. In the plot of the reactivity index there are two dashed lines, which define the dynamic capability L_D of the system. With the exception of some low frequencies in the load measurements, it can be observed that the reactivity index is contained between the limits of the dynamic capability, which supports the validity of the sound intensity measurements.

From the measured sound intensity level in each side, the intensity can be obtained from equation 5.5, which multiplied by the area of that side leads to the power. Adding the contributions of all the free sides provides the total power radiated, and the sound power level is obtained using equation 5.3. The no load results are presented in Figure 5.22, and the load results in Figure 5.23. A comparison between the PWL at 490 Hz and 1105 Hz both in load and no

load is shown in Figure 5.21.

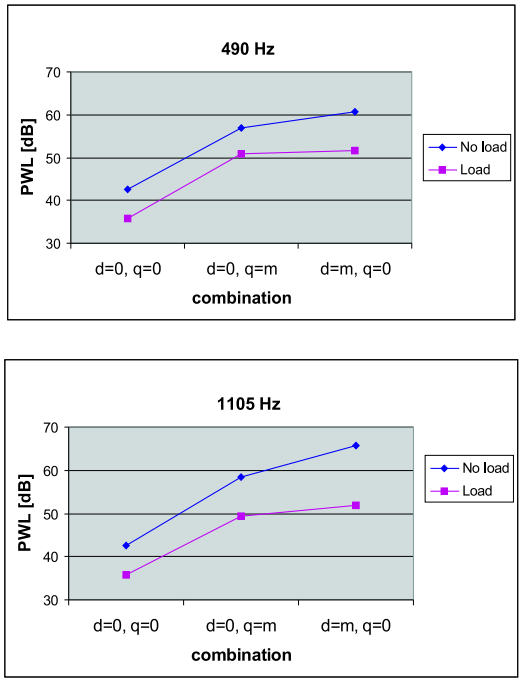

Figure 5.21: Comparison of sound intensity measurements results.

From all these results it can be observed again that the direct modulation produces more noise than the quadrature modulation. In no load the average difference is 4 dB at 490 Hz and 7 dB at 1105 Hz. Under load this difference is reduced to 1 dB and 3 dB at 490 Hz and 1105 Hz respectively. It can also be appreciated that the PWL at 1105 Hz is higher than at 490 Hz. In no load the increment in the direct current is 5 dB and in the quadrature current 2 dB. Under load this increment becomes 0.5 dB and 2 dB for the direct and quadrature current respectively. Finally, the PWL decreases when the machine is loaded. The decrease at 490 Hz when the direct current is modulated is 9 dB, and 6 dB in the case of the quadrature current. At 1105 Hz this decrease becomes 13 dB and 9 dB for the direct and quadrature current respectively.

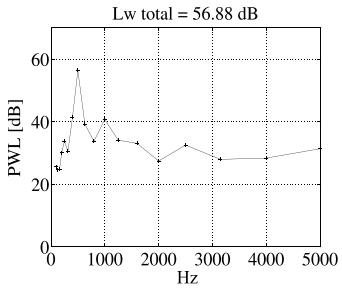

(a) d=0, q=m, 490 Hz.

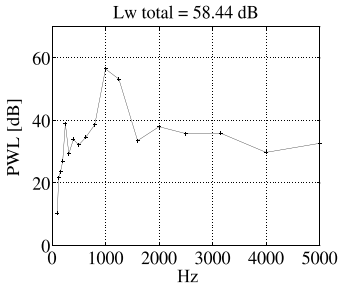

(b) d=0, q=m, 1105 Hz.

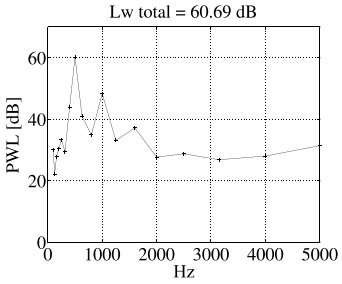

(c) d=m, q=0, 490 Hz.

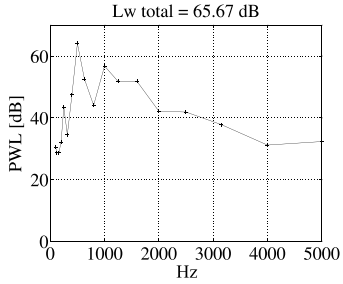

(d) d=m, q=0, 1105 Hz.

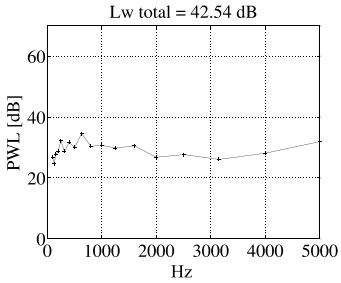

(e) d=0, q=0.

Figure 5.22: No load PWL results at 70 r.p.m.

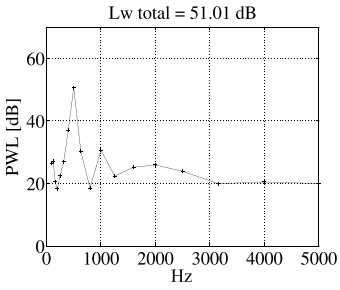

(a) d=0, q=m, 490 Hz.

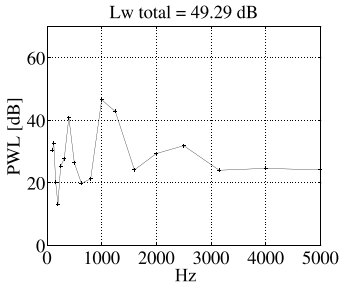

(b) d=0, q=m, 1105 Hz.

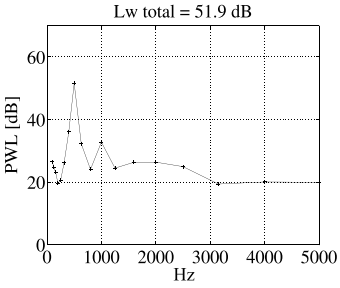

(c) d=m, q=0, 490 Hz.

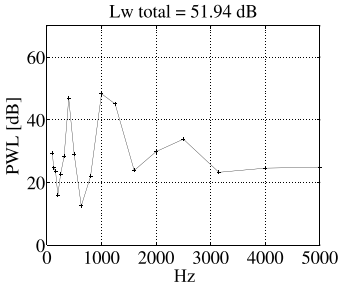

(d) d=m, q=0, 1105 Hz.

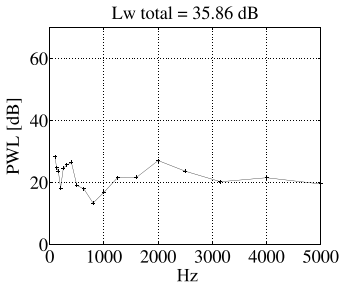

(e) d=0, q=0.

Figure 5.23: Load PWL results at 70 r.p.m.

5.8 Summary and Discussion

The no load stand still tests show a considerable change in the total sound pressure level at four different positions, indicating that the dynamic eccentricity is an important factor to consider in the test motor. Hence, an average value of the noise emitted at a certain position is obtained by operating the machine at low speed. This also minimizes the influence of the mechanical and aerodynamic noise in the measurements, which are found to be negligible compared to the noise produced by the electromagnetic forces.

The sound pressure measurements reveal that the noise emitted increases with the level of modulation almost linearly. The results from direct and quadrature modulation are closer at 1105 Hz compared to the 490 Hz case, and the level of noise measured at 1105 Hz is greater than at 490 Hz. This is due to the fact that these two frequencies excite different modes of vibration and hence the amplitude of the vibration in the direction where the microphone is placed may be quite different. The directional behaviour of the noise radiation implies that single point sound pressure measurements are likely misleading.

The most proper way of quantifying the acoustic noise from motors is to measure the sound power through sound intensity measurements, where all the space surrounding the motor is taken into consideration. These results show that direct modulation produces more noise than quadrature modulation, as well as the decrease in the noise emissions when the machine is loaded. The excitation of the motor structure can be more easily understood analyzing the movement of the flux vector from the stationary dq system. When the direct current is modulated, the amplitude of the flux vector fluctuates in the same direction as the d-axis, exciting the motor structure with radial forces. When the quadrature current is modulated the phase of the flux vector fluctuates around the d-axis, since the dq system can not follow the high frequency phase fluctuation of the flux vector. Hence, the path followed by the tip of the vector in this case is perpendicular to the d-axis. The magnitude of the radial component of the flux remains unchanged, whereas the tangential component fluctuates with the same frequency as the quadrature current. This movement implies that the amplitude of the flux vector is slightly changed, although the variation is very small for the level of the noise current considered. Hence, when the quadrature current is modulated it can be assumed that only tangential forces excite the motor structure. Although the radial and the quadrature excitations have the same amplitude and frequency, the acoustic response from the motor is different.

This indicates that the excitation of the mode of vibration at that frequency is somehow decreased when the quadrature current is modulated, and this might be due to the different physical response of the structure to the excitation.

In general, it can be observed that the noise emissions are considerably reduced under load, compared to the no load situation, and this could be due to the added stiffness provided by the coupling between the test motor and the load. However, since the influence of the mechanical forces was found to be negligible in the measurements, the cause for the noise reduction should have an electromagnetic origin. When the machine is loaded, the currents induced in the rotor are considerably increased, which contributes to decrease the flux level in the machine, and hence the electromagnetic stresses. Also, it is believed that the increased stiffness of the coupling would play an important role in reducing the influence of the eccentricity in the noise emissions, as well as the vibration of the rotor. The results from the sound intensity measurements also reveal that the difference in the noise emissions between direct and quadrature current modulation is importantly decreased when the machine is loaded. This seems to indicate a different physical behaviour of the structure when the machine is loaded, compared to the no load situation. Also, the large rotor current compared to the noise harmonics might damp down the electromagnetic response.

Chapter 6

Influence of stator structural changes in the noise emissions

6.1 Introduction

Adjustable-speed drives in industry and commercial buildings embodied as converter fed a.c. induction motor drives have a major drawback in increased magnetic noise. There is a devastating interaction between the fundamental airgap flux and harmonic components in the voltages and currents from the converter, but there are remedies. Numerous studies have been published about how to change the switching pattern in the converter in order to reduce these harmonics, or move them to a frequency range where the human ear is less sensitive. However, not enough efforts have been oriented towards a change in the structure of the motor, in order to reduce these noise emissions. The aim of this chapter is to evaluate the influence that several structural changes in the stator have in the acoustic behaviour of the machine.

Previous work

Some structural changes introduced at the department intended to isolate the outer surface of the stator, and therefore the surrounding air, from the vibrations transmitted through the teeth into the core. For this purpose some 'air gaps' could be introduced in the back of the core and this idea was already presented by Andersson and Skarrie (1997). They developed a theoretical study where the air gaps in the new mass-spring-mass system (inner core - air gaps - outer core) were optimized so as to reduce the vibrations of the new structure. A

prototype was built and tested but the experimental results showed that the new configuration did not improve the acoustic behaviour compared to the original structure. The work presented in this chapter has tried to contribute to the understanding of the mechanisms of noise production in this novel design, by studying the structural and acoustic behaviour using the FEM and BEM methods.

6.2 Basic model

The airgap forces excite the stator structure and the vibrations are transmitted through the teeth into the core, and then into the surrounding air. The stiffness of the teeth in the tangential direction is less compared to the core, and therefore they can contribute also to the vibration of the stator. This contribution becomes more important if the tangential airgap forces are big enough to induce a tangential movement of the teeth. However, the influence of the radial forces in the teeth is negligible, and these mainly serve as a path for the transmission of the excitation into the core. The studies presented in this chapter are only concerned with the transmission of the vibrations from the core into the surrounding air, independently if the teeth contribute or not to these vibrations.

The core was modelled in ANSYS as a cylinder using Solid45 elements, see Figure 6.1. In order to simulate the laminated nature of the structure, the Young modulus in the circumferential and in the longitudinal direction was different, $2.72\text{x}10^{9}$ and $1.36\text{x}10^{11}$ respectively. The element type and the physical properties of the cylinder correspond to the ones used in the stator of the motor presented in Chapter 4. These properties provided a good correlation between the experimental and simulated results from the modal testing analysis of the motor. The cylinder had an inner radius of 67.69 mm, an outer radius of 93 mm and a length of 60 mm, and the number of nodes an elements was 4032 and 3024 respectively. Since this model will also be used in SYSNOISE, the size of the elements had to be adapted in order to achieve good accuracy in the following acoustic calculations, which required a minimum of six elements per wave length. The upper frequency for the acoustic analysis was set to 5 kHz, and thus the maximum length allowed for any of the three dimensions of the elements was 11.33 mm. In order to meet this specification, the number of divisions along the circumferential and longitudinal directions were 72 and 6 respectively. With this distribution, the area of each element in the inner circumference became 2.1e-5 m^2. In the radial direction the structure was

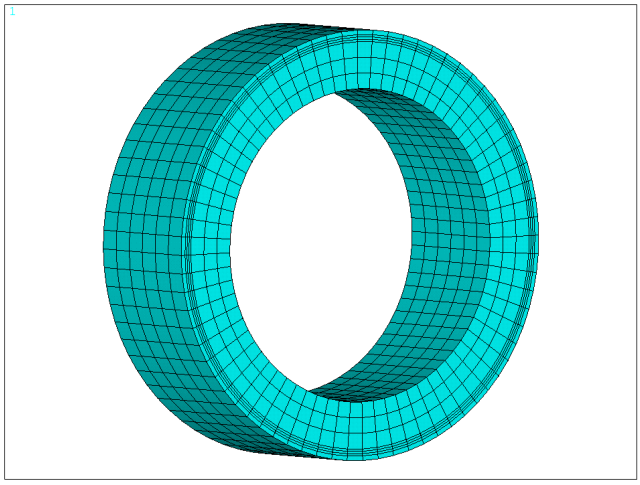

Figure 6.1: Cylindrical model of the core.

meshed in a series of layers graded towards the surface of the cylinder, where the modifications will be introduced.

There are generally two different methods for calculating the noise radiation from a structure in SYSNOISE. One method requires the use of an additional FEM software to calculate the vibration on the structure. This information is imported into SYSNOISE and thereafter a BE analysis is performed using the vibration information (either displacement or velocity), calculated previously in the FEM software, as the input to calculate the sound power. The second method consists on the use of the FEM software (ANSYS in this case) to perform a modal analysis so that the modal vectors are obtained and stored in a results file which is imported into SYSNOISE. Then, a FEM model is set up in SYSNOISE specifying the force as input and using the FEM model as well as the modal vectors from ANSYS to calculate the vibration response (displacement or velocity). After that, a BEM model is set up, where the vibration response calculated in the previous step is used as an input to calculate the radiated sound power. This second method is the one used for the SYSNOISE calculations in this thesis.

A modal analysis of all the structures presented in this chapter was per-

formed in ANSYS using the subspace method, and extracting all the modes of vibration up to 5 kHz. These modes, together with the geometry, were imported into SYSNOISE and the acoustic response was calculated for a magnitude of the applied stress equivalent to 5e-4 N/m^2, which corresponded to a force of 1.05 N at each element located in the inner surface of the cylinder. The components of the applied force at the nodes were set so that the magnitude of the force was the same for all the nodes and the direction pointing radially outwards. The BEM model was solved using the BE Indirect approach, which solves both the interior and exterior problems simultaneously, i.e. it assumes that the acoustic fluid is present on both sides of the surface, in the cavity and around the cylinder. In contrast, the BE Direct approach solves either the interior or exterior problem, and hence it assumes that there is fluid in only one side of the surface.

The acoustic results are taken directly from the SYSNOISE output file. It is important to distinguish between mechanical input power and vibration input power. The mechanical input power in the structure is defined as the product between the force and the vibration velocity at the driving point. In our case study, this power is converted into two components: the vibration input power of the structure and the power dissipated by structural damping. The vibration input power, in turn, produces acoustic power depending on the radiation efficiency. In the following, the vibration input power will be referred simply as input power. The calculation of the active sound power depends on the method used, i.e. BE Direct or BE Indirect. In the indirect method the formula for the input power is given by equation 6.1:

$$W_i = \rho c \int \bar{v}_n^2 dS \tag{6.1}$$

where ρ is the density of the fluid (air in this case), c is the speed of sound, $\bar{v}_n^2$ is the space average mean-square normal velocity of the surface, and S is the area of the radiating surface. The output power is calculated with equations 6.2 or 6.3, for the cases where velocity or pressure boundary conditions are defined respectively:

$$W_o = \frac{1}{2} \int \mu v^* dS \tag{6.2}$$

$$W_o = \frac{1}{2} \int \frac{p\sigma^*}{-ip\omega} dS \tag{6.3}$$

where μ is the potential, p is the pressure and σ is the radiation efficiency, which is calculated as:

$$\sigma = \frac{W_o}{W_i} \tag{6.4}$$

It should be noted that the radiation efficiency calculated in this way is equivalent to the definition found in the specialized literature, which is the ratio of the sound power radiated by the structure to the sound power radiated by a piston (which is large compared with the acoustic wavelength) vibrating with the same space-average mean-square velocity as the structure, see equation 6.5 (Harris, 1991). If the spatial velocity is uniform then the behaviour is like in the case of the piston. If the spatial velocity is not uniform, then the behaviour is similar to a piston with a uniform velocity equal to the spatial averaged velocity of the structure.

$$\sigma = \frac{W_o}{\rho c S \bar{v}_n^2} \tag{6.5}$$

These equations are evaluated through all the radiating surfaces, and the results for the active sound power will be similar as determining it over a closed surface enclosing the source, as it is done experimentally by means of sound intensity measurements. When using the BE Indirect method with two models (structural and acoustic), only the 'uncoupled' option is available for the simulation. This is due to the fact that the coupling is implicit when the two models are linked. In this link, the coupling between the fluid and the structure is defined, and the 'weak' option was used. This is valid when the fluid is air, since the modes of vibration of the structure are not modified by the surrounding fluid. Nevertheless, simulations were performed using a 'strong' coupling and the changes in the results were negligible.

The geometry analyzed presents a cavity, and therefore the 'non-uniqueness' problem may appear. This means that there is more than one solution at a given frequency, but it is not possible to know whether the solution has converged to the right answer. The unreal solutions correspond to the resonance frequencies of the cavity and when a solution is obtained for one of these frequencies, the only way of ensuring that the solution converges to a correct answer is to control that the sound pressure field inside the cavity does not become large because of resonance. When using a BE Direct method this can be achieved specifying a minimum number of points inside the cavity, where the sound pressure is

constrained to be zero. In this case the solution is 'overdetermined', since there are initially m equations and m unknowns but, by specifying additional points inside the cavity, new constraints are introduced overspecifying the problem. When using a BE Indirect method this problem is defined as a 'non-existence' problem, and the treatment is to add some impedance (absorption) inside the cavity. However, according to the SYSNOISE manual, impedance elements should not be used inside closed volumes in a BEM Indirect model which is linked to a structure. In this case, 'singularities' in the response will be due to physically-correct behaviour, the interaction of internal resonances of the volumes through the flexible structure to the exterior. Since all the models in this thesis are simulated by using a BEM Indirect model which is linked to a structure, the 'non-uniqueness' problem will not be present and no remedy is needed for this phenomena.

The superposition method was used for the acoustic analysis in SYSNOISE. This method is based on a linear summation of the contributions from the different modes. Each mode can be represented as a curve with a resonance at a certain frequency. The response at the resonance frequency is dominated by the mode at that frequency. At any other frequency, the response depends on the location of the nearby resonance frequencies and the amount of modes involved in the addition. The results obtained from the original model are presented in the following sections, where they are compared with other cases where some changes are introduced in the core structure.

6.3 Zig-zag gap model.

The shape of the zig-zag gap is shown in Figure 6.2. The gaps are distributed in two adjacent layers and shifted so that the radial component of the vibrations is prevented from escaping to the surrounding air by always hitting an air barrier. These gaps were located very close to the outer surface of the stator in order to reduce their interaction with the natural paths followed by the flux. The properties of the material are the same as in the basic model. The number of nodes remained constant, while the number of elements was reduced to 2448.

The fact that some iron material is replaced by air involves a decrease in the weight of the structure, which in turn affects the modal frequencies. The influence of this modification in the weight was studied comparing two cases: first, the density of the new model matched the density of the basic model, which implied a decrease of its total weight; and second, the density of the

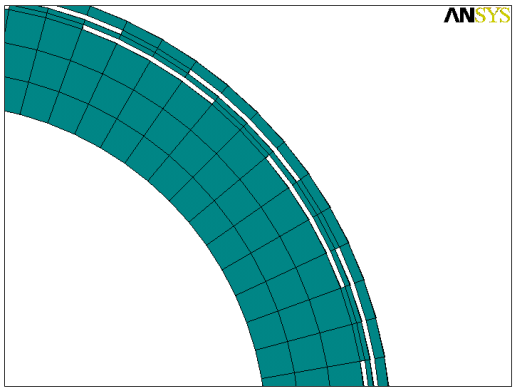

Figure 6.2: Zig-zag gap model.

new model was increased so that the weight matched the one from the basic model. The new modal frequencies of both zig-zag models were calculated in ANSYS and imported into SYSNOISE, where the same force as described in the previous section was applied, and the solution was obtained for all the modal frequencies from the different models.

The set up for the simulation is exactly the same as for the basic model. It should be noted that the frequencies of the zig-zag gap model with a new density would present slightly different resonance frequencies compared to the constant density case, but their response is still very similar, as shown in Figure 6.3. This figure shows a comparison between the total sound power level (PWL) radiated by the different structures, when a damping of 0.01 is used. The response of the two zig-zag models is very similar up to 3 kHz, and above that limit the curve of the constant weight model is slightly shifted to the left, as it would be expected since the modal frequencies decrease when the mass of the system is increased. Compared to the basic model, the response when the zig-zag gaps are included shows no sign of improvement, the overall sound power level is mainly shifted towards lower frequencies. There is a peculiar behaviour between 2 kHz and 3 kHz, characterized by a sudden decrease of the PWL. The radiation efficiency in this region is significantly more accentuated in the zig-zag model, as it is shown in Figure 6.4. From this Figure, it can be observed that above 4 kHz, even if the radiation efficiency is considerably lower in the zig-zag model, the PWL is higher compared to the basic one. This behaviour can be explained due

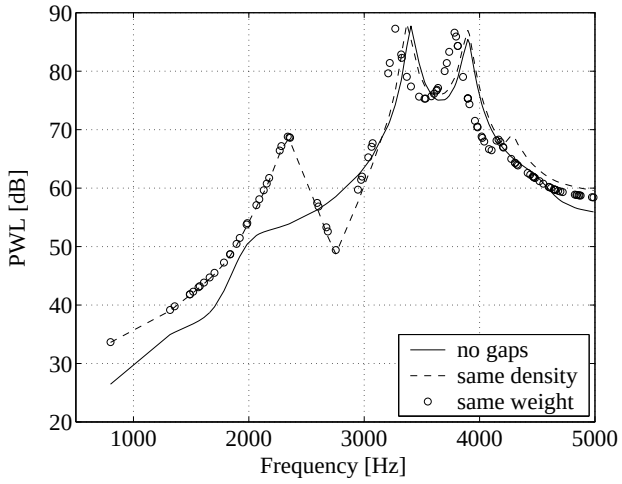

Figure 6.3: PWL of basic and zig-zag gap models, damping 0.01.

to the fact that the input power in this region is higher in the zig-zag model, as it is shown in Figure 6.5. Although the force applied is the same between the different models, so is not the input power because the structures are different. The structure with gaps is less stiff and has less mass, so it would be expected to present a higher response velocity and therefore higher input power.

The influence of the damping was also tested for the case of the structure with the zig-zag gap having the same weight as the basic model. The damping was increased up to 0.1 and decreased down to 0.001 and the results are presented in Figure 6.6. A decrease in the damping is followed by a higher PWL at the resonance frequencies above 3 kHz. When the damping is increased the response above 3 kHz experiments an important reduction of the PWL and the resonance peaks are no longer represented. This behaviour is explained since the input power is also reduced above 3 kHz due to the lower response velocity of the structure when the damping is increased, as shown in Figure 6.7.

The results obtained from this section agree with the experimental results presented by Andersson and Skarrie (1997), when a motor was built and tested using a stator of similar characteristics to the one presented in this section. That is, the acoustic response is not improved when the gaps are introduced around the stator, and it is characterized by a shift in the resonance frequencies.

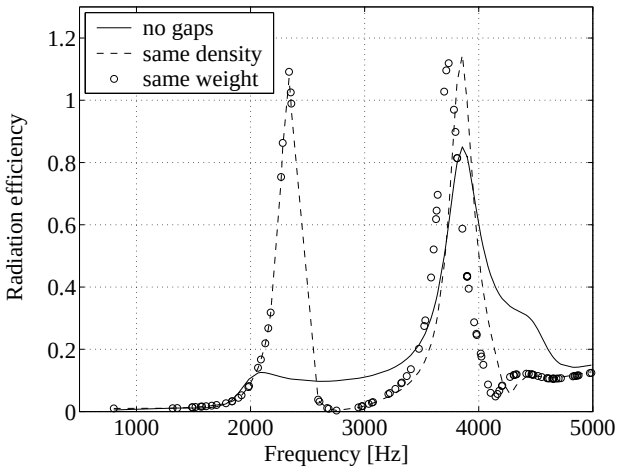

Figure 6.4: Radiation efficiency of basic and zig-zag gap models, damping 0.01.

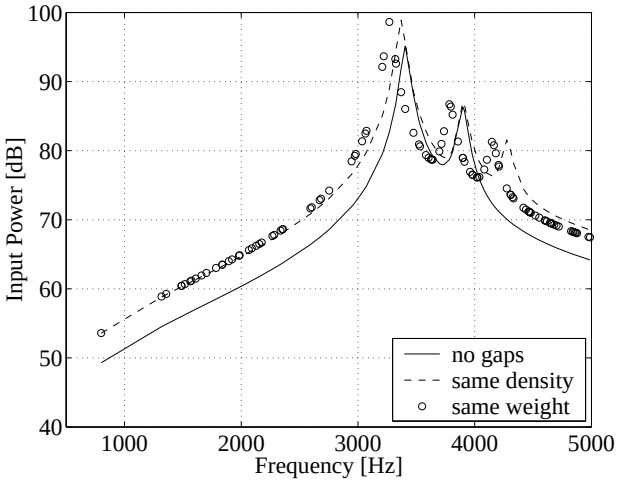

Figure 6.5: Input power of basic and zig-zag gap models, damping 0.01.

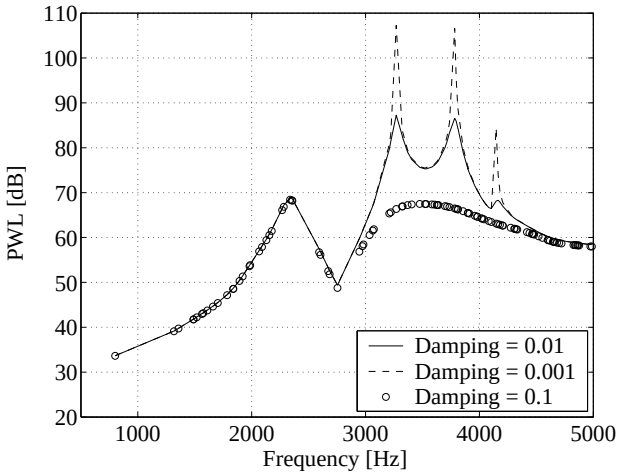

Figure 6.6: PWL of zig-zag gap model with constant weight for different dampings.

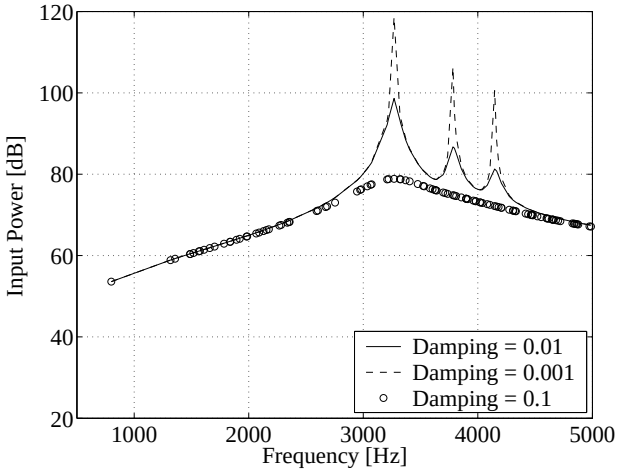

Figure 6.7: Input power of zig-zag gap model with constant weight for different dampings.

6.4 Four gap model

The idea of introducing the gaps in the back of the stator core was based in the assumption that the vibrations are mainly transmitted through iron and that the air barriers would contain these vibrations within the inner part of the core, thus isolating the outer part and also the surrounding air. The unsatisfactory results were initially attributed to the fact that the vibrations could still be transmitted through the thin iron paths located between the two air gap layers. Hence, reducing the amount of these paths would contribute to a better isolation, and this led to the study of a new geometry.

The new model was built replacing the iron by air between the gaps and also between the two layers in the zig-zag gap structure, leaving only four points of connection around the motor between the inner and outer parts of the core, see Figure 6.8. The new modes were calculated in ANSYS both when the weight and the density are maintained constant compared to the basic model. The material properties remained unchanged, and the amount of nodes and elements decreased to 3136 and 1800 respectively. The analysis in SYSNOISE presents the same characteristics as in the previous sections.

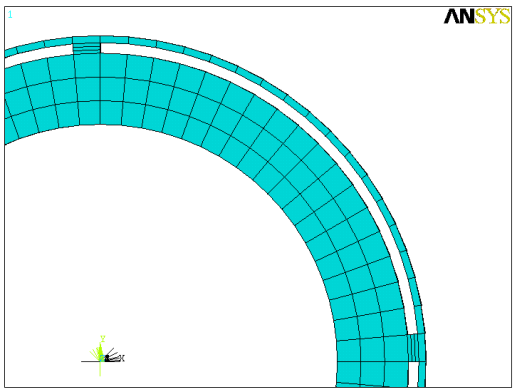

Figure 6.8: Four gap model.

The inner surface of the cylinder was excited with the same force used in the previous cases, and Figure 6.9 shows a comparison of the PWL obtained from the new structure and the basic model. The overall PWL is increased due to the fact that the four gap structure presents more resonance frequencies

within the same frequency range. The increase in the mass when the weight matches the one from the basic model is translated into a shift to the left of the curve below 2.5 kHz. The values obtained for the radiation efficiency are considerably higher than both the basic and zig-zag gap models, as shown in Figure 6.10. This behaviour corresponds to an input power considerably lower than the PWL at the resonance peaks above 2.5 kHz, as shown in Figure 6.11.

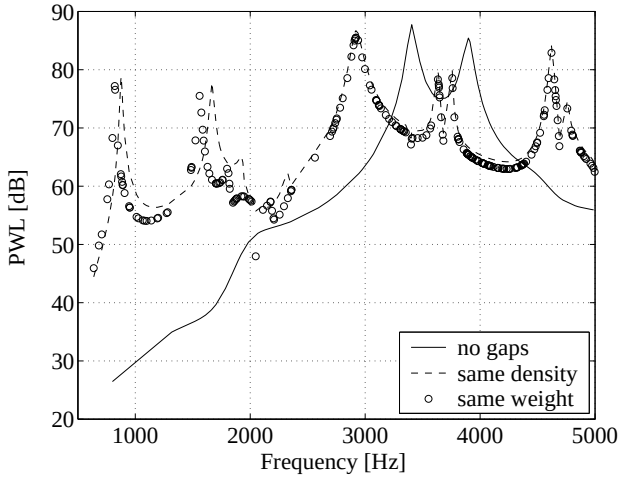

Figure 6.9: PWL of basic and four gap models, damping 0.01.

The influence of a change in the damping of the structure was also studied and the results are presented in Figure 6.12. The response below 2.5 kHz is amplified at the modal peaks when the damping is decreased while the PWL is considerably lower at those frequencies when the damping is increased. This behaviour is explained due to the lower input power below 2.5 kHz when the damping is increased, as shown in Figure 6.13. The reduction in the number of iron paths between the inner and the outer core is not corresponded with a decrease in the noise emissions. Actually, the acoustic behaviour of the structure is worsened, mainly due to the increase in the number of resonance frequencies that the structure presents within the same frequency range. A theoretical study where there are no connections between the inner and the outer parts of the core would reproduce the maximum achievable level of isolation.

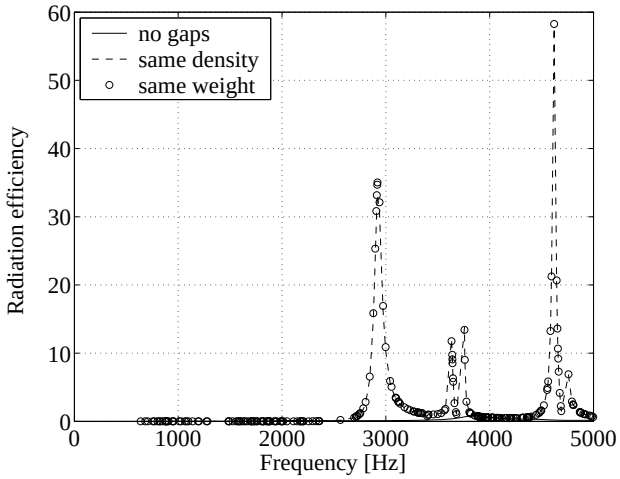

Figure 6.10: Radiation efficiency of basic and four gap models, damping 0.01.

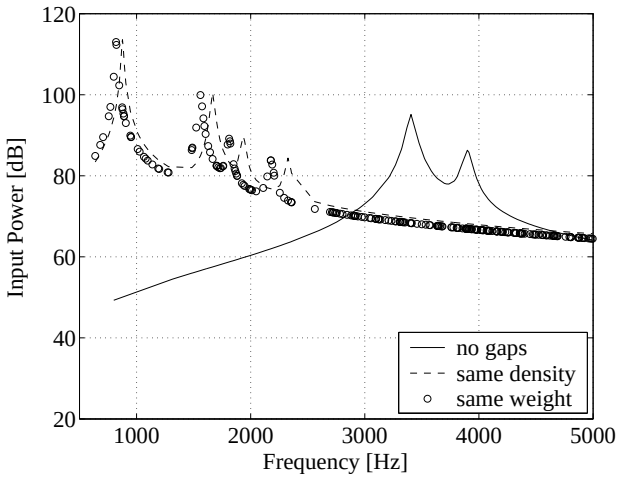

Figure 6.11: Input power of basic and four gap models, damping 0.01.

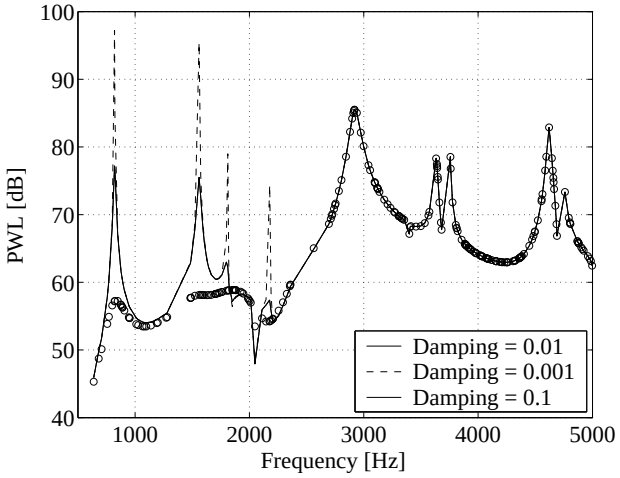

Figure 6.12: PWL of four gap model with constant weight for different dampings.

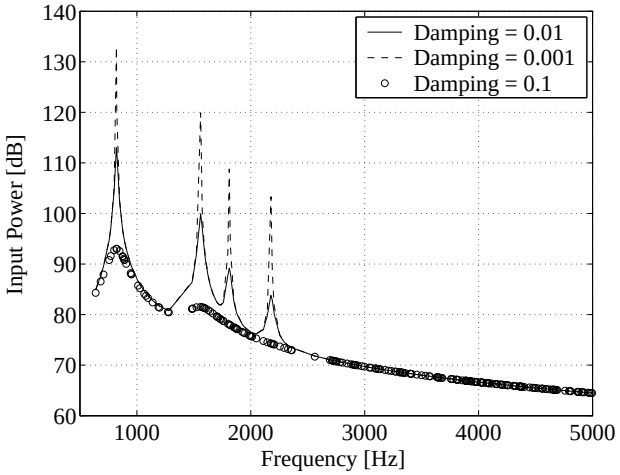

Figure 6.13: Input power of four gap model with constant weight for different dampings.

6.5 Ideal gap model

The ideal model was built setting a continuous gap which separates completely the inner and outer parts of the core, see Figure 6.14. The material properties remained unchanged and the number of nodes and elements were 3528 and 2160 respectively. This relative increase compared with the four gap model is due to the fact that one of the thin layers close to the surface was not replaced by air. Although there is no physical connection between the two rings, ANSYS calculated the modes for both of them. These modes were imported into SYSNOISE, where the same force used in the previous models was applied to the nodes in the inner surface of the cylinder. The set up for the simulation was exactly the same as in the previous cases.

It should be noted that the link between the inner cylinder and the outer cylinder is still provided through the air, which transmits the vibrations from the inner to the outer cylinder. As explained in section 6.2, the coupling between the fluid and the structure is implicit, and it is defined when the structural and the acoustic models are linked together. Both cases when the fluid-structure interaction is defined as 'weak' and 'strong' were simulated, and the change in the results was negligible. This is reasonable since the load of the air on the structure is not high enough to change its modes of vibration.

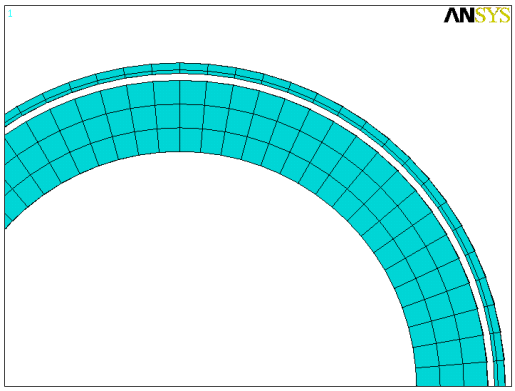

Figure 6.14: Ideal gap model.

Only the structure with the same weight as the basic model was simulated and the acoustical response is shown in Figure 6.15. The overall PWL is still

higher compared to the basic model, mainly in the region between 2 kHz and 3 kHz. The maximum PWL is achieved around 2.7 kHz, and at this frequency the radiation efficiency of the ideal model is considerably more pronounced, as shown in Figure 6.16.

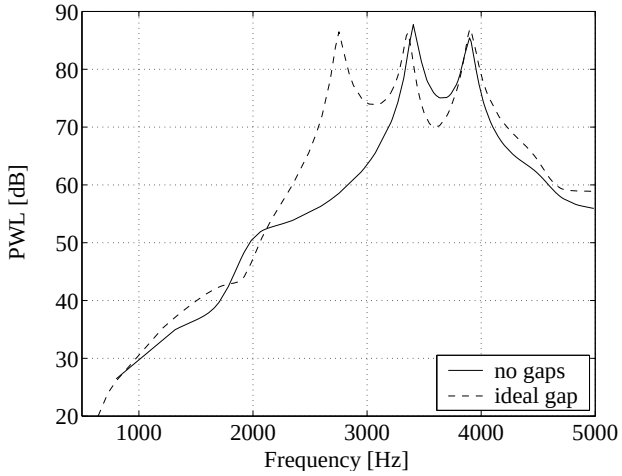

Figure 6.15: PWL of ideal gap and basic models, damping 0.01.

In order to investigate more in detail the noise radiation between 2 kHz and 3 kHz, the behaviour of the ideal gap model was compared to the basic model in that region. The basic model presents three modal frequencies, at 2176 Hz, 2357 Hz and 2753 Hz. The modes of the two rings in the ideal model were calculated separately in ANSYS. The inner ring presented exactly the same three modes of vibration as the basic model, but the frequencies were slightly higher, as it would be expected since the mass of the structure is decreased: 2246 Hz, 2357 Hz and 2846 Hz. Hence, the inner ring and the basic model can be considered to be acoustically equivalent between 2 kHz and 3 kHz. The outer ring presented 9 modes of vibration in this region. It was observed that the modes of vibration calculated for the inner ring and the outer ring separately coincided with all the modes of vibration calculated in ANSYS for the ideal gap model. Table 6.1 shows a comparison of the sound levels produced at the modal frequencies for the basic and the ideal gap models. The values with the superscript '*' in the ideal gap model correspond to the modes associated with

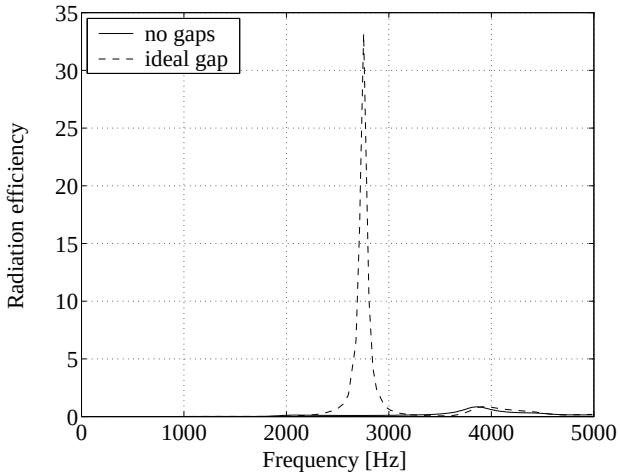

Figure 6.16: Radiation efficiency of ideal gap and basic models, damping 0.01.

the inner ring. The value with the superscript '**' corresponds to a modal frequency of both the inner and the outer rings. The rest of the modes calculated for the ideal gap are associated to the outer ring. From the table, it is clear that the outer ring is excited, and also that it is the responsible for the higher PWL obtained, compared to the basic model. The sound emitted at the frequencies corresponding to the inner ring modes is higher compared to the same modes in the basic model. This is due to the influence of the nearby outer ring modes, which are indeed very close. Also, note that the maximum response is obtained at 2721 Hz and that this mode is associated with the outer ring.

The results obtained indicate that not only the iron but also the air are the mediums conducting the vibrations from the inner to the outer part of the core. Even if the transmission coefficient through the air is lower compared to the iron, the fact that the stiffness of the outer part of the cylinder is considerably decreased by removing iron material is a key factor in the acoustical behaviour of the new structures. On one hand the outer core introduces more modal frequencies within the same frequency range. On the other hand, the outer core is also more easily deformed, which makes it more sensitive to the vibrations transmitted from the inner core. Some of the modes of vibration calculated in ANSYS for the different structures are shown in Figures 6.17, 6.18 and 6.19.

Basic model	*Ideal Gap model*
	2076 Hz: 50.7 dB
2176 Hz: 52.9 dB	2246 Hz: 56.7 dB*
	2278 Hz: 57.7 dB
	2336 Hz: 59.7 dB
2357 Hz: 53.9 dB	2357 Hz: 60.4 dB**
	2604 Hz: 71.9 dB
	2675 Hz: 78.0 dB
	2721 Hz: 83.7 dB
	2805 Hz: 82.1 dB
	2842 Hz: 72.9 dB
2753 Hz: 58.5 dB	2846 Hz: 79.0 dB*

Table 6.1: Comparison between the modal frequencies for the basic and ideal gap models.

It is illustrated how the degree of deformation experienced in the outer part of the core is more accentuated than in the inner part, and this contributes to the radiation of noise, which explains the unsatisfactory results obtained from the models where the surrounding airgap is introduced.

6.6 Summary and Discussion

In this chapter the effect of some structural changes in the stator of the motor with the aim of reducing the noise emissions has been discussed. The structural change consisted on introducing some air gaps around the periphery of the stator so as to interfere with the transmission path for the vibrations. Different geometries for the gaps have been presented, together with the ideal case, where the outer core is not physically connected through iron with the inner core.

The results presented in this chapter indicate that the idea of introducing air gaps in the periphery of the stator core does not reduce the transmission of the vibrations to the surrounding air, which would reduce the noise emitted. Replacing some iron by air reduces the stiffness in this area and makes the structure more sensitive to vibration excitation. However, it has also been discussed that an increase in the damping of the material is translated into a decrease of the noise emissions. The damping could be increased filling the slots with composite damping materials with high thermal and magnetic conductivity.

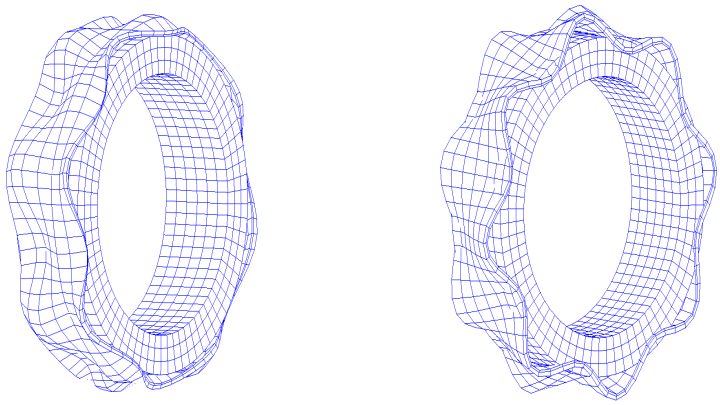

(a) Mode 81, 3397 Hz. (b) Mode 89, 3546 Hz.

Figure 6.17: Modes of vibration in the ideal model.

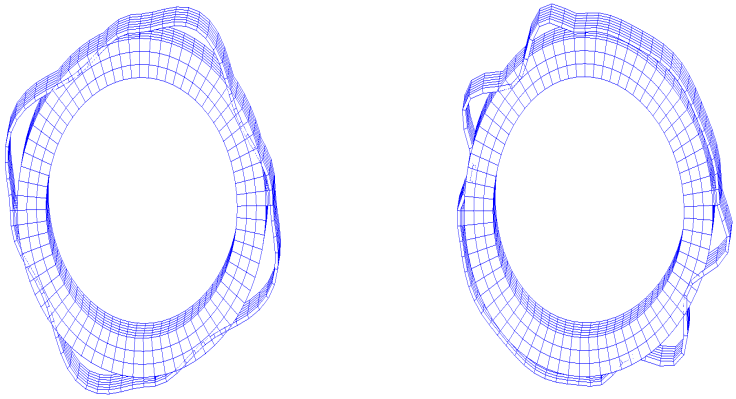

(a) Mode 6, 848 Hz. (b) Mode 58, 2918 Hz.

Figure 6.18: Modes of vibration in the four gaps model.

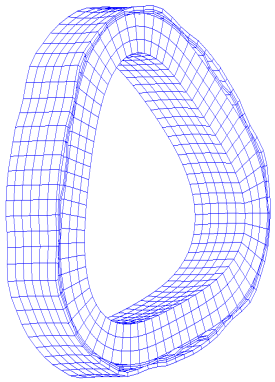

(a) Mode 35, 3640 Hz.

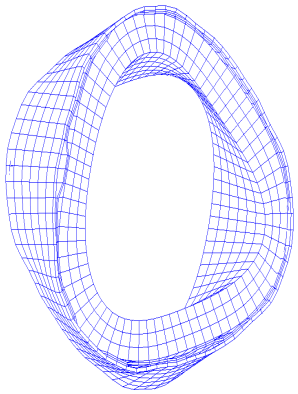

(b) Mode 37, 3716 Hz.

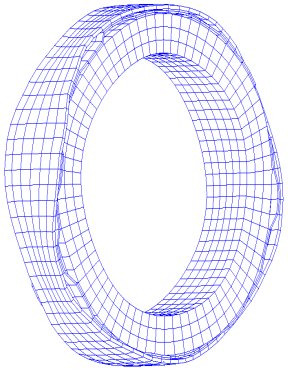

(c) Mode 68, 4618 Hz.

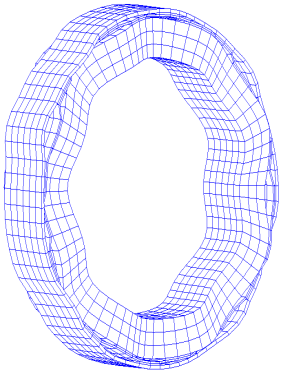

(d) Mode 69, 4659 Hz.

Figure 6.19: Modes of vibration in the zig-zag gap model.

Chapter 7

Conclusions

7.1 Summary

In this thesis, the acoustic noise emissions from vector controlled induction motor drives have been analyzed. Vector control provides faster transient response compared to conventional v/f drives, and this is achieved with an efficient decoupling of the currents controlling the flux and the torque in the machine.

A simulation platform including the control system and simplified models for the power electronics, motor and observers has been presented. The control system has been implemented in a DSP card and the performance of the drive was successfully tested modulating high frequency signals as noise references added to the direct and the quadrature currents.

A method for the prediction of the sound radiation from an electrical motor has been analyzed, based in the combination of structural and electromagnetic finite element models, together with an acoustic boundary element model. It was found that the level of agreement between the noise calculations and the measurements is sensitive to a few different factors. From the structural point of view, it is important that the modes of vibration are properly calculated in the structural analysis, so that the acoustic model behaves in a similar way as the experimental motor. It was also observed that a change in the damping influenced the response at some frequencies considerably, while at others the behaviour remained basically unchanged. From the electromagnetical point of view, using a two-dimensional model for the induction motor implies that the skewing of the rotor bars can not be modelled, which in turn affects the force calculations since the rotor harmonics are not damped. A change in the material

magnetic properties, which consisted in a 10% increase of the flux density in the saturated part of the BH curve, produced an increase of 3 dB or less in the simulated acoustic response.

Regarding the sound measurements, the directional behaviour of the noise radiation from electrical machines implies that the most proper way of quantifying their acoustic noise emissions is to measure the sound power through sound intensity measurements. It was observed that the direct and the quadrature current modulation can be associated to the radial and the tangential excitation of the motor structure respectively. Although both components were excited with noise signals of the same amplitude and frequency, the acoustic response was higher when the direct current was modulated. This indicates that the excitation of the mode of vibration at that frequency is somehow decreased when the quadrature current is modulated, and this phenomena is probably related to the different physical response of the structure to the excitation in both cases.

When the machine was loaded it was observed that the overall sound emissions decreased. The electromagnetic reason for this behaviour is the decrease of the flux level at load, which in turn influences the stresses. It is also believed that the stiffness of the coupling with the load would play an important role in reducing the vibration of the rotor and the degree of eccentricity. The acoustic response for the direct and the quadrature current modulation is much more similar at load, which indicates a different behavior of the structure when the machine is loaded, compared to the no load situation. Also, the large amplitude of the rotor currents compared to the noise harmonics can contribute to damp the electromagnetic response.

The effect of introducing air gaps around the periphery of the stator, in order to interfere with the path for the vibrations and reduce the noise emissions, was also tested. However, it was observed that the stiffness in this area is decreased, which makes the structure more sensitive to vibration excitation, actually radiating more noise than the original model.

7.2 Future work

The prediction of the noise emissions from an induction motor has been tested using some of the most advanced computational tools available in the market. However, the results show that it is difficult to obtain a good correlation between the simulations and the measurements. In order to reproduce the acoustic behaviour of an electrical machine, an accurate representation of its structural

and electromagnetical properties is required. The FEM modal analysis referred in this thesis needs to be improved below 1 kHz. The models should also be validated at frequencies higher than 2 kHz. This can be achieved by increasing the sampling frequency in the electromagnetic calculations to approximately double, and comparing the acoustic simulation with the results obtained adding a 1105 Hz noise component to the currents. At this frequency, the predicted and measured modes of vibration show a better agreement than at 490 Hz. Also, the airgap forces should be extracted from the three-dimensional model, in order to take into account the influence of skewing.

The results from Chapter 6 indicated that an increase in the damping of the material is translated into a decrease of the noise emissions. New ways of increasing homogeneously the damping in the stator structure could be investigated. In particular, iron powder has increasingly been used in the construction of electrical machines in the last years, allowing the exploration of new geometries that could be hardly achieved from laminated structures. In principle, iron powder machines would present a higher damping factor in the radial direction compared to the laminated structure, due to the presence of insulating material around the iron particles. However, the damping in the extrusion direction is expected to be higher in the laminated stator, due to the thicker layer of insulation between the laminations. Nevertheless, the study of the acoustic behaviour of such structures is needed in order to assess the acoustic characteristics of this material.

Bibliography

Andersson, C., Skarrie, H. (1997). *Mekanisk ljudreducering i en asynkronmaskin*. Dept of Industrial Electrical Engineering and Automation, Lund University, Sweden. MSc. Thesis.

Alaküla, M., Olsson G., Svensson T. (1995). *Styrning av elektriska drivsystem*. KF Sigma, Dept of Industrial Electrical Engineering and Automation, Lund Institute of Technology, Lund, Sweden.

Bakhuizen, A.J.C. (1973). *A contribution to the development of stepping motors* Eindhoven Technical University, Netherlands. Ph.D. Thesis.

Belkhayat, D., Roger, D., Brudny, J.F. (1997). Active reduction of magnetic noise in asynchronous machines controlled by stator current harmonics. *EMD'97. Proceedings of the Eighth International Conference in Electrical Machines and Drives*, pp. 400–405, IEE, London, UK.

Belmans, R., Verdyck, D., Geysen, W., Findlay, R.D. (1991). Electromechanical analysis of the audible noise of an inverter-fed squirrel-cage induction motor. *IEEE Transactions on Industry Applications*, vol. 27, no. 3, pp. 539–544.

Belmans, R., Hameyer, K. (1998). Impact of inverter supply and numerical calculation techniques in audible noise problems. *International seminar on vibrations and acoustic noise of electric machinery*, pp. 9–23. Béthune, France.

Bologniani, S., Di Bella, A., Zigliotto, M. (1999). Random modulation and acoustic noise reduction in IM drives: a case study. *EMD'99. Proceedings of the Ninth International Conference on Electrical Machines and Drives*, pp. 137–141, IEE, Canterbury, UK.

Brüel & Kjær (1986). *Sound Intensity booklet*.

Brüel & Kjær (1988). *Structural testing. Part 2: Modal analysis and simulation*.

Chang, S.C., Yacamini, R. (1996). Experimental study of the vibrational behaviour of machine stators. *IEE Proceedings on Electrical Power Applications*, vol. 143, no. 3, pp. 242–250.

Chau, K.T., Jiang, S.Z., Chan, C.C. (2000). Reduction of current ripple and acoustic noise in dual-inverter pole-changing induction motor drives. *PESC'00. Record of the 31th Annual IEEE Power Electronics Specialists Conference*, vol. 1, pp. 67–72.

Cho, D.H., Kim, K.J. (1998). Modelling of electromagnetic excitation forces of small induction motor for vibration and noise analysis. *IEE Proceedings on Electrical Power Applications*, vol. 145, no. 3, pp. 199–205.

Delaere K., Hameyer K., Belmans, R. (1998). Static eccentricity as a cause for audible noise of induction motors. *ICEM'98. Proceedings of the International Conference on Electrical Machines* vol. 1, pp. 502–506, Istanbul, Turkey.

Ewins, D.J. (1984). *Modal testing: theory and practice* Research Studies Press Ltd.

Garvey, S.D., Glew, G.N. (1999). Magnetostrictive excitation of vibration in machines - a modal approach. *EMD'99. Proceedings of the Ninth International Conference on Electrical Machines and Drives*, pp. 169–173, IEE, Canterbury, UK.

Garvey, S.D., Le Flem, G.D. (1999). Tangential forces matter. *EMD'99. Proceedings of the Ninth International Conference on Electrical Machines and Drives*, pp. 174–178, IEE, Canterbury, UK.

Gerling, D. (1994). The audible noise of induction machines compared for different methods of calculating the air-gap field. *ICEM'94. Proceedings of the International Conference on Electrical Machines*, vol. 3, pp. 409–414, Paris, France.

Hadj Amor, A., Timar P.L., Poloujadoff M. (1995). Induction squirrel cage machine design with minimization of electromagnetic noise. *IEEE Transactions on Energy Conversion*, vol. 10, no. 4, pp. 681–687.

Harris, C.M. (1991). *Handbook of acoustical measurements and noise control*. McGraw-Hill.

Holmes, D.G. (1997). *A generalized approach to the modulation and control of hard switched converters*. Dept of Electrical and Computer Systems Engineering, Monash University, Australia. Ph.D. Thesis.

Hupe, R., Kennel, R. (1989). Increase of power and reduction of noise and current ripple of inverter fed induction machines. *EPE'89. Proceedings from the Third European Conference on Power Electronics and Applications*, pp. 47–50, Aachen, Germany.

Ishibashi, F., Noda, S., Mochizuki, M. (1998). Numerical simulation of electromagnetic vibration of small induction motors. *IEE Proceedings on Electrical Power Applications*, vol. 145, no. 6, pp. 528–534.

Kobayashi, T., Tajima, F., Ito, M., Shibukawa, S. (1997). Effects of slot combination on acoustic noise from induction motors. *IEEE Transactions on Magnetics*, vol. 33, no. 2, pp. 2101–2104.

Krause, P.C. (1986). *Analysis of Electric Machinery*. McGraw-Hill.

Lai, J.C.S. (2000). *Acoustic Noise*. Course Notes, AMEC 4002. University College, The University of New South Wales, Australia.

Låftman, L. (1997). The Contribution to noise in an induction machine, fed from a pulse width modulated inverter. *EPE'97. Proceedings from the Seventh European Conference on Power Electronics and Applications*, vol. 2, pp. 2483–2489, Trondheim, Norway.

Lipo, T.A. (1996). *Introduction to AC machine design*. WisPERC UW, Madison Wisconsin, USA.

Maliti, K.C. (2000). *Modelling and analysis of magnetic noise in squirrel-cage induction motors*. Dept of Electric Power Engineering, Electrical Machines and Power Electronics, Royal Institute of Technology, Stockholm, Sweden. Ph.D. Thesis.

Martínez Muñoz, D., Pulle, D.W.J., Alaküla, M., Weibull, H. (1999). A drive system for acoustical analysis. *EMD'99. Proceedings of the Ninth International*

Conference on Electrical Machines and Drives, pp. 147-150, IEE, Canterbury, UK.

Ramesohl, I., Kaehler, C., Henneberger, G. (1999). Influencing factors on acoustical simulations including manufacturing tolerances and numerical strategies. *EMD'99. Proceedings of the Ninth International Conference on Electrical Machines and Drives*, pp. 142–146, IEE, Canterbury, UK.

Stemmler, H., Eilinger, T. (1994). Spectral analysis of the sinusoidal PWM with variable switching frequency for noise reduction in inverter-fed induction motors. *PESC'94. Record of the 25th Annual IEEE Power Electronics Specialists Conference*, vol. 1, pp. 269–277.

Vandevelde, L., Melkebeek, J.A.A. (1994). Theoretical and experimental study of radial forces in relation to magnetic noise of induction motors. *ICEM'94. Proceedings of the International Conference on Electrical Machines*, vol. 3, pp. 419–424, Paris, France.

Vandevelde, L., Melkebeek, J.A.A. (1997). Calculation of radial magnetic forces for the analysis of noise and vibrations of squirrel-cage induction motors. *EMD'97. Proceedings of the Eighth International Conference in Electrical Machines and Drives*, pp. 86–90, IEE, London, UK.

Verma, S.P., Balan, A. (1998). Experimental investigations on the stators of electrical machines in relation to vibration and noise problems. *IEE Proceedings on Electrical Power Applications*, vol. 145, no. 5, pp. 455–461.

Wang, C. (1998). *Vibro-acoustic analysis of inverter driven induction motors*. School of Aerospace and Mechanical Engineering, University College, The University of New South Wales, Australia. Ph.D. Thesis.

Wang, C., Lai, J.C.S. (1999). Vibration analysis of an induction motor. *Journal of Sound and Vibration*, 224(4), pp. 733–756.

Wang, C., Lai, J.C.S., Pulle, D.W.J. (2000). Prediction of acoustic noise from variable speed induction motors: deterministic vs. statistical approaches. *Record of the 2000 IEEE Industry Applications Conference*, vol. 1, pp. 471–478.

Xu, L., Zhu, Z.Q., Howe, D. (2000). Acoustic noise radiated from direct torque controlled induction motor drives. *IEEE Proceedings on Electric Power Applications*, vol. 147, no. 6, pp. 491–496.

Zhu, Z.Q., Xu, L., Howe, D. (1997). Acoustic noise radiated by nominally identical induction machines fed from sinusoidal and non-sinusoidal power supplies. *EPE'97. Proceedings of the Seventh European Conference on Power Electronics and Applications*, vol. 2, pp. 2489–2494, Trondheim, Norway.

Zhu, Z.Q., Xu, L., Howe, D. (1999). Influence of mounting and coupling on the natural frequencies and acoustic noise radiated by a PWM controlled induction machine. *EMD'99. Proceedings of the Ninth International Conference on Electrical Machines and Drives*, pp. 164–168, IEE, Canterbury, UK.

Appendix A

Free response analysis of a one-axis symmetric plate

The free response analysis of the plate shown in Figure A.1 was conducted both experimentally, using STAR version 5.23, and with finite elements, using ANSYS version 5.6, in order to explore the modes of vibration of the structure and obtain their modal parameters. The plate is symmetric only along one of its axes. In this way a higher number of modes of vibration are found within a certain frequency range. The plate had a thickness of 12 mm and it was made of aluminium, presenting a Young's modulus of 6.85 x 10^{10} N/m^2, a density of 2700 kg/m^3 and a Poisson ratio of 0.34. Both the experimental and FEM free response analyses of the plate will be presented in this appendix.

A.1 Apparatus & instrumentation

- B&K 4374 acceloremeter
- B&K 2635 charge amplifier
- B&K 8001 impedance head
- B&K 2706 power amplifier
- B&K 4810 mini-shaker
- B&K 2032 dual spectrum analyzer
- NEC versa 4000 laptop computer

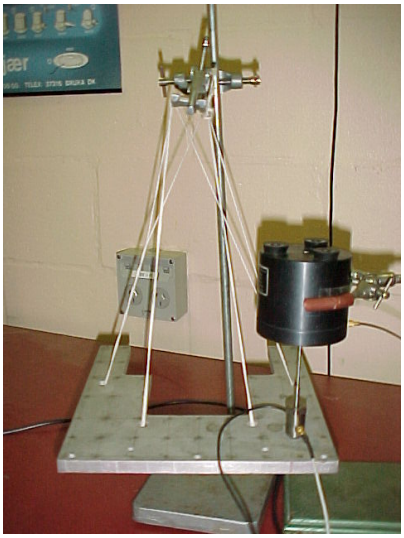

Figure A.1: Test plate.

A.2 Experimental free response synthesis

There are different steps that should be followed in order to set up the modal test. The number of degrees of freedom have to be selected first. It was considered that a number of 47 DOF would be enough to capture a reasonable number of modes and obtain a good representation of their shapes. Since the structure presents a two-dimensional behaviour, the SDOF points in the geometry are expected to move freely in the direction perpendicular to the plate. The different SDOF points are defined as a grid covering the whole structure and their coordinates were introduced into the STAR software, installed in the laptop computer, where the physical grid over the plate is reproduced, as shown in Figure A.2.

The suspension of the test object must be selected as well. In order to study the dynamics of the body the so called free-free condition should be established, and one method is to suspend the body by cords attached to a spring. The plate is excited with random waveform excitation taken from the signal generator incorporated into the analyzer, which in turn is connected to an elec-

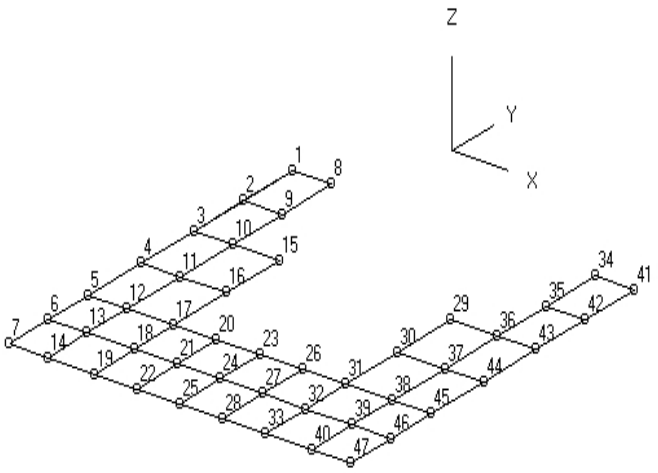

Figure A.2: Grid of SDOF nodes in STAR.

trodynamic vibration exciter. The exciter is attached through a force transducer to the structure at node 39, far from the symmetry axis of the plate so that both the symmetric and asymmetric modes will exhibit maximum motion. The force transducer is stud-mounted onto the body frame through a threaded hole and connected to the exciter at the other end. The plate remains in a horizontal position and the exciter is hold so that the group exciter-transducer remains perpendicular to the plate. The acceleration is measured at the 47 SDOF by means of an acceloremeter, which is easily attached at each point measurement through wax.

At node 39 the acceloremeter incorporated in the force transducer unit was used instead. The outputs from the two acceloremeters and the force transducer are connected to the spectrum analyzer through charge amplifiers, and it was ensured that the corresponding calibration values were set. Figure A.3 shows an schematic diagram of the setup with the details of the equipment used. Figure A.4 shows a picture of the actual set-up in the laboratory.

The spectrum analyzer calculates the frequency response function (FRF) for each SDOF measurement as the ratio between the spectrum of the acceleration at that point and the applied force at node 39. For each measurement, the input

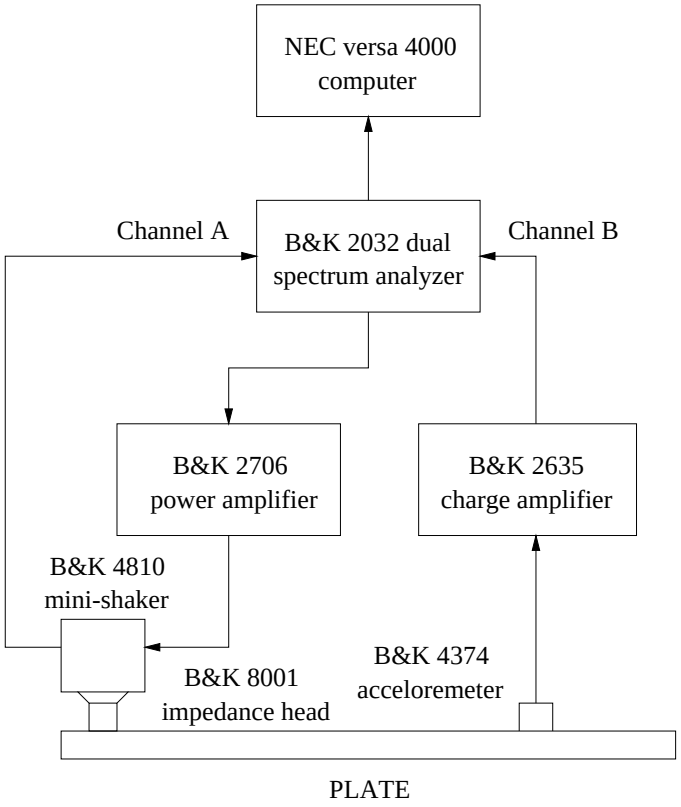

Figure A.3: Schematic of experimental set-up.

signals were averaged taking 50 samples with an overlapping factor of 50%. The frequency span was 3.2 kHz and a hanning window was used for the weighting of the results. The resolution in the analyzer was 4 Hz and the time for each sample was automatically adjusted by the analyzer depending on this resolution. After the averaging process, the FRF for each SDOF is stored for further post-processing in the laptop computer, which is connected to the analyzer through the serial port.

Since the plate was excited with random noise, the spectrum of the force is flat, and thus all the peaks which appear in the FRF will correspond to the natural frequencies of the plate. By visual inspection of the measured FRF

Figure A.4: Laboratory set-up for the free response analysis of the plate.

displayed in the laptop computer, it can be appreciated that a number of resonances are repeated from one SDOF to another at the same frequency, although their amplitudes vary, and that not all the resonances are present in all the measurements. Hence, some kind of weighted averaging should be done from all the measurements, in order to get a single representative FRF which will be used later for the 'curve fitting' process. This operation was automatically done in the software and the resulting FRF is shown in Figure A.5.

A SDOF curve fitter is used and each resonance peak is isolated in a band, i.e. between an upper and a lower user-defined frequency. These limits must be carefully selected in order to pick data only corresponding to that resonance, trying to avoid the influence of the adjacent modes. A number of 8 bands were defined in the 0 Hz - 3.2 kHz frequency range. With this information, the curve fitting process is automatically done by the software and the results are presented in Table A.1 in the next section, where the ANSYS predictions are also included for comparison. Figure A.6 shows the shape of the first eight modes of vibration.

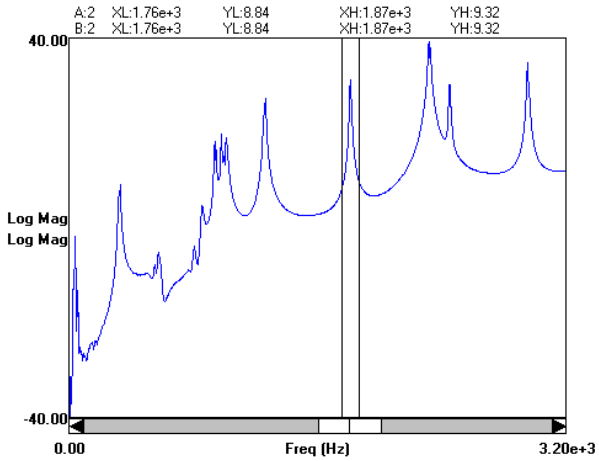

Figure A.5: Averaged frequency response function of the plate.

A.3 FEM free response synthesis

A model of the plate was reproduced in ANSYS, see Figure A.7. The material was set to be isotropic and Shell63 elements were used, with a default size of 0.03 mm. The number of elements and nodes was 2864 and 3049 respectively. The modal analysis was performed using the reduced analysis type, with a frequency span between 0 Hz and 4 kHz. The frequencies of the modes corresponding to the experimental ones are presented in Table A.1, where also the damping calculated by the STAR software is included. All the experimental modes were identified, although two extra modes appeared at the frequencies of 1172.6 Hz and 2268.6 Hz, which were not observed in the experiments.

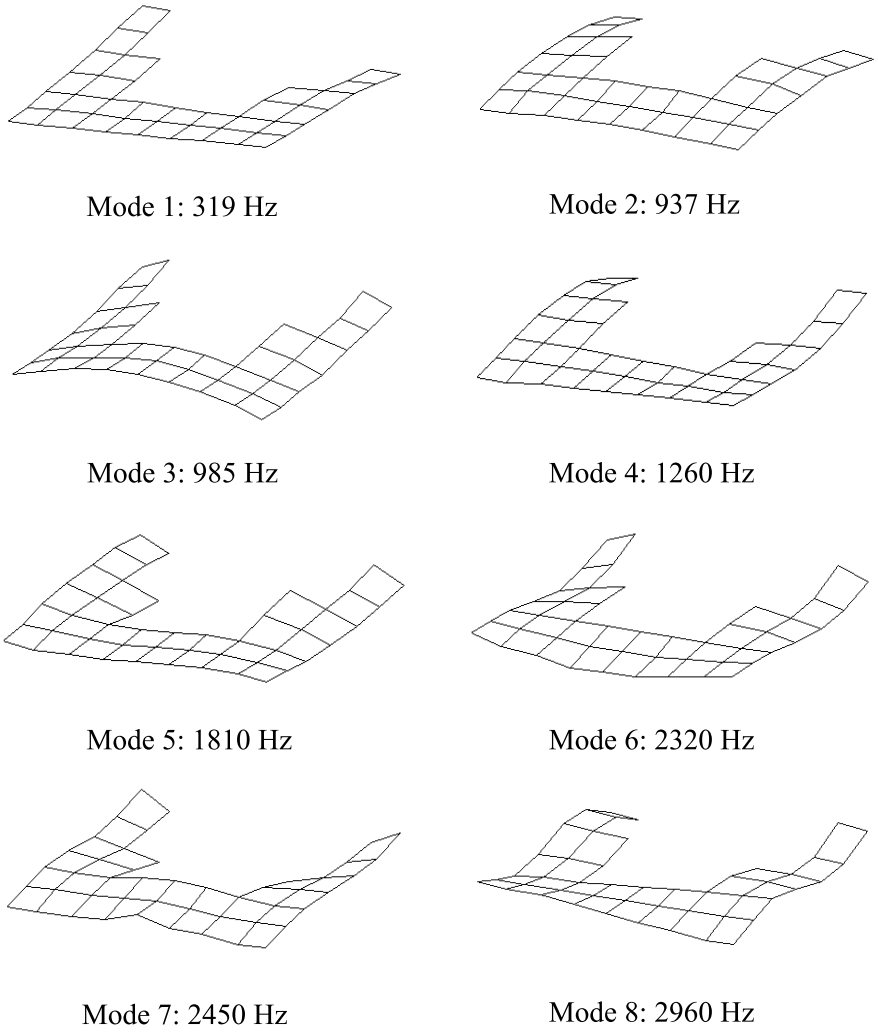

Figure A.6: Experimental modes of vibration of the plate structure.

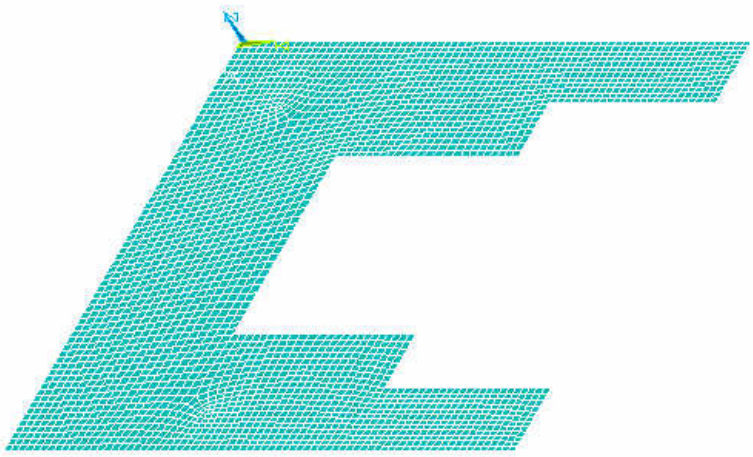

Figure A.7: Finite element model of the plate.

Mode	*STAR Fq.(Hz)*	*ANSYS Fq.(Hz)*	*Damp. (Hz)*	*Damp. (%)*
1	319.72	322.98	0.14	43.59e-3
2	937.63	912.40	0.16	16.93e-3
3	985.01	936.71	6.50	659.5e-3
4	1.26e+3	1272.1	0.63	50.25e-3
5	1.81e+3	1935.5	2.13	117.7e-3
6	2.32e+3	2345.9	3.34	143.9e-3
7	2.45e+3	2576.7	3.34	136.2e-3
8	2.96e+3	2950.0	3.51	118.7e-3

Table A.1: Modal parameters of the plate.

Appendix B

Forced response analysis of a one-axis symmetric plate

The purpose of the forced response analysis of the plate is to measure the noise radiated by the structure when a force of a certain frequency and amplitude is used for the excitation. The experimental results will be compared with the prediction done using finite and boundary element analyses.

B.1 Experimental forced response synthesis

The equipment used for the excitation of the plate is the same as the one used in the free response analysis presented in Appendix A. Since the results will be quantitatively compared with the computations, the force transducer has to be carefully calibrated. This was not the case in the free response, since a force of any magnitude and random frequency will excite the same modes in the structure, and this will vibrate following a pattern which is inherent for each mode. However, the level of vibration will depend on the amplitude of the excitation, and this will determine the amount of noise radiated by the structure. The force transducer can be easily calibrated with the help of a known mass, which is attached to one of the ends of the impedance head, and a known acceleration applied with a calibrator exciter at its other end. Since both the combined mass of the transducer plus the attached mass and the acceleration applied are known, the theoretical force inside the impedance head can be calculated using Newton's first law and the charge amplifier connected to the force transducer is adjusted.

A force of 0.28 Newton with a frequency of 320 Hz is perpendicularly applied to the plate at node 39. The frequency selected corresponds to the first experimental mode in order to increase the acoustical response. The acceleration is measured at 11 nodes and this will serve to compare the results obtained with the finite element calculations, presented in next section. Using this excitation, the overall sound power radiated has to be estimated. The sound power going through a certain area is calculated as the averaged normal acoustic intensity going through that area times the area of the surface. In order to calculate the overall sound power radiated, the plate was set inside a frame of dimensions 30x30x30 cm^3, see Figure B.1. The total sound power is calculated from the addition of the sound power from the individual sides of the frame, and it was assumed that the table where the frame was attached to reflected all the sound.

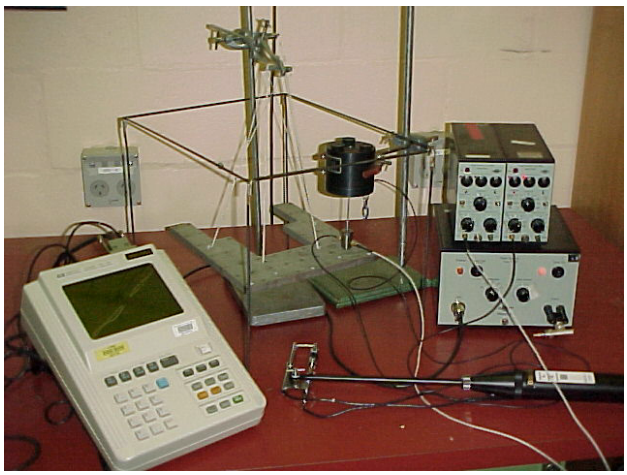

Figure B.1: Experimental set-up for the forced response analysis.

By sweeping the sound intensity probe all over one side of the frame, the instantaneous values of the sound intensity over the whole surface are processed in the HP analyzer connected to the probe, where the spectrum of the measurement is instantaneously averaged. The results are more accurate when a higher amount of points are stored, i.e. the longer time the probe is swept over the surface. Each one of the surfaces was continuously scanned six times, corre-

sponding to a time of around three minutes, until the spectrum in the analyzer was constant. The same procedure was repeated for the other sides of the frame and the results stored for each one of them in the HP analyzer in 1/3 octave bands. Multiplying this plot by the area of each surface and adding the results for all the surfaces, the overall sound power level (PWL) shown in Figure B.2 was obtained.

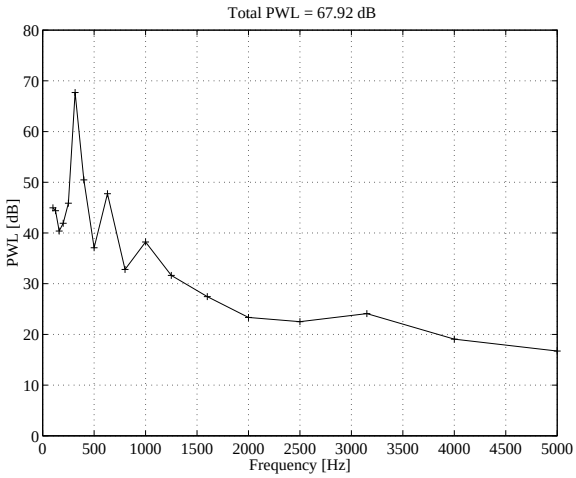

Figure B.2: Averaged Sound Power Level spectrum of the plate.

The total sound power obtained for the octave band with centre frequency at 315 Hz (thus between 280.63 Hz and 353.57 Hz) was 67.69 dB, and this corresponds to the highest peak in the plot. Since there is only one mode in this band, at 320 Hz, it was assumed that all this power corresponded to the excitation of that mode. The total sound power level resulting from adding the contributions of the whole spectrum was 67.92 dB so it can be concluded that the sound radiation of the plate is almost only induced by the first mode.

B.2 FEM forced response synthesis

The measured acceleration at the different SDOF in the plate can be compared with the ANSYS results using the same model as in the free response analysis. The model is now constrained with a force of 0.28 Newton applied at the node

in the finite element mesh situated the closest to the real coordinates of node 39. In the same way, the acceleration at the corresponding grid nodes is compared with the closest nodes in the finite element mesh, and the results are presented in Figure B.3.

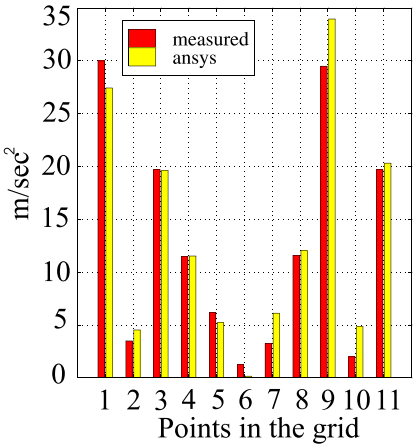

Figure B.3: Comparison of the acceleration results for different points on the plate.

In order to calculate the theoretical sound power radiated by the plate, SYSNOISE version 5.3 was used. The geometry and the mesh were imported from ANSYS and a grid was defined around the structure, see Figure B.4, where the sound pressure level will be plotted after the acoustic calculations. The modal frequencies also needed to be imported but this was not possible because of the incompatibility between the available versions of ANSYS and SYSNOISE. The modes were calculated directly in SYSNOISE instead, although the results were less accurate than the ones obtained from ANSYS. The new frequency for the first mode was 304.6 Hz, so this was the frequency of the force applied at the same node used for the excitation in ANSYS, maintaining the same amplitude of 0.28 Newton. The sound power calculated in SYSNOISE at this frequency was 66.21 dB, when a damping of $4.36\text{x}10^{-4}$ was used, which corresponds to the experimental damping obtained for the first mode in the free response analysis. The difference in PWL with the measured 67.69 dB is probably due

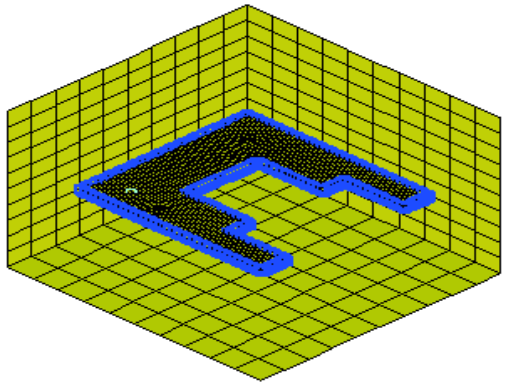

Figure B.4: Sysnoise preprocessor

to the damping factor. As explained in Appendix A, the modal parameters are obtained by curve fitting from the selected bands delimiting the modes in the averaged FRF plot. These bands are user-defined, so the user's skills play an important role in the estimation of the modal parameters.

The sound pressure level in the mesh surrounding the plate is shown in Figure B.5. It can be appreciated that although the force is applied far from the symmetry line of the structure, the sound pressure level (SPL) distribution is perfectly symmetrical all over the surrounding grid. This symmetry was still observed if the force was increased or the damping changed, but is no longer present if the frequency of the force is slightly changed a few Hertz from the calculated modal frequency, as shown Figure B.6. In fact, the excitation frequency in Figure B.5 matches perfectly the theoretical one calculated in SYSNOISE for the first mode. Since all the energy is used to excite this mode, the structure will vibrate only with the corresponding mode shape. This mode is anti-symmetrical but it should be noted that, since the sound pressure is a scalar quantity, the plot of the SPL in the figure looks symmetric. When the frequency of the exciting force is shifted a few Hertz, the input energy is not only exciting the first mode but also producing a translation of the plate upwards and downwards, which is more important in the side of the plate where the force is applied, and this is the reason for the higher SPL observed around this zone in Figure B.6.

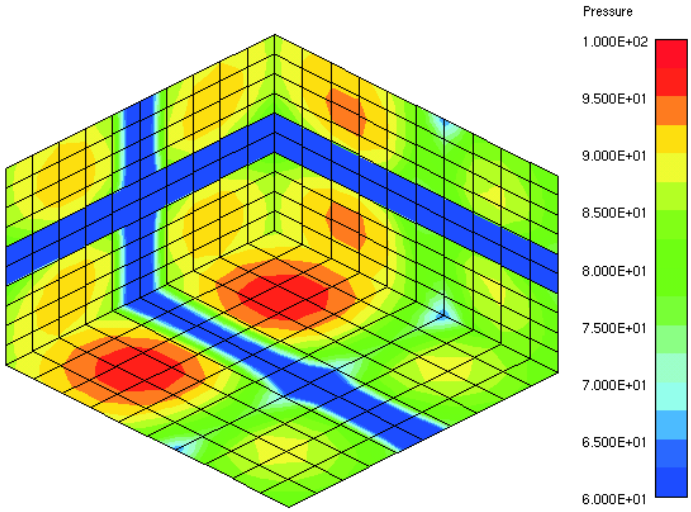

Figure B.5: SPL at 304.6 Hz

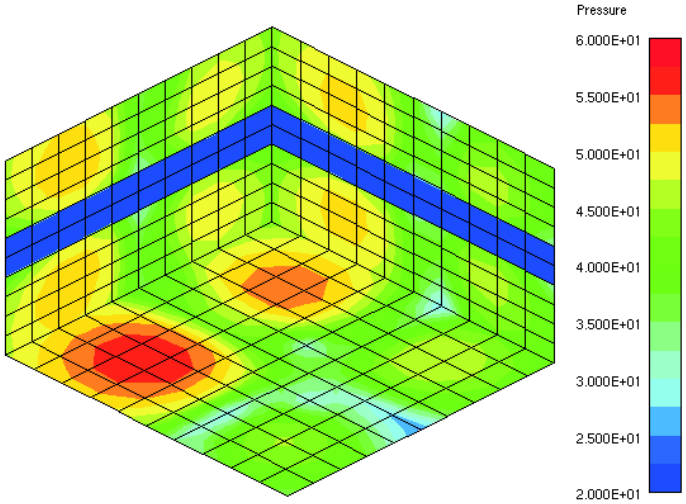

Figure B.6: SPL at 310 Hz

Appendix C

No load sound intensity measurements

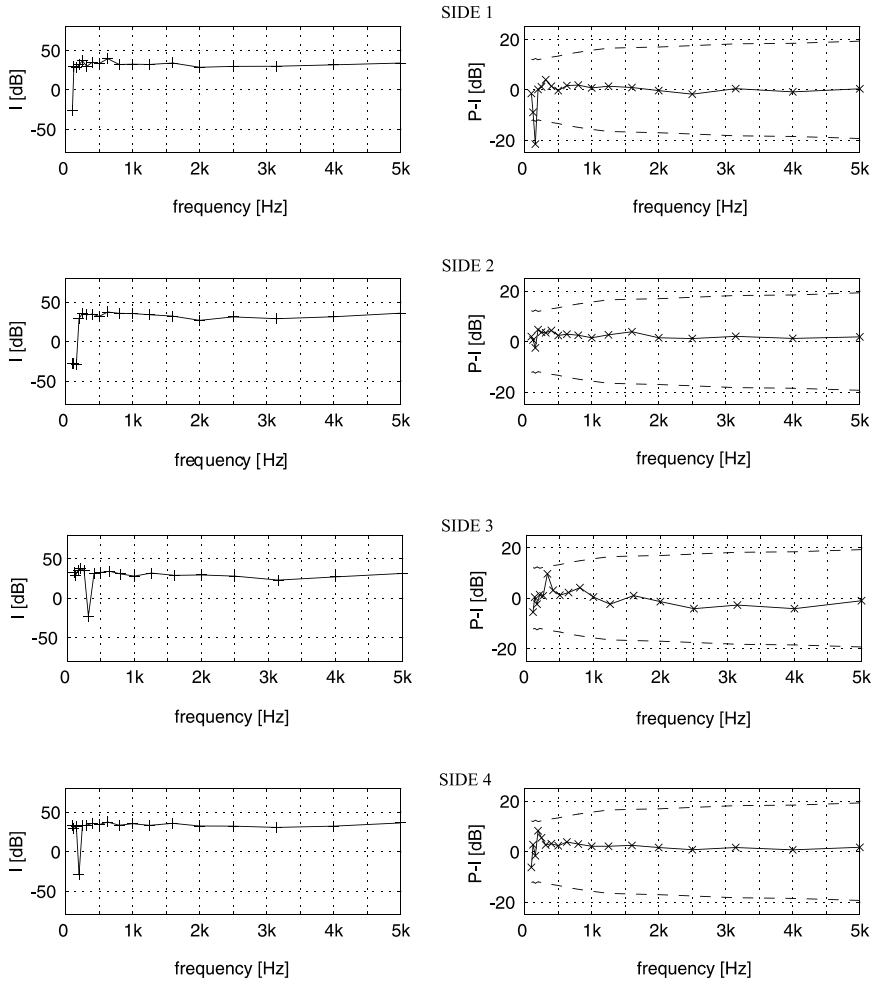

Figure C.1: Measured sound intensity and residual index over the four free sides of the frame when d=0, q=0.

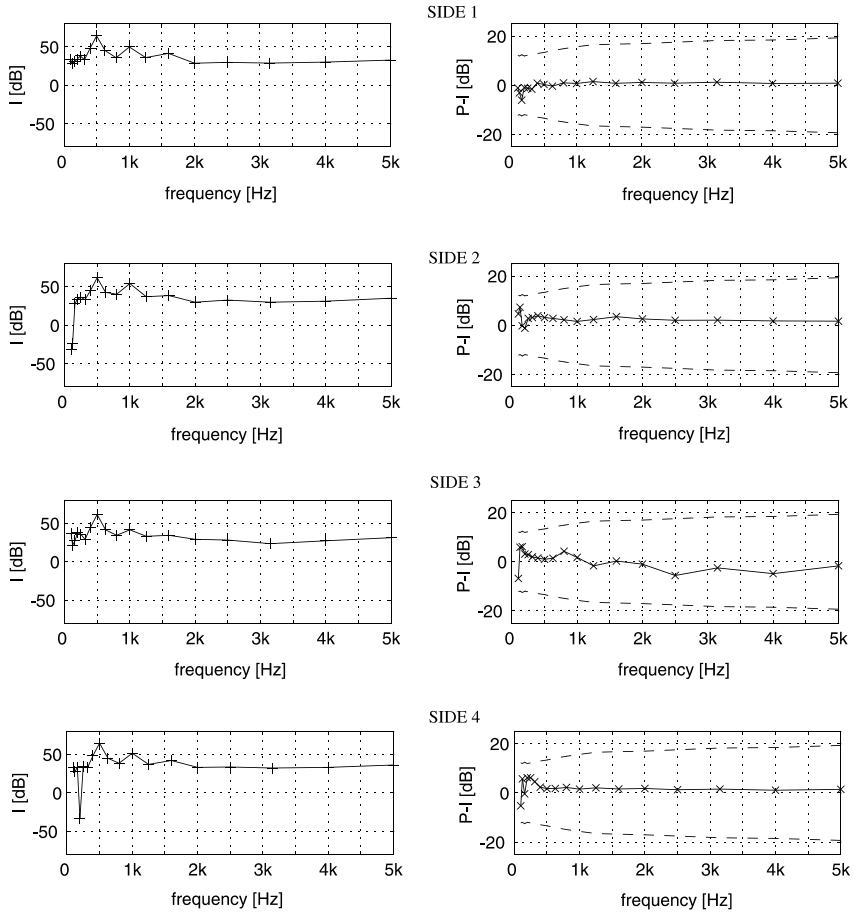

Figure C.2: Measured sound intensity and residual index over the four free sides of the frame when d=m, q=0, f=490 Hz.

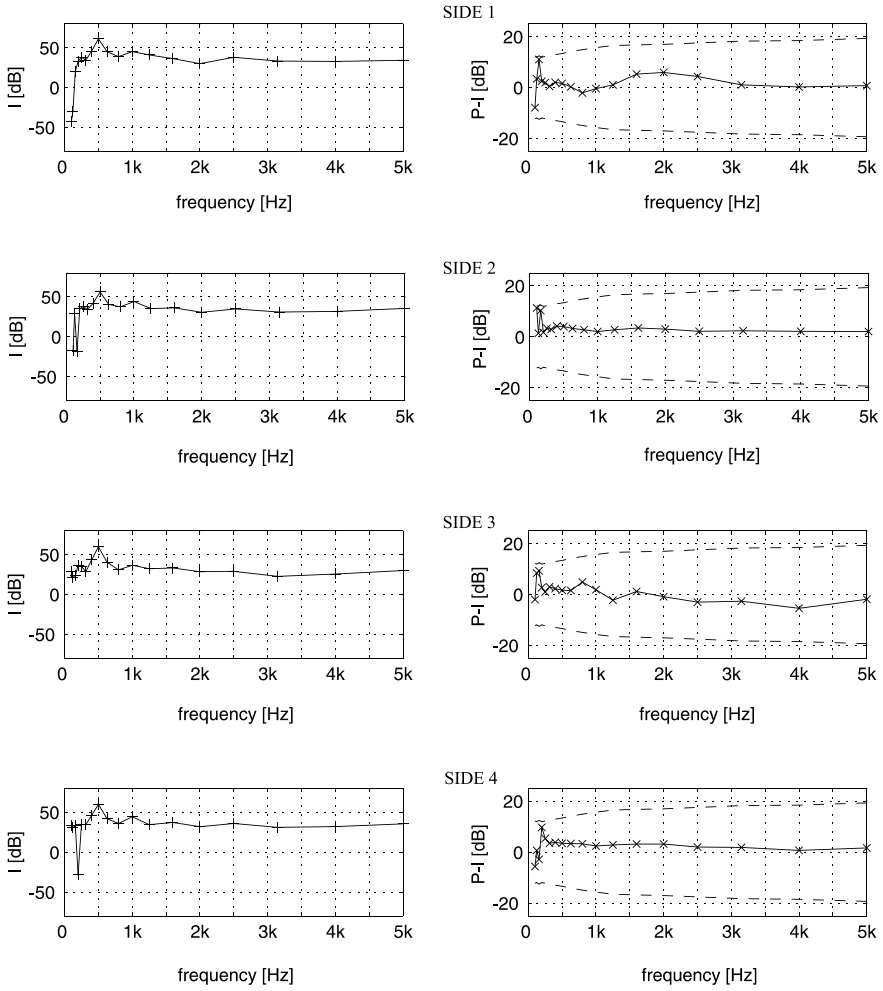

Figure C.3: Measured sound intensity and residual index over the four free sides of the frame when d=0, q=m, f=490 Hz.

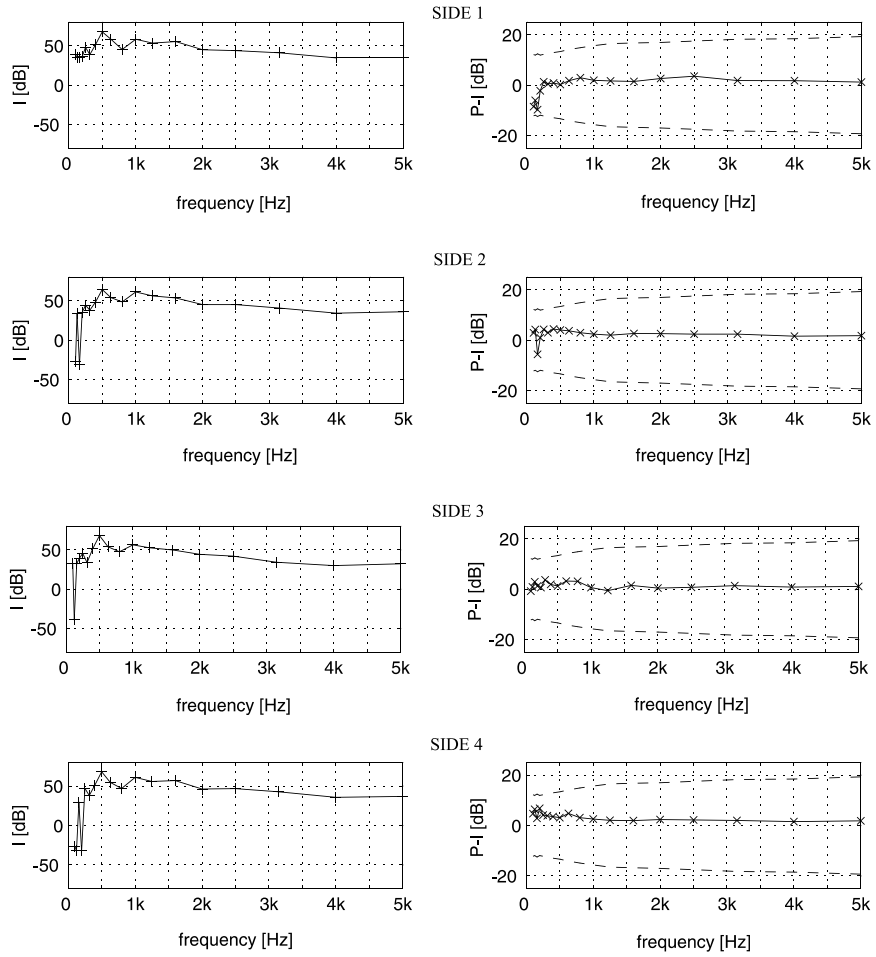

Figure C.4: Measured sound intensity and residual index over the four free sides of the frame when d=m, q=0, f=1105 Hz.

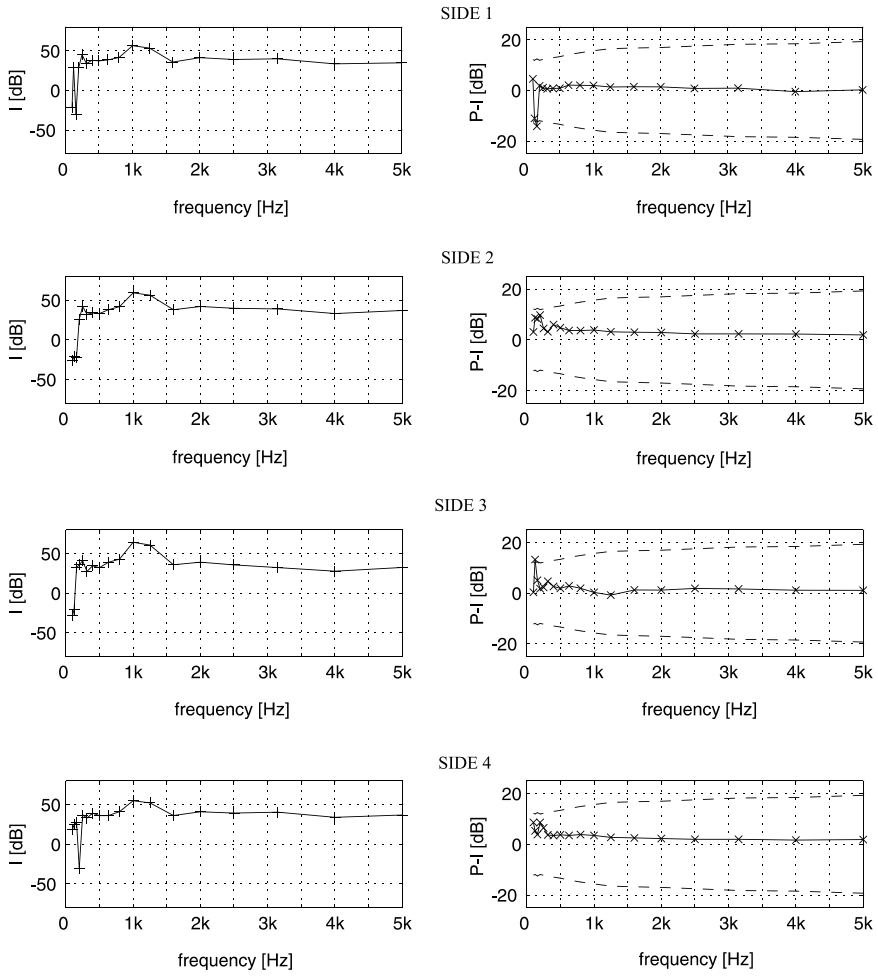

Figure C.5: Measured sound intensity and residual index over the four free sides of the frame when d=0, q=m, f=1105 Hz.

Appendix D

Load sound intensity measurements

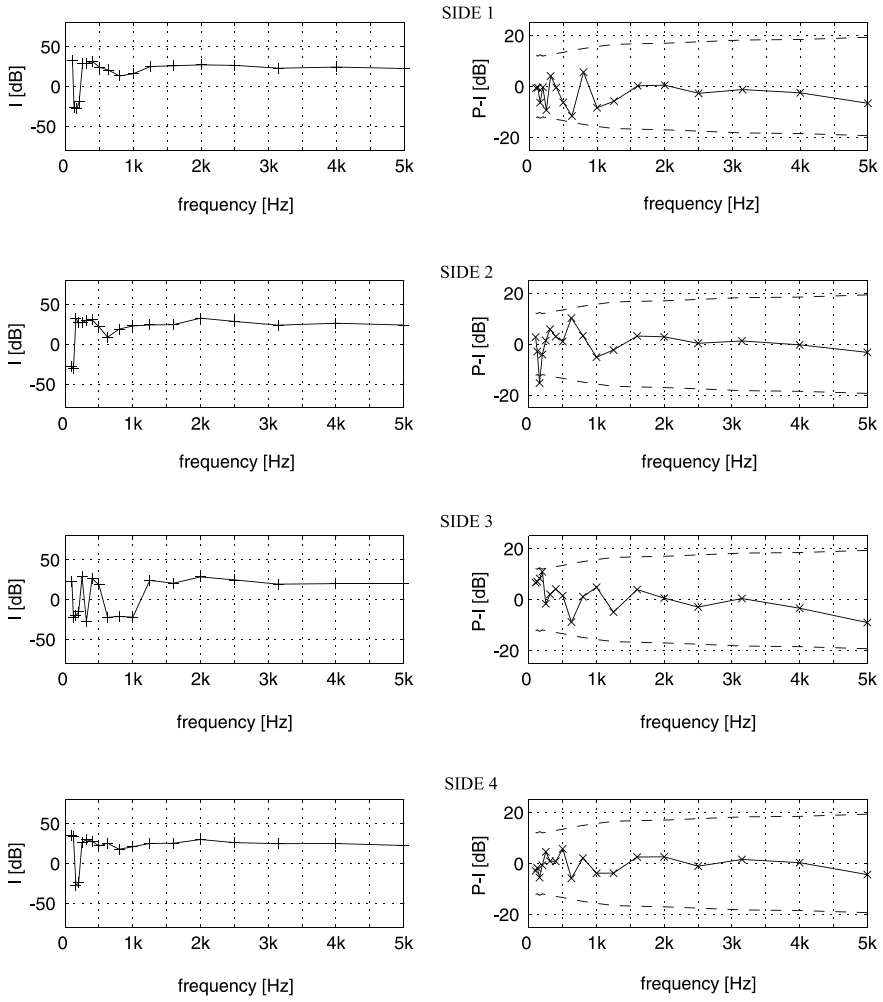

Figure D.1: Measured sound intensity and residual index over the four free sides of the frame when d=0, q=0.

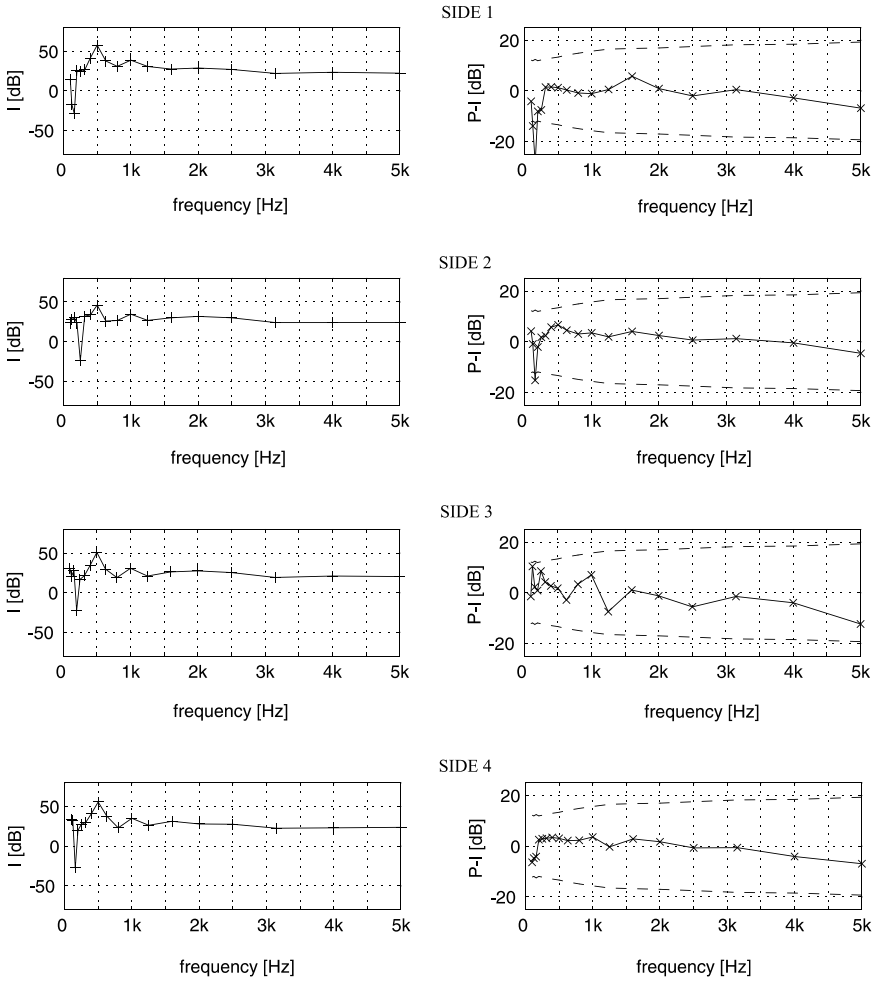

Figure D.2: Measured sound intensity and residual index over the four free sides of the frame when d=m, q=0, f=490 Hz.

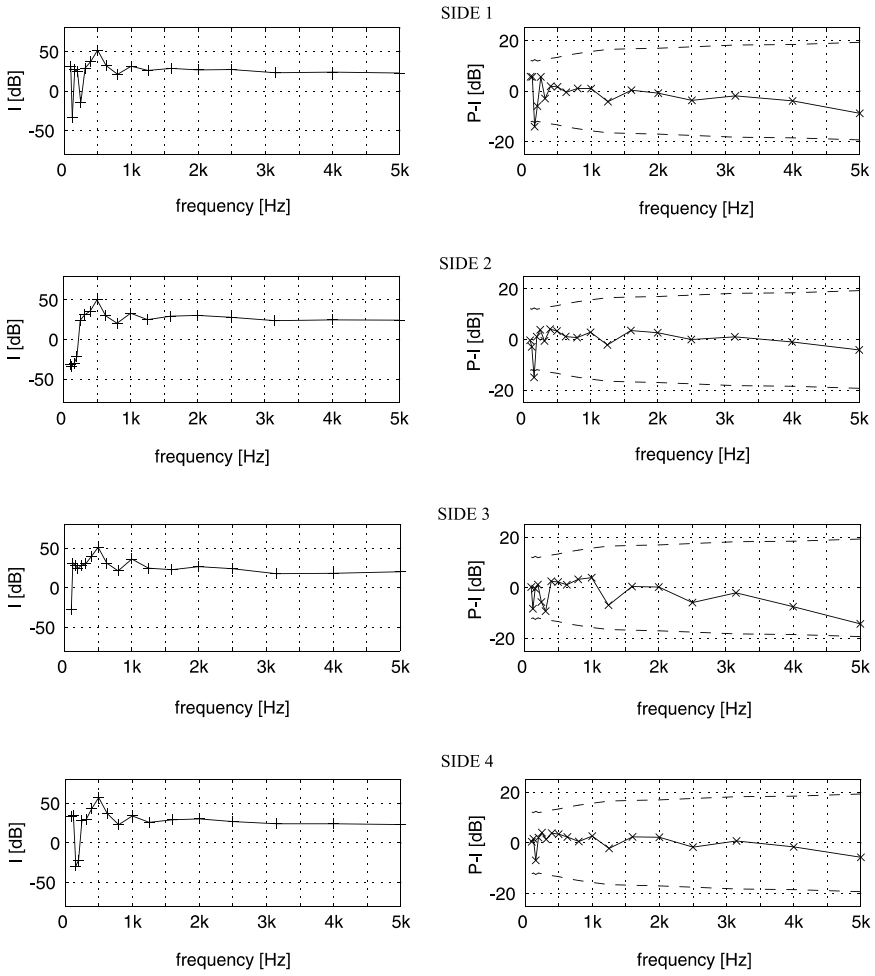

Figure D.3: Measured sound intensity and residual index over the four free sides of the frame when d=0, q=m, f=490 Hz.

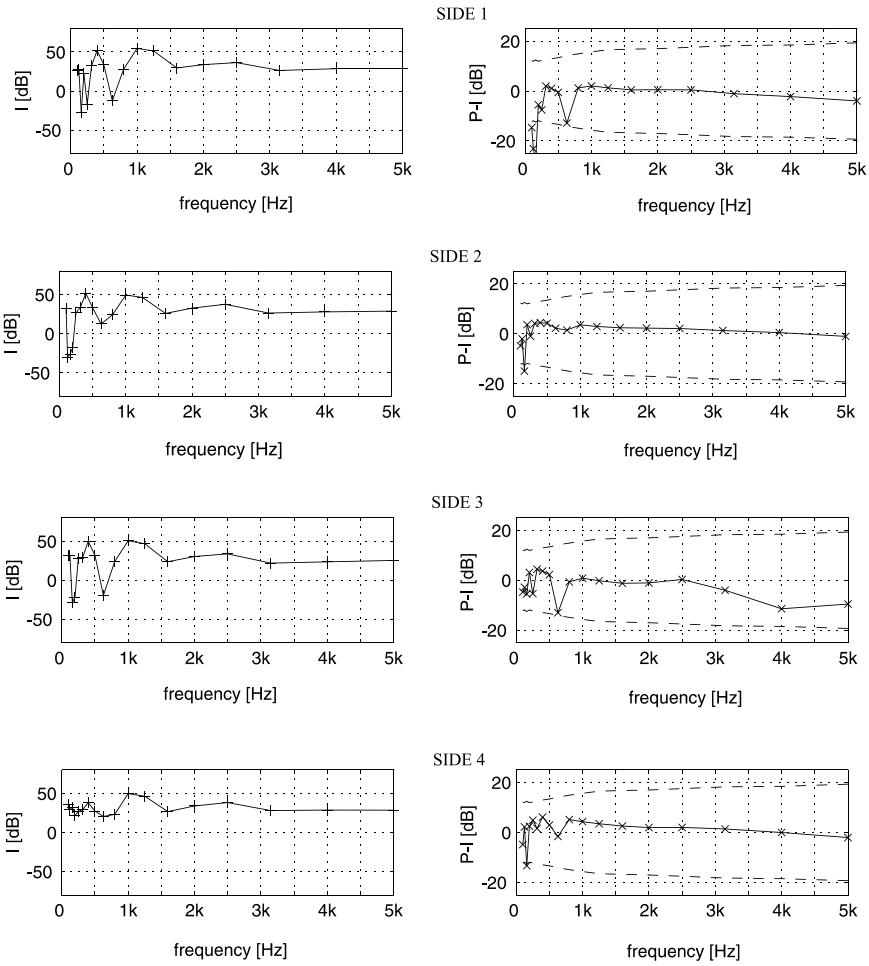

Figure D.4: Measured sound intensity and residual index over the four free sides of the frame when d=m, q=0, f=1105 Hz.

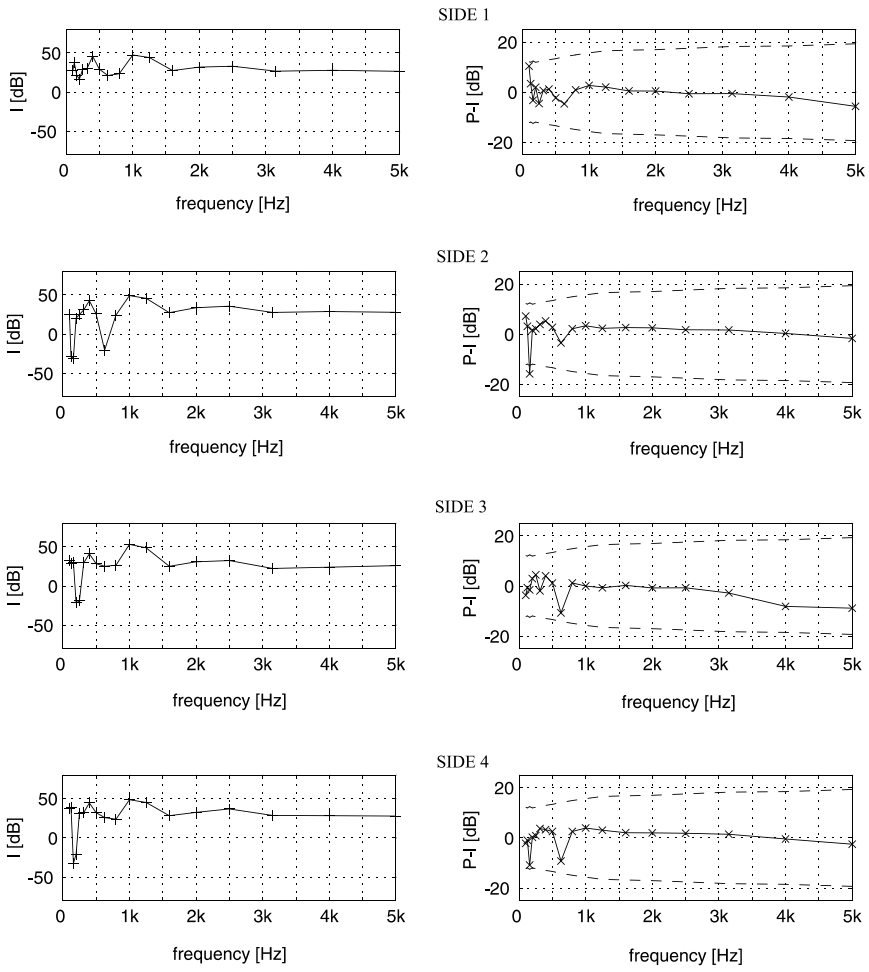

Figure D.5: Measured sound intensity and residual index over the four free sides of the frame when d=0, q=m, f=1105 Hz.